Azo Dyes Incorporating Cyclopentadienyliron Moieties: Synthesis, Polymerization, Decomplexation and Stability Studies

Masters Thesis

Submitted to the Faculty of Graduate Studies in partial Fulfillment of the Requirements for the Degree of Master of Science

University of Manitoba
Winnipeg, Manitoba
Canada

Wesley R. Budakowski

THE UNIVERSITY OF MANITOBA

FACULTY OF GRADUATE STUDIES

*****

COPYRIGHT PERMISSION PAGE

AZO DYES INCORPORATING CYCLOPENTADIENYLIRON MOIETIES: SYNTHESIS, POLYMERIZATION, DECOMPLEXATION AND STABILITY STUDIES

BY

WESLEY R. BUDAKOWSKI

A Thesis/Practicum submitted to the Faculty of Graduate Studies of The University of Manitoba in partial fulfillment of the requirements of the degree of

MASTER OF SCIENCE

Abstract

A series of cyclopentadienyliron azo dye complexes have been prepared via metal-mediated nucleophilic aromatic substitution reactions. The complexed dyes displayed shifts in their absorption bands in the ultraviolet-visible region that resulted from changes occurring to the conjugated system of the azo dyes. Dyes that contained a substituted aminoazobenzene pendant to an organometallic backbone displayed hypsochromic shifts, while those that contained a complexed arene within a dye backbone displayed bathochromic shifts. The versatility of the metal-mediated nucleophilic aromatic substitution reactions allowed dye monomers, which contained an azo chromophore as a pendant side chain to an organometallic backbone, to be polymerized yielding coloured polymers.

Photolytic decomplexation, a technique shown to allow for the successful demetallation of a number of complexes under varying conditions, was used to demetallate the complexed dyes. Absorption profiles of the decomplexed dyes resembled those of the starting uncomplexed dyes. Photolysis in the presence of hydrogen peroxide was shown to degrade the dyes rapidly, through cleavage of the azo bond. Increased rates of reaction were observed for the organometallic dyes compared to the organic dyes. Thermolytic techniques were shown to produce products that are indicative of cleavage of the azo bond.

Dedicated to Ben Borysowich

Faithless is he who says farewell when the road darkens
(J.R.R. Tolkien)

Acknowledgments

I would like to thank everyone who helped me, either with the actual research presented herein (Tarek Afifi, and the rest of the group) or by just lending support when needed (friends, family). In particular, I would like to thank my supervisors, Alaa Abd-El-Aziz, and Ken Friesen, my external examiner Annemeike Fahrenhorst, and the following people who kept me sane throughout the program: Basil Elmayergi, Jen McClelland, Leslie May, the UofW "gang" (Joe Dimartino, Jeff Hurd, John Strong, Mike Woo), and Daryl Budakowski.

Table of Contents

List of Figures:

List of Tables

Wavelength, IR, TGA, Yield, GPC, and m/z tables:

^{1}H and ^{13}C NMR data tables:

List of Equations

List of Schemes

List of Abbreviations

APT	Attached proton test
ArC	Quaternary aromatic carbon
ArCH	Aromatic carbon
ArH	Aromatic Hydrogen
BF_4^-	Tetrafluoroborate anion
Cp	Cyclopentadienyl ring
$CpFe^+$	Cyclopentadienyliron
$CpRu^+$	Cyclopentadienylruthenium
Comp.	Complexed
DCC	Dicyclohexylcarbodiimide
DMF	Dimethylformamide
DMAP	Dimethylaminopyridine
DMSO	Dimethyl sulphoxide
EDG	Electron-donating group
emr	Electromagnetic radiation
EtOH	Ethanol
EWG	Electron-withdrawing group
FT	Fourier Transform
GC/MS	Gas Chromatography-Mass Spectrometry
GPC	Gel Permeation Chromatography
IR	Infrared
J	Coupling Constant
Mn	Number-average molecular weight
Mw	Weight-average molecular weight
n	non-bonding electrons
NIST	National Institute of Standards and Technology
NMR	Nuclear Magnetic Resonance
Nuc^-	Nucleophile
PF_6^-	Hexafluorophosphate anion
PEL	Polyelectrolytes
ppm	parts per million
rf	Radio frequency
S	Singlet state
S_NAr	Nucleophilic aromatic substitution
TGA	Thermogravimetric analysis
T	Triplet state
UV	Ultraviolet
Vis	Visible
Φ	Quantum yield
λ	Wavelength
π	pi-electrons
π^*	anti-bonding orbital
X^-	Generic anion

1.0 Introduction

1.1 Cyclopentadienyliron Complexes

1.1.1 Synthesis of $CpFe^+$ complexes

With regards to conventional organic synthesis techniques involving aromatic units, electrophilic aromatic substitution is one of the most encountered. However, should one desire to substitute a nucleophile onto an aromatic system (S_NAr), the presence of strong electron-withdrawing groups are required. The synthetic methodology is typically time consuming and requires harsh reaction conditions. An alternative to the attachment of sigma bonded electron-withdrawing groups to the aromatic system is the use of organometallic reagents that are coordinated to the entire electronic system of the aromatic ring. These units are strong electron-withdrawing groups (the $CpFe^+$ moiety is comparable to the presence of a o- and p- nitro group combined), and are easily removed following S_NAr reactions[1].

There are a variety of metallic moieties employed to increase the reactivity of arenes toward nucleophilic aromatic substitution. The degree of ring activation varies from one moiety to another, with ring activation increasing in the following order: $Cr(CO)_3 << CpRu^+ \approx CpFe^+ < Mn^+(CO)_3$. While $Cr(CO)_3$ complexes have been one of the most studied, especially the [(η-arene)$(CO)_3Cr$] complexes, the starting material needed to produce this complex ($Cr(CO)_6$) is expensive and reaction times are typically long[2]. Cyclopentadienyliron complexes, however, do not suffer from these drawbacks, and can be readily made via a ligand exchange reaction involving low cost and low toxicity starting materials, thus producing highly soluble products with easily removable organoiron moieties[2-4].

Nesmeyanov was the first to use the ligand exchange reaction to produce a [(η^6-arene)(Cp)Fe^+]X^- complex[5]. The ligand exchange reaction (Scheme 1.1.1) has since been used extensively in the preparation of various organoiron arene complexes[6]. The reaction utilizes ferrocene, an arene, $AlCl_3$ and Al powder. The $AlCl_3$ coordinates to a Cp ring of ferrocene, which undergoes nucleophilic attack by the arene to form the ligand exchange product. The presence of the Al powder prevents the oxidation of the ferrocene to the ferricinium ion[5-6]. Typically, due to the Lewis acid nature of the $AlCl_3$, the presence of electron-withdrawing groups on the arene ring tend to lower the reaction rate by coordinating to the Lewis acid. Conversely, the presence of electron-donating groups increase the yields and allow the reaction to occur under milder conditions[7]. Following reaction, the cationic complexes are isolated as their salts.

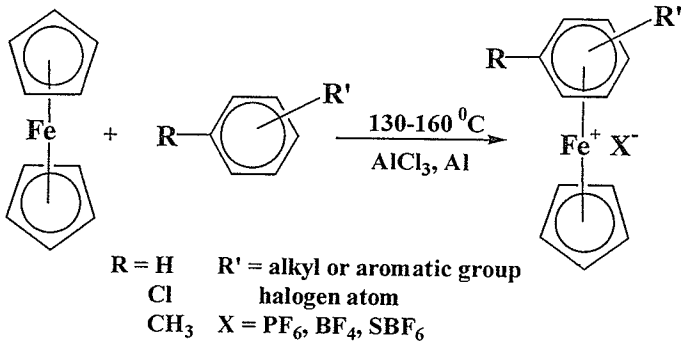

Scheme 1.1.1: A ligand exchange reaction yielding complexed arene-Fe^+Cp complexes

Once isolated, the arene unit of the arene-Fe^+Cp complex may undergo nucleophilic aromatic substitution with various nucleophiles, thus creating C-C, C-N, C-S, and C-O bonds. Once again, Nesmeyanov pioneered this reaction, and it has

subsequently proven quite useful in the synthesis of a variety of organoiron complexes that incorporate various nucleophiles[7-11]. Scheme 1.1.2 presents a generic example of some of the reactions common to this system[7].

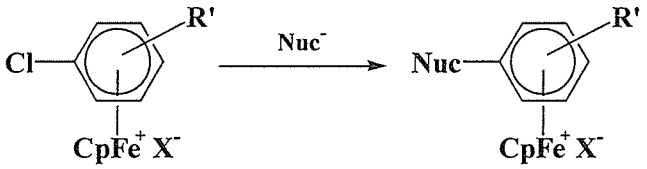

Nuc = PhOH, PhSH, CH(CN)COOEt
$CH(COMe)_2$, $CH(COPh)_2$

Scheme 1.1.2: S_NAr reactions involving a $[(\eta^6\text{-arene})(Cp)Fe^+]X^-$ complex

1.1.1 Polymerization of $CpFe^+$ complexes

One of the more interesting applications of organoiron complexes lies in their use in polymer synthesis. Methods for preparing polymers incorporating repeating aryl-ether or thioether units are typically hindered by harsh reaction conditions and low yields[12-13]. The Ullmann synthesis and non-metal mediated nucleophilic aromatic substitution reactions are two of the conventional polymerization techniques affected by these drawbacks. However, using organoiron chemistry allows for a rather facile synthesis to be conducted producing organometallic polymers. These metallated polymers may be interesting in themselves due to the electrical, mechanical and optical properties imparted by the metal, or may be decomplexed to yield the organic analogue which would have been difficult to synthesize otherwise[1,14]. Scheme 1.1.3 presents an example of the use of organoiron complexes in the synthesis of polyarylethers[15]. The complex and nucleophile are commonly reacted in high concentration to obtain the

polymeric material[1]. Additionally, the technique readily incorporates C-S and C-N bonds into the polymer by simply changing the choice of nucleophile. Thus a tailor-made polymer may be synthesized. This is especially important given that these types of aromatic polymers are typically used as thermoplastics, thus the thermal stability of the polymers can be tailored depending on the choice of nucleophile. Organoiron arene complexes have been used in the synthesis of a variety of polymers ranging from the above-mentioned polyarylethers to polynorbornenes and polymethacrylates[15-19].

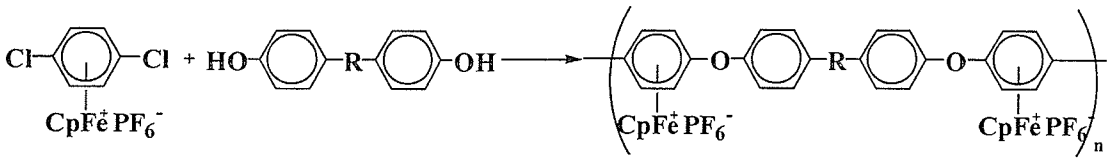

R = direct bond ; $C(CH_3)_2$; $C(CH_3)_2C_6H_4C(CH_3)_2$;
$C(CH_3)C_6H_4$; $C(CH_3)(CH_2CH_2COOH)$

Scheme 1.1.3: Polyarylethers synthesized via metal mediated S_NAr

1.1.3 Decomplexation techniques

As aforementioned, the organometallic moiety may be removed easily, thus allowing the organic analogue to be isolated. There exist three primary techniques available for the decomplexation of the arene, namely, pyrolytic sublimation, electrochemical liberation, and photolytic liberation[2].

Pyrolytic techniques have commonly been used, but typically require special equipment (pyrolytic sublimator) and are only applicable when the product is thermally stable. The process utilizes high temperatures (200-250 °C) to cleave the arene-iron

bond. The demetallated product then condenses on a 'cold-finger' in the sublimator apparatus[2,7,20,21]. With regards to thermally unstable compounds, electrochemical techniques have also been examined, as they require milder reaction conditions. However, they require specialized equipment and since the process requires lower concentrations of complex, there is a need to combine samples in order to isolate the desired product. This is a definite drawback given that each sample may take 2-3 hours for complete decomplexation[7,22,23]. Furthermore, the process is not applicable to compounds that are easily reduced.

Photolytic techniques were first investigated by Nesmeyanov, who reported the release of ferrocene and benzene upon irradiating THF solutions of $[(\eta^6\text{-}C_6H_6)(Cp)Fe^+]X^-$. Photolytic techniques have since become a very widely used method for liberation of arenes from organoiron complexes. The process is amenable to thermally unstable compounds, is applicable for functional groups susceptible to reduction, and allows facile product isolation[7,24,25]. The common products of photolytic demetallation are the free arene, ferrocene, and Fe(II) ions, although in certain cases oxidation of ferrocene itself was observed in hydrocarbon solvents[26-28].

Mann has performed extensive work on the photolysis of organoiron-arene complexes, and has reported that the photolysis process is governed by two factors: the solvent used, and the anion present (X^-). It was found that, in solution, the complex exists either as an ion pair or freely solvated ions. Polar solvents facilitate the freely solvated forms, while non-polar solvents favour the formation of ion pairs[29-31]. The solvent is ultimately responsible for liberating the arene, however, should the complex exist as an ion pair, then the anion will take part in the transition step. The degree of

association depends on the nucleophilicity of the anion, or solvent. The nucleophilicity of the anion increases in the order: $SbF_6^- < PF_6^- << ClO_4^- < BF_4^- < CF_3SO_3^-$, while solvent nucleophilicity increases in the order: $CH_2Cl_2 < CH_3CN < CH_3OH < H_2O$[30]. The mechanism of decomplexation is primarily either a solvent assisted reaction (for polar, nucleophilic solvents) or an anion assisted reaction (for non-polar, weakly nucleophilic solvents). It should be noted that while acetonitrile is lower on the list of solvents, it is an adequate choice for a solvent, and has been used extensively in liberation reactions[7,24-30].

A generic photolytic induced demetallation reaction is shown in Scheme 1.1.4[28]. This reaction proceeds though an intermediate that incorporates the solvent, commonly CH_3CN, as a temporary ligand. The intermediate has been identified by Mann as $[(\eta\text{-}C_5H_5)Fe(CH_3CN)_3]^+$ (where C_5H_5 = Cp) by low temperature NMR and UV studies[28]. This intermediate then undergoes reaction with free cyclopentadienyl anion to yield ferrocene, as shown in Scheme 1.1.5[28].

$$2[(\eta\text{-}C_5H_5)Fe(arene)]^+ \xrightarrow[CH_3CN]{h\nu} (\eta\text{-}C_5H_5)_2Fe + Fe(II) + 2(arene)$$

Scheme 1.1.4: Net reaction for photolytic decomplexation in acetonitrile

$$[(\eta\text{-}C_5H_5)Fe(arene)]^+ \xrightarrow[CH_3CN]{h\nu} [(\eta\text{-}C_5H_5)Fe(CH_3CN)_3]^+ + (arene) \quad (1)$$

$$[(\eta\text{-}C_5H_5)Fe(CH_3CN)_3]^+ \xleftrightarrow{CH_3CN} Fe(CH_3CN)_6^{+2} + C_5H_5^- \quad (2)$$

$$[(\eta\text{-}C_5H_5)Fe(CH_3CN)_3]^+ + C_5H_5^- \longrightarrow (\eta\text{-}C_5H_5)_2Fe + 3CH_3CN \quad (3)$$

Scheme 1.1.5: Intermediate steps in a decomplexation reaction in acetonitrile

There have been questions raised regarding whether step 2 in Scheme 1.1.5 actually occurs. However studies examining irradiated solutions of (η-C_5H_5)$Fe(CD_3CN)_3^+$ with HBF_4 were observed to yield Fe(II) and free cyclopentadiene (C_5H_5). Additionally, photolysis of [(η-C_5H_5)Fe(η-C_6H_6)]BF_4^- in protic solvents (methanol, ethanol and water) showed the only products as Fe(II) and the free arene . This indirectly substantiates the existence of free $C_5H_5^-$, as this ion would rapidly protonate in such solvents thereby removing it from the reaction sequence before reaction 3 could occur[28].

The mechanism for the photolytic demetallation of an organoiron arene is illustrated in Scheme 1.1.6[4,24]. The two processes differ in that there exist either the ion pair, or the freely solvated ions. Regardless, upon irradiation, the complex is excited into a singlet state, and undergoes intersystem crossing to the lower energy triplet state (See section 1.2.1 for a explanation of these states). The triplet state is regarded as the reacting species since the process occurs even in the presence of singlet quenchers[24]. Once excited, the organoiron complex alters its structure from a η^6 complex to a η^4 complex through 'ring-slippage'[7,24,27,29,32]. This opens coordination sites on the iron atom allowing either solvent or the anion to temporarily coordinate to the iron. Further reaction with the solvent rapidly forms the products shown in Scheme 1.1.6[24].

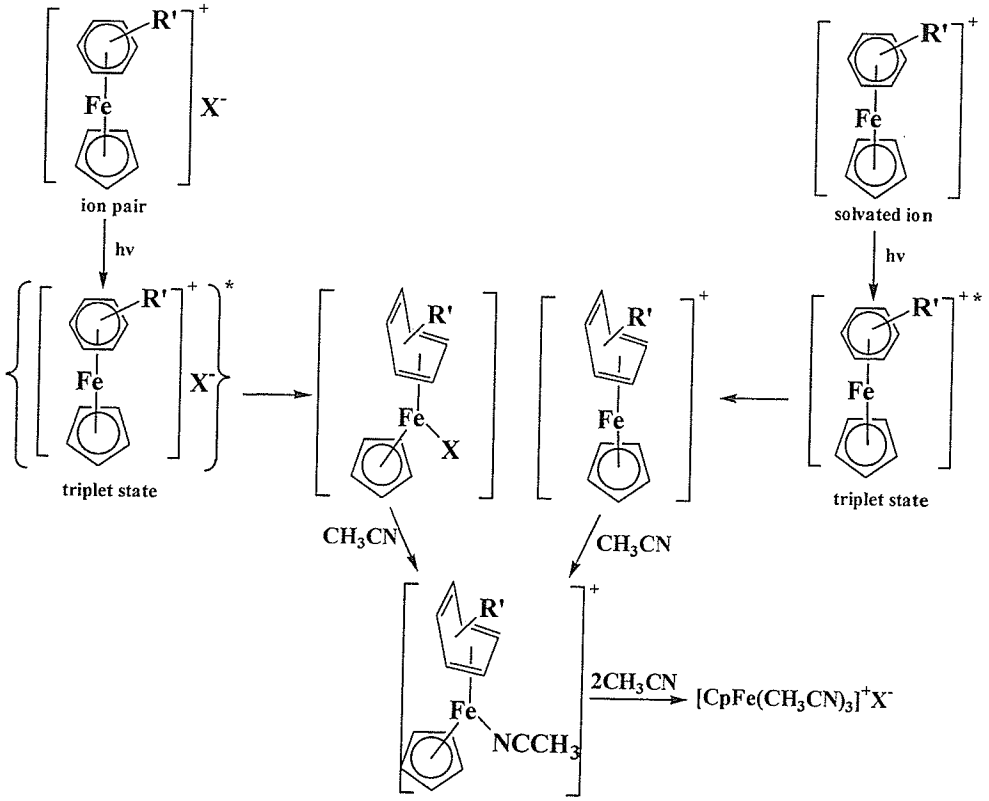

Scheme 1.1.6: Mechanism for photolytic demetallation

1.2 The Chemistry of Azo Dyes

Much attention has been given to the physical basis of colour. A dye is a coloured substance, usually organic in nature, which can be applied to a substrate in order to impart colour[33]. Usually the substrate is a textile fiber, but other applications such as paper, leather, hair, plastics, or foodstuffs are common. The production of commercial dye compounds is one of the largest industrially driven organic synthesis trades, and as a result there is little information preceding 1980 in the literature due to the flurry of patent activity that dominated this field[34]. The commercial dye trade is dominated by azo type dyes, first discovered by Peter Griess in 1858, which incorporate the N=N group as a chromophore, which commonly bridge two or more aromatic units[35]. Although most of the original data are subject to patent protection, there has been substantial subsequent (post 1975) research investigating various types of azo dyes, all exhibiting their own colour and characteristics[34,36-41]. The coloured dyes can be classified as $n \rightarrow \pi^*$ chromogens or donor-acceptor chromogens. Azo dyes fall into the latter category, that are characterized by possessing one or more substituents with lone pair electrons (donor groups) and one or more electron-withdrawing substituents (acceptor groups) attached to the same conjugated π-electron system. Figure 1.2.1 provides the generic representations of two of the more common forms; an aminoazobenzene (1) and a thiophene/thiazole derived azo dye (2)[34,36-41]. Recently these dyes have attracted considerable attention in polymer systems due to their potential uses in optical applications (Section 1.2.3)[42].

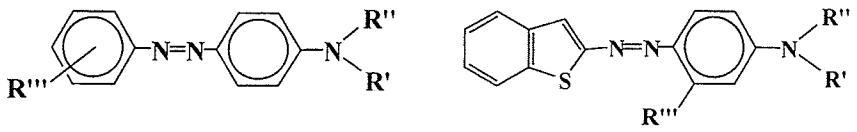

(A) (B)

Figure 1.2.1: Generic representations of an aminoazobenzene (A) and a thiophene based dye (B)

1.2.1 Synthesis and characterization of azobenzene dyes

The manufacture of azo dyes is always based on reaction of diazonium compounds of benzene (or heterocyclic moieties), with phenols, napthols, arylamines, pyrazolones, or other suitable components, to yield hydroxy-azo or amino-azo compounds[36-42]. The resulting dyes contain a chromophore (the azo group) and an auxochrome (the hydroxyl or amino group)[36-41].

Azo dyes are commonly synthesized via a coupling reaction of a diazo, or azo component (the terms are interchangeable), and a coupling component. For azobenzenes, the diazo component is quite often a functionalized aniline, while the coupling component may be an aniline or phenol[36-37,42]. In particular, N-β-hydroxyalkylanilines are commonly employed as coupling components, due to the electron donating ability of the aniline functional group[43]. Scheme 1.2.1 illustrates the formation of an azobenzene[35,44]. The reaction is termed a diazotization reaction, which can be categorized into two steps, namely a diazotization step and a coupling step. In the first, the diazo component undergoes diazotization as a result of reaction with nitrosylsulphuric acid (HSO_4NO, arising from the reaction of sodium nitrite with sulphuric acid). Other nitrosating agents may be used, such as nitrosyl bromide or chloride (NOBr/Cl), dinitrogen trioxide (nitrous anhydride, $NONO_2$), or the nitrous acidium ion ($NOOH_2$), however, nitrosylsulphuric acid is by far the most common[35,45].

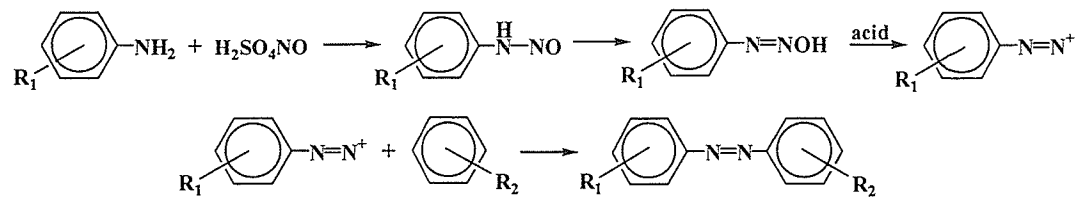

Scheme 1.2.1: Synthesis of an azobenzene dye

The formation of the azo functional group requires low pH and low temperature to allow for the formation of the acid, and to ensure that the stability of the intermediate is not compromised[35]. Diazotization proceeds upon stirring for a couple of hours, at which time the solution is combined slowly with a solution of coupling component (by either adding the azo solution dropwise to coupler or vice versa). The azo component, being strongly electrophilic, reacts with the coupling component, which typically has a carbon with higher electron density (such as the carbon occupying the para position in an aniline). The overall reaction is one in which a diazonium ion reacts with a free amine via electrophilic aromatic substitution[35,44].

The thiophene analogues are typically synthesized with the same overall method, but via a Gewald-type reaction which yields the 2-aminothiophene derivatives[38-39,46-48]. Regardless of the specific dye, the final step in the reaction process is neutralization of the medium. The actual method by which this occurs depends strongly on the nature of the reactants. Amines typically require acidic solvents, therefore must be neutralized by alkaline solutions, whereas phenols are typically coupled in slightly alkaline conditions, thereby necessitating the addition of an acid for neutralization. As would be expected, exact reaction conditions depend on the reagents chosen[37-38,49-50].

Structural confirmation of azo dyes can quickly be performed through nuclear magnetic resonance (NMR) spectroscopy[34,40,51], which is of definite advantage given the difficulty associated with locating and differentiating the azo and hydrazo bands in the infrared spectra of azo compounds[44]. The IR spectra of azo dyes are typified by numerous bands in the 1615-1000 cm^{-1} region, making structure elucidation troublesome at best. Due to the myriad variety of substituted azo dyes synthesized, no comprehensive NMR study has been performed, however there do exist a few comparisons within subclasses of azo dye structures themselves[34,51-53]. One of the more important factors to note is that although the azo linkage is not linear (predominately trans, see Section 1.2.2), the rapid rotation around the C-N bond causes the aromatic rings to become equivalent, as shown in Figure 1.2.2[51].

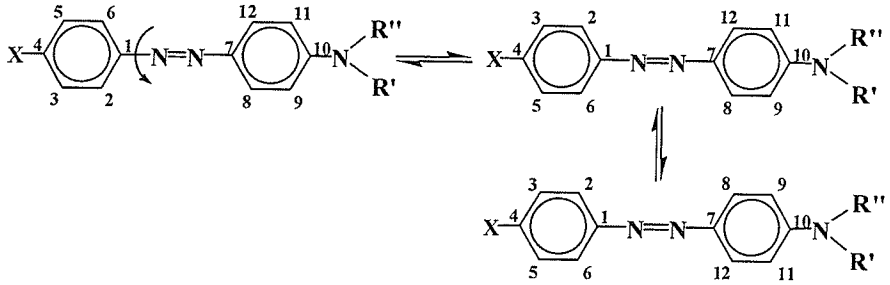

Figure 1.2.2: Nuclei equivalency caused by rotation around C-N bond.

1.2.2 Characteristics and Visual Properties of Azobenzene derived dyes

i) Excitation resulting from absorption of visible light irradiation

Prior to any in depth discussion regarding the nature of the azo dyes themselves, it is beneficial to overview the reasons compounds may be coloured. Colour arises from electronic transitions resulting from the absorption of electromagnetic radiation in the visible region of the spectrum, typically between 400-800 nm[35,53]. The actual colour observed for a substance arises from the conjugate colour of the absorption. Thus, for example, a red coloration results from the absorption of blue-green light at approximately 500 nm[54].

Upon absorption of light an electron will be promoted into an excited state. In the case of absorption of visible light the promotion occurs between the highest occupied molecular orbital (HOMO, typically nonbonding, n or pi-bonded, π) to the lowest unoccupied (LUMO) or anti-bonding orbital (π^*). Figure 1.2.3 compares the electron configuration of the ground (a) and excited (b) states of a molecule[55].

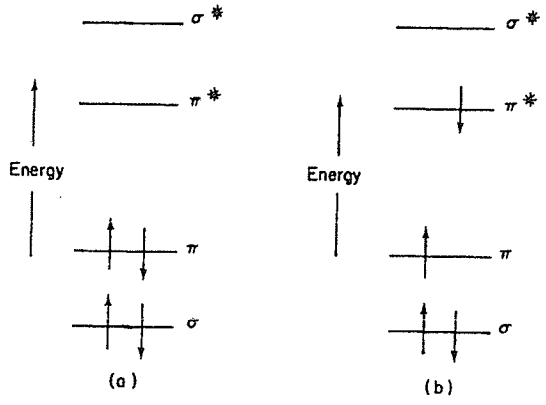

Figure 1.2.3: Ground (a) and Excited (b) levels of a molecule

The energy of the absorbed radiation must obey the Einstein-Bohr law [Equation 1.2.1], in order for any transition to occur.

Equation 1.2.1: $\Delta E = h\nu = hc/\lambda$

ΔE represents the difference in energy between the two levels, while h is Planck's constant (J·s), ν is the frequency of the radiation (s^{-1}), c is the speed of light ($m \cdot s^{-1}$), and λ is the wavelength of light (m)[35,55-56]. On excitation, the electron is promoted into an excited singlet state (in which the electron spin, or multiplicity, remains unchanged relative to its original value). Thereafter, the electron will not remain in the excited state, as the excited state is deactivated by collisions, emission of radiation, or photochemical reactions. Transitions that involve emission of radiation may result in a reversal of electron spin (change in multiplicity) which results in the formation of a triplet state (in which the two lone electrons have the same spin). Thereafter the excited triplet state may undergo photochemical reaction or radiative or non-radiative relaxation to the ground state. Figure 1.2.4 illustrates a Jablonski diagram, which demonstrates the various pathways available[55]. In Figure 1.2.4, abs represents absorption of a photon; S1, S2 and T1, T2 are excited singlet and triplet states, respectively; ν_r is vibrational relaxation; ic denotes internal conversion, while isc is intersystem crossing; fluorescence and phosphorescence are abbreviated fl and phos, respectively[55].

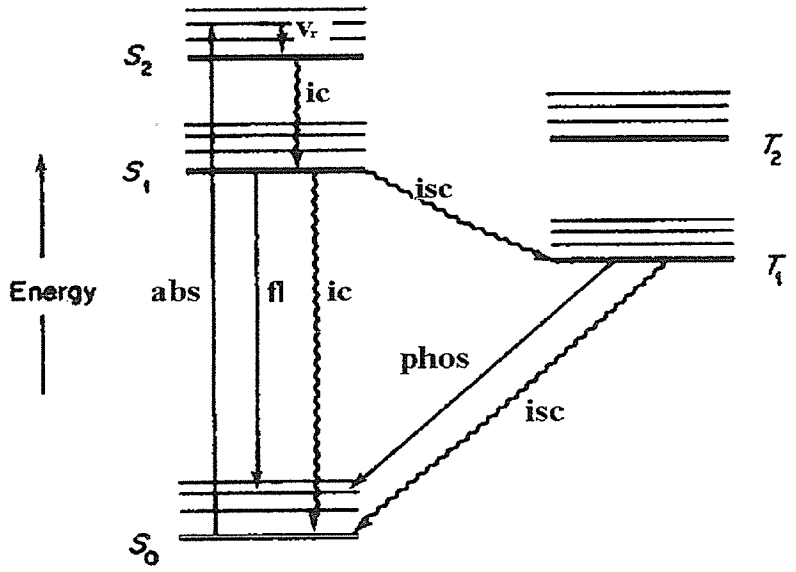

Figure 1.2.4: Jablonski Diagram

Absorption of light that promotes electrons into two closely spaced vibrational bands (within a given energy state) usually creates one broad band rather than two individually resolved bands. The broad bands result from the loss, or collapse, of the fine structure. These losses are due to the large number of different vibrational and rotational transitions available for a molecule, in addition to intermolecular effects arising from solvation[35,55]. Hence a wide single band, and not a number of individual bands are observed. The position, or wavelength, of this band is dependant on the energy of the light, as shown in Equation 1.2.1. The intensity of the band, however, is a measure of the probability of the particular excitation occurring. The higher the probability, the greater the intensity, and thus the larger will be the molar absorptivity (or extinction coefficient)[35]. Furthermore, the narrower the band, the brighter the colour, thus a narrow band will result in a more vibrant colour, while broad bands produce dull colours[57].

With regards to azo compounds, the transitions of importance are the π-π^* transition, in which a π electron is excited into an antibonding π^* orbital, and/or n-π^* transitions, where a non-bonding electron is excited[45]. π-π^* bands are typically more intense than the n-π^* transitions. The low intensity of the n-π^* transition, coupled with the often close proximity to the π-π^* transition renders the former rather insignificant in regards to the observed colour of a compound[55,57]. Given that overlap of the two bands is often common in azo dyes, the majority of attention has focused on the π-π^* transition[35,55-57].

The position of an absorption band can be largely affected by the structure of the compound. For example, if one examines an aromatic system versus a non-aromatic system, the aromatic system would, as a rule, absorb at higher wavelengths (lower energy). This occurs due to the degree of conjugation. As the conjugated system increases, the energy difference between the highest occupied and lowest unoccupied molecular orbitals decrease. Thus, the excited state will be stabilized to a greater extent, relative to the ground state, than in a non-conjugated system. This in turn means that less energy is needed to excite the molecule and the absorption band will be shifted to higher wavelength (red shifted)[35]. It is for these reasons that highly delocalised π electron systems typically exhibit vibrant colours[34].

ii) Azo dyes

Given the wide commercial application of azo-compounds as dyes and pigments, the most important property is that the compounds absorb in the visible region of the electromagnetic spectrum. Furthermore, a wide range of absorption characteristics,

providing an equally wide range of colour choices, would be preferred. Due to the high degree of conjugation associated with these types of molecules, absorption throughout the visible region is common. There have been many studies examining the wavelength maxima of azo dyes and the factors that may influence or change these values[36-37,58-62].

Azo dyes of the type shown in Figure 1.2.5 are termed donor-acceptor chromogens, due to the migration of electron density through the molecule[53,63]. In Figure 1.2.5, the diazo component, substituted with X, Y, and Z substituents (usually electron-withdrawing) is the acceptor (or azo) chromogen, while the coupling component, substituted with A and B (usually electron-donating) is classified as the donor chromogen[63]. The absorption band in the visible region is related to the migration of electron density over the molecule, from the terminal amino group to the azo bridge[53,63]. The largest band is characterized as the π-π^* band, usually occurring around 380-475nm (depending on the actual structure of the azo dye, see below) which may overlap with the weaker n-π^* band, typically occurring around 440 nm[36,45,64]. In addition, there are low wavelength absorptions present in the UV region, which are a result of electronic transitions involving the aromatic rings[45]. The n-π^* band is relatively unchanged as the substitution pattern of the benzene rings is altered, owing to the fact that the n-π^* band is localized on the azo group, and thus is relatively free from changes to the aromatic system. However, the highest occupied π orbital arises from the aromatic rings, thus any change in the electron distribution of the benzene system will result in a change of position of the π-π^* band[56].

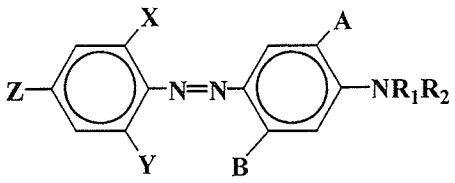

Figure 1.2.5: Substituted azobenzene

iii) Canonical representations and isomerization of the azo group

Owing to the high degree of delocalization in azo molecules, the dye can be thought to exist in two canonical forms. Figure 1.2.6 illustrates these two forms[63]. It has been found that in the ground state resonance structures do not exhibit a large influence, and that form (I) can approximately represent the ground state. However, due to the imparted energy associated with the excited state, the resonance forms do become significant, and thus may influence the visible absorption band. It is for this reason that the dipolar form (II) is typically used to represent the excited state[63,65]. Which one dominates, and to what degree, is dependant on the nature of any substituents present, and the steric factors that may arise from them[36-37].

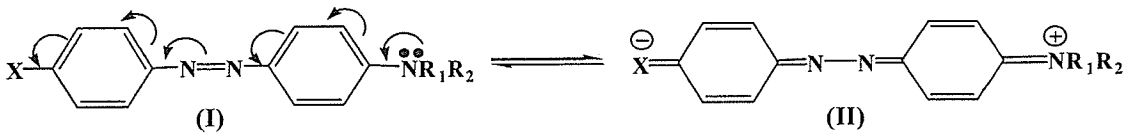

Figure 1.2.6: Canonical forms of a substituted aminoazobenzene

One of the more interesting characteristics of azo compounds is the *trans/cis* isomerization that can occur[36,56,64,66]. Figure 1.2.7 shows the two forms present with respect to azobenzene[65]. Studies have shown the *trans* form to be the predominant

form, which may change to the *cis* form upon irradiation, with a photostationary state between the two isomers achieved very quickly[35,42,56,64,66]. Cattaneo and colleagues have examined the mechanisms of the isomerization and discovered that there are two probable mechanisms of isomerization: Torsion around the N=N bond, or inversion of one nitrogen atom[64]. Through a series of intense computational models, they found that torsion is preferred for ground state or thermal isomerization, while inversion is favoured upon π-π^* excitation.

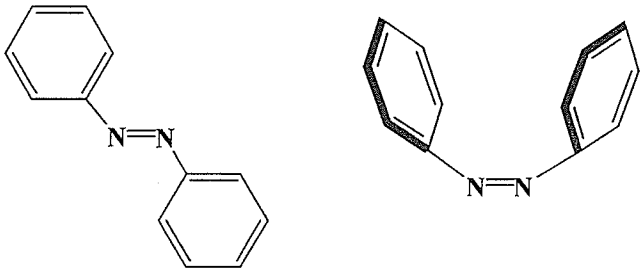

Trans-Azobenzene **Cis-Azobenzene**

Figure 1.2.7: Isomers of azobenzene

Due to the large difference in spatial arrangement between the two forms, the isomerization process may influence the absorption band. The isomerization of *trans*-azobenzene (TAB) illustrates this point. In TAB, the π- π^* excitation produces a visible maxima at 316 nm, while the n- π^* excitation produces a much weaker band at 447nm. The *trans* form may undergo photoisomerism to the corresponding *cis* form, which has the corresponding bands at 260 and 440 nm, for the π-π^* and n-π^* transitions, respectively[63]. However, given that the predominant form is the *trans*, and that substitution of the azo chromophore typically pushes the π-π^* band to longer wavelengths (overlapping the n-π^* transition), the change in the observed absorption

band tends to be limited. This however does not apply with regards to polarization, configuration, or electro-optical properties, and the photoisomerization of azobenzene dyes is the main reason why these compounds have been examined as potential molecular switches and photoresponsive materials[44,64,67].

iv) Substituent effects

As aforementioned, the resonance hybrids can affect the position of the visible absorption band. Because the wavelength of the visible absorption band is directly related to the energy difference between the ground and excited states (Equation 1.2.1), resonance theory concludes that any alteration to this energy difference, resulting from changes in electron migration between the two forms, will alter the visible absorption band, and hence the colour or the dye[53,63]. For example, if substituent "X" in Figure 1.2.5 exhibits electron-withdrawing capabilities, the migration of electron density will be enhanced, thus lowering the energy of the excited state (Form II), thereby shifting the absorption band to higher wavelength (lower energy). This type of shift of the absorption band to longer wavelengths is termed bathochromism[36,37,63,65]. This effect will also occur should "R_1" and "R_2", on the amino group, be electron donating (thereby increasing the 'donating power' of the donor component and stabilizing the excited state). If electron donating groups are present on the azo component, and electron-withdrawing groups on the donor group, then the shift either will be small, or the excited state will be destabilized to such an extent that the energy difference between levels increases, resulting in a shift to shorter wavelengths. This type of shift is termed a hypsochromic shift[63].

A large degree of the colour variation noted in azobenzene derived dyes is a direct result of substitution of the diazo or coupling component[36,43,58-59,63,66,68]. As already mentioned, the change in the visible absorption band arises from the degree of stabilization imparted by a substituent, and any substituent that stabilizes the excited state (Figure 1.2.5, form II) will reduce the energy difference between the states and result in a bathochromic shift. Thus, the substituent X on the diazo component can have a large influence on the position of the absorption peak depending on whether it withdraws or donates electrons (although no formal removal or donation of electrons actually occurs[49]). Bathochromism is typically caused by the presence of electron withdrawing groups, which allow greater stabilization of (II), thus bringing it closer in energy to (I). Electron-withdrawing groups in the para position typically produce the greatest shifts[53,58,66].

Substitution in the coupling residue will also affect the absorption maxima, although not necessarily in the same manner. Given that the degree of charge migration determines the position of the absorption band, the presence of electron donating groups on the coupler residue, or on the amino nitrogen, will bathochromically shift the band. A common example of this can be seen when the "R" groups on the amino nitrogen are alkyl. The 'donating power' of the donor component is increased, hence the bathochromic shift. However, should the alky chain itself be substituted with an electron-withdrawing group, such as a cyano, a hypsochromic shift can result. The cyano group effectively hinders donation though the conjugated system, thereby raising the energy of the excited state. The wavelengths of some substituted azo dyes of type (I), are given in Table 1.2.1[63].

Table 1.2.1: λ_{max} values of substituted azobenzene

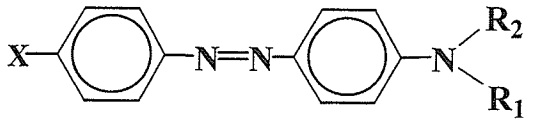

R_1	R_2	X	λ_{max} (nm)
H	H	H	385
H	Et	H	400
Et	Et	H	415
C_2H_4OH	C_2H_4OH	H	407
C_2H_4Cl	C_2H_4Cl	H	397
C_2H_4CN	C_2H_4CN	H	382
H	H	NO_2	444
H	Et	NO_2	468
Et	Et	NO_2	490
C_2H_4OH	C_2H_4OH	NO_2	475
C_2H_4Cl	C_2H_4Cl	NO_2	446
C_2H_4CN	C_2H_4CN	NO_2	432

The effect of electron-donating groups on the diazo component is not as straightforward as with electron-withdrawing effects. For example, while the addition of a methyl or a methoxy functional group to the diazo ring will not cause a significant change in the absorption band, the addition of a dimethylamino ($N(Me)_2$) group will result in a noted bathochromic shift[63]. This led Peters to postulate that the introduction of a dimethylamino group introduces an extra p-orbital with two electrons, which effectively raises the energy of the highest occupied orbital relative to the unoccupied orbital. Since this will lessen the energy difference between the two states, a bathochromic shift is expected[36]. Additionally, the addition of an electron-donating group to the diazo ring that already contains an electron-withdrawing substituent can result in a bathochromic shift, depending on the positions of the substituents[53,58,63]. A final example, of the somewhat non-intuitive effects that electron donating substituents may impart on the diazo ring system, can be seen in a comparison of julolidine and

lilolidine (Figure 1.2.8)[63]. When compared to the unsubstituted forms (X=H), if X=OMe julolidine displays a 10 nm bathochromic shift. However, the lilolidine structure displays a 8 nm hypsochromic shift. This is due to the limited ability of the terminal nitrogen of the lilolidine structure to conjugate with the aromatic system, when compared to julolidine[63]. The lack of conjugation results in a hypsochromic shift, which will increase as the electron donating power of the substituents on the diazo components increases. Table 1.2.2 provides λ data for the functionalized forms[63].

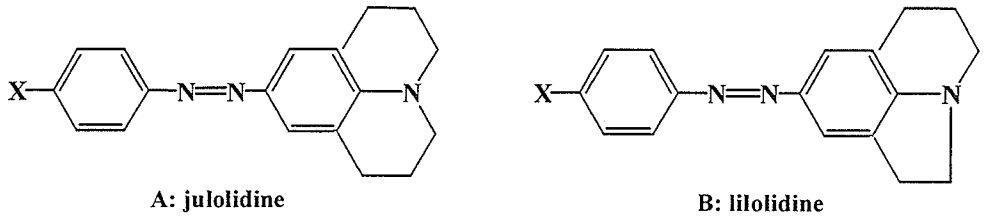

A: julolidine B: lilolidine

Figure 1.2.8: Julolidine and Lilolidine dyes

Table 1.2.2: λ_{max} values for substituted Julolidine and Lilolidine dyes

X	Julolidine λ_{max} (nm)	Lilolidine λ_{max} (nm)	$\Delta\lambda_{max}$ (nm)
OMe	452	417	35
Me	446	422	24
H	442	425	17
Br	464	448	16
CF_3	471	461	10
CN	496	487	9
NO_2	521	515	6

The general conclusion that electron-withdrawing groups may cause a bathochromic shift allows a correlation between λ_{max} and the Hammett constant of the substituent to be made. Previous reports have examined this phenomenon and attempted to draw relationships between the Hammett constant, σ, and the λ_{max} value, with

increasing λ_{max} values coinciding with increases in the value of σ[36,53]. The correlations strongly depend on the substituent pattern, and fail for ortho substituents. However, the general relationship is good for qualitative determination of the position of an absorption band. Hammett constants are the sum of the total electrical effects of a functional group attached to a benzene ring, and combine the inductive, field and resonance (or mesomeric) effects[49].

The inductive effect relates the degree of polarization of a bond, which is the direct result of polarization of an adjacent bond. For example, in chloroethane the carbon-carbon bond is polarized (towards the alpha-carbon) as a result of the electron withdrawing power of the chlorine substituent[49]. Field effects are similar to, but greater in importance than, inductive effects, and are transmitted through space (solvent) and not through bonds. Lastly, the resonance effect dictates the degree of charge density in an aromatic ring, as shown in Figure 1.2.9. In Figure 1.2.9, NH_2 is an example of a +M group, which donates electrons by resonance[49].

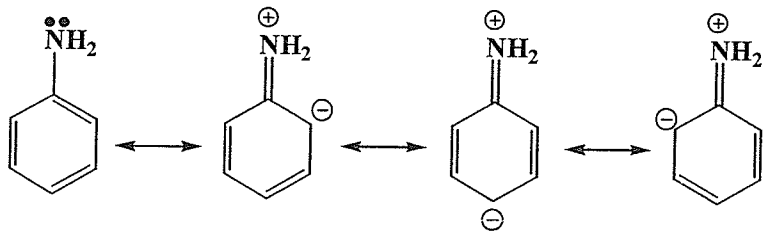

Figure 1.2.9: Resonance effect in aniline

v) Steric Effects

While the presence of electron-donating groups or electron-withdrawing groups aids in predicting the position of the absorption peak of a given dye, the position of the substituents may result in large deviations from the expected value[45,58-59,63]. The steric effects imparted by the substituents may alter the nature of the visible band, and it is for this reason that, for most substituents, one is not able to simply sum the Hammett constants to obtain a relative idea regarding the position of the absorption peak[63]. In particular, the steric effects associated with ortho substituents are typically greatest, hence the lack of any concrete Hammett constants for this position.

Steric hindrance of an azo dye is typically overcome by a rotation around a single bond. This rotation, as a rule, results in less p-orbital overlap for the system, and thus raises the energy of the excited state (relative to ground), causing a hypsochromic shift in the visible band[63]. Figure 1.2.10 portrays the relative energy levels of the ground and excited state when the system is sterically hindered[63].

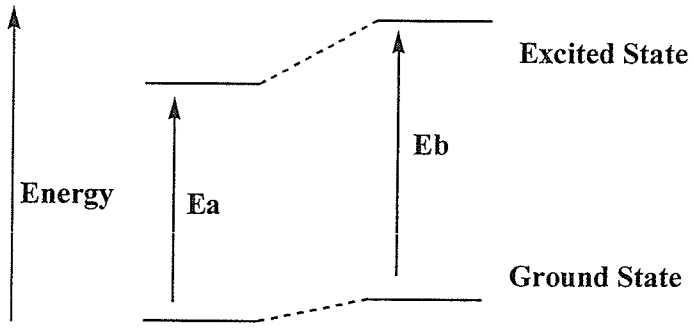

Figure 1.2.10: Change in energy between a planar (a) and a sterically hindered (b) dye

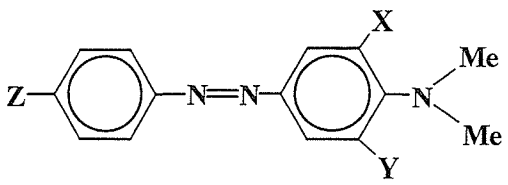

Figure 1.2.11: A sterically hindered aminoazobenzene

A generic sterically hindered azo dye is displayed in Figure 1.2.11. Should X=Y=Z=H the visible absorption band would be found in the longer wavelength region. However, should even one of X or Y be a substituent of reasonable size (such as X=Me, Y=Z=H) a hypsochromic shift of 33 nm is observed relative to the unsubstituted dye[63]. In this particular instance, the electronic effects imparted by the methyl groups on the terminal nitrogen are overcome by the steric effects imparted by the methyl substituent on the coupler ring, thus a hypsochromic shift is observed. Interestingly enough, an even greater hypsochromic shift is observed when $Z=NO_2$. A non-sterically hindered system would benefit from a bathochromic shift from the presence of a 4'-nitro substituent. However, the greater electron-withdrawing effect of the nitro substituent enhances the electron donating power of the terminal amino, thus making the amino C-N bond of a higher π-character. Rotation around this bond is therefore more strained than compared to a conventional sigma bond, thus raising the energy of the excited state further, which results in a greater hypsochromic shift (the opposite of what conventionally would be expected for a 4'-nitro substituted azobenzene)[63].

Additionally, the nature of the substituents on the terminal amino nitrogen may also affect the absorption band. In the case where both substituents are β-cyanoethyl

(-CH_2CH_2CN), the partial negative charges that reside on the cyano functional group cause repulsion between these two groups, resulting in a loss of planarity of the system. This may result in a smaller hypsochromic shift than would be expected normally. This effect also applies to the OH groups of β-hydroxyethylanilines[45].

Steric effects encountered as a result of the position of substituents on the diazo component are also noteworthy. The presence of bulky substituents on the 2'- and 6'-positions (ortho to the azo bond) on the diazo ring can reduce the effectiveness of the coupler residue to incur a bathochromic shift[59]. Commonly, the larger the substituent, the greater the effect, with certain cases resulting in the substituted dye having a lower wavelength of absorption than the unsubstituted dye[58]. The one exception to this is the cyano group, due to its rod-like structure[63]. Otherwise, the presence of any other substituent ortho to the azo bond will result in a sterically hindered molecule. Figure 1.2.12 presents an example of an azo dye sterically hindered by diazo substituents[63].

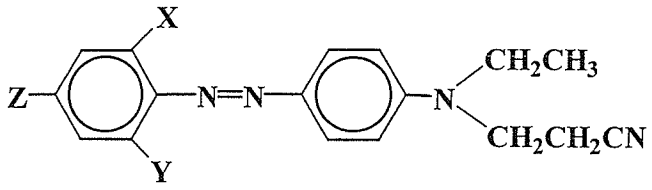

Figure 1.2.12: A 2'- 6'-substituted aminoazobenzene (Eg. X=NO_2, Y=COC_2H_5)

Hallas and colleagues have examined the effects of ortho substituents and have explained that the presence of a methyl substituent causes an overlap of the orbitals with the lone electron pair of the β-nitrogen of the azo group, Figure 1.2.13[58,63]. This results in a rotation around the C-N bond to alleviate the strain. However, should X=Y=Me, the steric effects cannot be overcome by the simple rotation shown in Figure 1.2.13, thus a

large hypsochromic shift is observed (383 nm, Z=NO_2) when compared to the parent dye (453 nm, X=Y=H, Z=NO_2)[63]. Thus, with regards to conventional textile production of azobenzene derived dyes, it is sterically disadvantageous to incorporate large substituents in the 2'- or 6'- positions due to the loss of colour which would be observed.

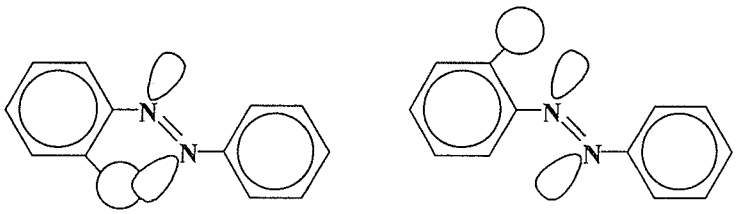

Figure 1.2.13: Rotation around C-N bond to alleviate steric strain

vi) Hydrogen bonding

An interesting property of azo dyes is their ability to exist in the azo form, or the hydrazone form (Figure 1.2.14)[14,35,69]. Equilibrium between the two forms is typically achieved very quickly, and is solvent affected. This phenomenon has been well studied since the early 1900s when it was discovered that formation of a hydrogen bond between an azo nitrogen and a nearby hydroxyl (Figure 1.2.15), may favour the azo form, since there would not be a removal of the hydrogen from the oxygen[35].

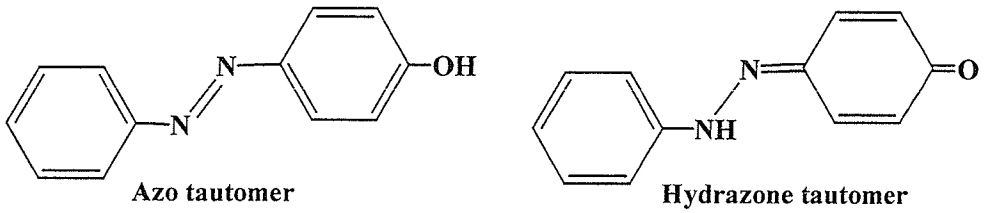

Figure 1.2.14: Azo-Hydrazone tautomers

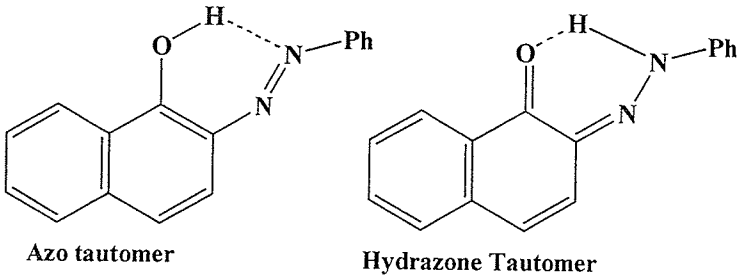

Figure 1.2.15: Intramolecular Hydrogen bonding

Typically, the formation of an intramolecular hydrogen bond results in a bathochromic shift, which is evident when comparing the spectra of those dyes illustrated in Figure 1.2.16[53]. The parent dye (R=H) absorbs at 486 nm while the substituted dye (R=COOH) absorbs at 493 nm due to the hydrogen bond that forms between the carboxylic hydrogen and the α-nitrogen of the azo group[53]. The phenomenon of hydrogen bonding or protonation of the azo nitrogens is closely related to the acidic tautomeric equilibrium discussed below.

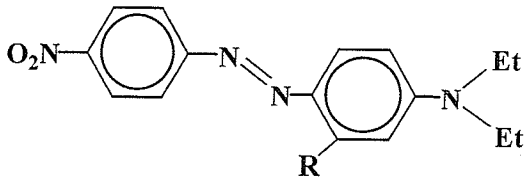

Figure 1.2.16: H-bonding (R=COOH, OH, NH_2) in ortho-substituted azobenzenes

vii) Thiophene derived azo dyes

Generally, the nature of bathochromic or hypsochromic shifts resulting from substituent effects, which apply to azobenzene dyes, also apply to the thiophene derived azo dyes, and there have been a number of papers exploring the properties of thiophene related azo dyes[50,60-62,68,70-74]. The presence of the sulphur atom within the

ring structure of the diazo component acts as an additional electron-withdrawing group, due to the available 3d orbitals. In addition, substituent effects tend to be more effectively transmitted than when compared to azobenzenes, due to the diene-like character of the thiophene ring. Thus the presence of a nitro substituent on the thiophene ring will cause a larger bathochromic shift than observed for the analogous azobenzene[68]. Furthermore, the fact that the thiophene ring system has less resonance stabilization than benzene typically results in a bathochomic shift for the dyes due to the difference in energy between the ground and excited states being lessened[60,68]. This is illustrated by comparing the two examples given in Figure 1.2.17[68]. The azobenzene dye absorbs at 463 nm in ethanol, while the nitrothienyl derived dye absorbs at 573 nm.

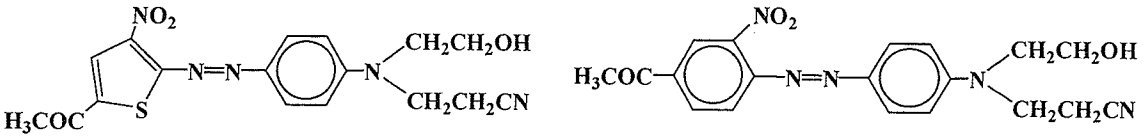

Figure 1.2.17: Comparison of an benzene and a thiophene derived azo dye

viii) Solvent effects

Absorption bands arising from n-π^* transitions typically exhibit a hypsochromic shift on increasing solvent polarity. Conversely, π-π^* transitions display bathochromic shifts[55]. Since, with respect to azobenzene dyes, the π-π^* transition is of greater significance, bathochromic shifts are expected. Upon changing polarity from a less polar to a more polar solvent, if a bathochromic shift is observed, the dye is said to exhibit positive solvatochromism. Conversely, should a hypsochromic shift be observed, it would be termed negative solvatochromism. With regard to 4-

aminoazobenzene dyes, the ground state is less polar than the excited state (Figure 1.2.5 (I) and (II), respectively). Thus, a polar solvent will typically have little effect on the ground state (I), but will greatly stabilize the dipolar excited state (II)[63]. The stabilization of the excited state will cause a bathochromic shift, analogous to how electron-withdrawing groups in the diazo component stabilize the excited state. The presence of water in the solvent may also create a bathochromic shift, through intermolecular hydrogen bonding. However, this effect may be counteracted by intramolecular hydrogen bonding which prevents water molecules from encroaching on the azo bridge[61]. The nature of water effects is readily explained by examining the effect of acidic media on the visible absorption profile of a dye.

Acidic conditions remove the n-π^* band and shift the absorption band by creating a tautomeric equilibrium between the azo dye and its protonated form[35,53,56,60,63]. The change in the absorption peak of the protonated analogue, when compared to the neutral form, is termed halochromism. Positive halochromism represents a bathochromic shift, while negative halochromism a hypsochromic shift. Figure 1.2.18 shows the protonation sites of an aminoazobenzene derived dye[63]. Increasing the acidity of the solution will, typically, create two distinct absorption bands, one in the 320 nm region, the other falling in the range of 500-550nm. The former band is attributed to protonation of the amino nitrogen, form (II) in Figure 1.2.18, while the longer wavelength band is attributed to form (III). The reason that the ammonium cation falls at a lower wavelength arises from the fact that the effective electron-donating power of the terminal amino substituent is reduced upon protonation, thus resulting in a hypsochromic shift.

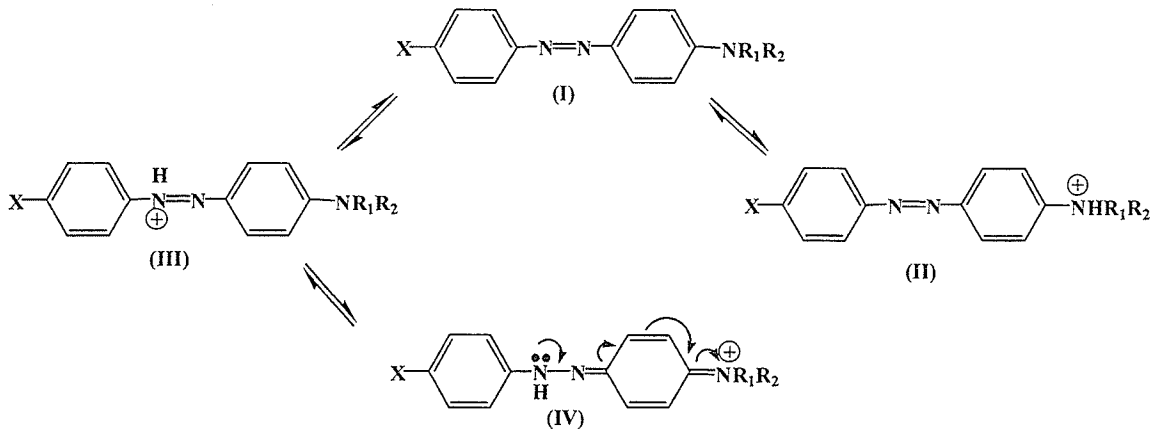

Figure 1.2.18: Tautomeric Equilibria existing in acidic solution

Forms (III) and (IV) in Figure 1.2.18 represent the charge-resonance system of the azonium cation[63]. It is interesting to note that (IV) best represents the ground state, thus the visible absorption band is attributed to a migration in electron density away from the β-nitrogen atom (the opposite of neutral dyes). Thus, the presence of electron-withdrawing groups in the azo component (X=EWG), results in a lessening of the expected bathochromic shift[53,63,65]. Conversely, the presence of electron donating groups in the azo component will result in an increased bathochromic shift, or greater positive halochromism. Figure 1.2.19 presents the relative energy levels of the azonium cations when the substituents display electron-donating (a) and electron-withdrawing (b) properties[63,65]. Ea (the energy gap for an azonium cation containing electron-donating groups) is smaller than in the neutral from due to an electron-donating group increasing the energy of the ground state but stabilizing the energy of the excited state, while an electron-withdrawing group will stabilize the ground state in addition to increasing the excited state, thus increasing the energy gap (Eb).

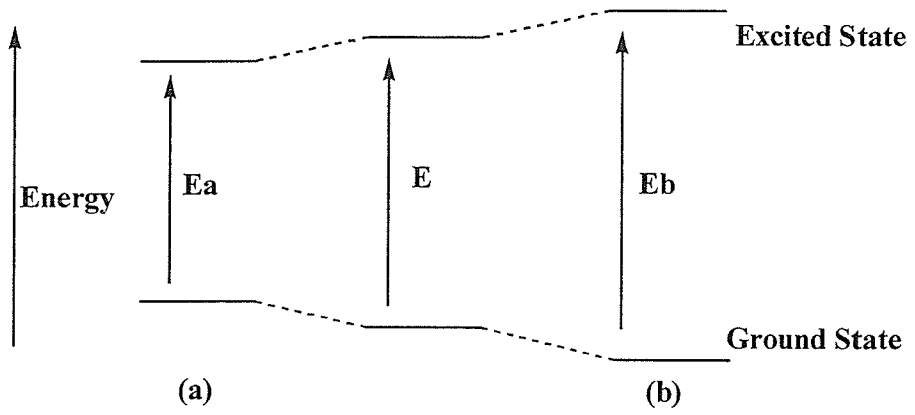

Figure 1.2.19: Comparison of energy levels between electron-donating substituents (a) and electron-withdrawing substitutents (b) on an azonium cation

The presence of electron donators in the coupler residue will have a large effect on the basicity of the β-nitrogen atom, since the electron density on the β-N will be greater with increasing electron-donating ability of the substituents. The increased basicity will result in a higher degree of protonation at this site[35,63]. Alternatively, should there exist a substituent in the 2' or 6' position of the diazo component, then overlap of the substituent with the lone pair (Figure 1.2.13) will occur and result in decreased protonation due to steric hindrance[63].

1.2.3 Novel Frontiers for Azobenzene compounds

Traditionally, the role of azobenzene related dyes have focused on the colouring of textile products, with the original application being to cover up the natural discoloration of early plastics[67]. The inclusion of azo compounds into polymeric materials was largely limited to dyeing of natural and synthetic fabrics such as polyester, cellulose acetate, and nylon, and numerous reports are given detailing the so termed 'fastness properties' of these dyes on the respective fibers[36-37,43,58-59]. However, with the explosion of macromolecular science, azo compounds began to be used more and more to simply increase the attractiveness of polymeric materials[67].

One of the main drawbacks to early colouring of fibers was the inability of the colour to persist over time. Every class of dye behaved in a slightly different manner, and fading, as a result of wash out, or chemical change, was a genuine concern. It was for this reason that researchers began to examine the possibility of covalently bonding the dye chromophore to the polymeric material in the attempt to synthesize a 'permanently' coloured plastic. Millikan was one of the first to succeed, by producing a coloured polyurethane as shown in Scheme 1.2.2, where R is the azo chromophore[67]. The benefit of these polymeric dyes lies in the combination of their macromolecular properties with the colour characteristics of the dye[33].

Scheme 1.2.2: HO-[R]-OH + OCN-[R']-NCO $\rightarrow$ -(-O-[R]-OCONH-[R']-NHCO-)-$_n$

In addition to the dyeing of fabrics and conventional plastic materials, a newer branch of polymer chemistry has emerged in the past decade. This being the switch

from the design of structural linkages to functional linkages. Conventionally, polymer chemists were more interested in the bulk properties of the polymer, and less so on the actual functionalization of the polymer. Thus, a polyester, for example, was characterized by its molecular weight and not by any specific reactivity or property of the ester functional group[44]. However, with recent developments in photoresponsive materials, electro-optical properties and electronic storage devices, there has been a movement towards functional polymers that are tailor made for a specific function as a result of the specific functional group used in the synthesis[44,75]. A distinction needs to be made from methods utilizing polymers as supports for specific functional groups, and functional polymers. The latter may have the functional group placed in the backbone, side chain, crosslink, etc, while a supported functional group is almost always positioned as a side chain (since the polymer serves as a 'carrier' only). Moreover, a functional polymer will undergo a transformation if the functional group changes, whereas a support polymer will typically not exhibit any changes when the functional group is altered[44].

Azo compounds are uniquely suited for use in functional polymers, given that they may undergo photo-induced isomerization (which alters the polarity of the molecule), and that the chromophore units are characterized by efficient electron mobility[44]. Interestingly, with regards to textile applications, the isomerization of azo compounds was conventionally looked upon as a detriment, since the colour could alter slightly and become duller with formation of the *cis* form[63]. However, with the advent of functional polymers, the previous isomerization 'problem' has created a whole new

area of polymer research. The numerous applications for functional polymers incorporating the azo functionality are summarized in Figure 1.2.20[43].

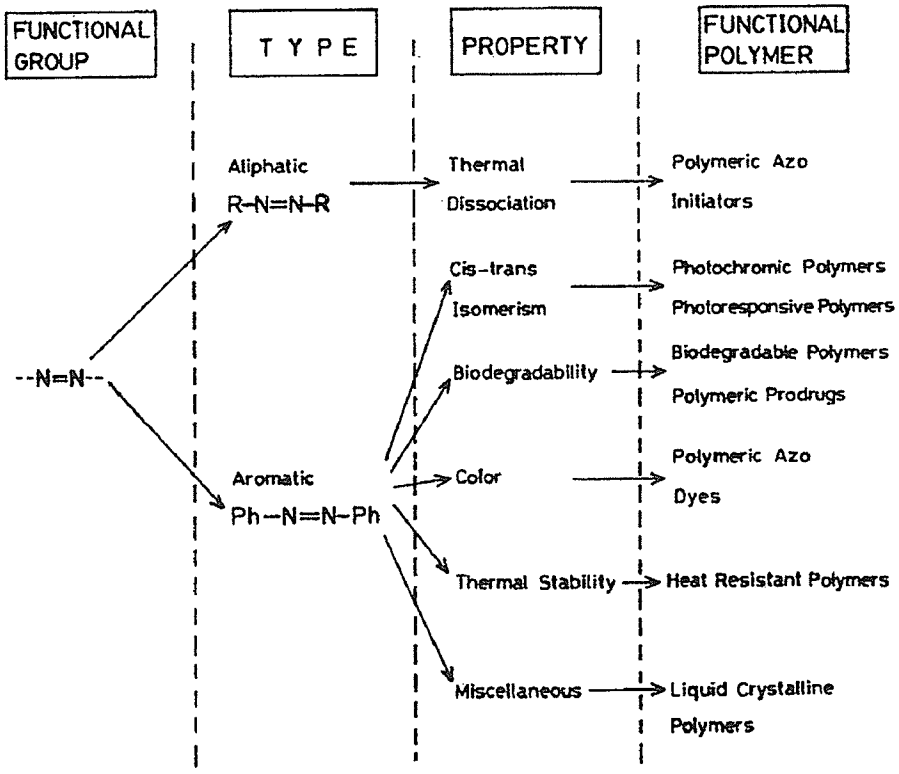

Figure 1.2.20: Functional Approach to Polymer applications

i) Nonlinear Optical Properties

It is necessary to explain, albeit briefly, the basis of nonlinear optical (NLO) properties and why azo compounds are of interest as second order non-linear optical molecules. The examination of non-linear optical properties touches many disciplines of science from chemistry and physics to material science. Non-linear optical properties arise from the interaction of an electric field (*i.e.* a light source) with a molecule, thus

polarizing it. These interactions vary depending on the molecules, and range from a change in refractive index to emission of light. In the case of a molecule that displays *linear* optical properties, the refractive index is independent of electric field, and any emitted light is of the same frequency of the parent. This is not true for non-linear behaviour. It is this non-linear response to the electric field that provides the useful properties now being exploited[76-78].

The field of non-linear optics can be referred to as photonics, in analogy to electronics (with photons taking the place of electrons)[76]. The drive towards optical devices has progressed considerably in the past decade, and is spurred by their improved speed (optical switches can be orders of magnitude faster than their electronic counterparts), and their ability to be relatively free of electronic and magnetic interferences and 'cross-talk'[76].

Two of the larger applications with regard to non-linear optical properties reside in the use of electro-optic devices and second harmonic generators (SHG). Electro-optic devices are those which exhibit a change in refractive index, while SHG are immanently useful for optical storage devices. The benefit of SHG (also termed frequency doubling) arises from the fact that the storage capacity of a focused beam of light is proportional to the frequency of the light. Thus SHG (which produces light of double the original frequency, and thus lower wavelength) can alter infrared light into blue light, thus increasing optical data storage capabilities[55,57].

The types of compounds exhibiting NLO properties are diverse. However, in general, a mobile set of π electrons is needed. Thus polymers (including conjugated and those with side chain chromophores), azo compounds, heterocycles, and transition metal

complexes (such as ferrocene derivatives) have been examined[76-84]. In general, polymers are the most familiar type of non-linear media employed, and commonly have their chromophores aligned in such a way (termed 'poling') as to maximize their non-linear optical properties. Poling requires the application of an electric field at temperatures near the glass transition temperature of the polymer. Polymers incorporating dyes potentially allow for the poling process to be followed visually. Polymers incorporating the dye Disperse Red 1 (Shown in Figure 1.2.21) displayed a colour change from red/orange to purple during the poling process, thus the degree of poling could be followed based on the change in the absorption band[78]. Azo dyes themselves are classified as second order non-linear optical materials, which accounts for their ability to be used as SHG and electro-optical devices[76]. Incorporation of these dyes into polymer systems may result in interesting properties ranging from photoviscosity and photomechanical properties to alteration of solubility with irradiation[44].

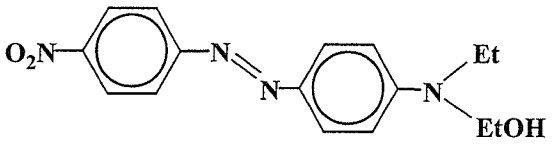

Figure 1.2.21: Disperse red 1

ii) Polymers containing the azo functionality

As outlined above, azo compounds display second order non-linear optical properties, and the isomerization associated with these compounds is of interest with respect to functional polymers. The benefits of incorporating the azo functional group

into a polymeric material are manifold. In addition to the fact that the chromophore allows one to study the orientation and structure of the polymer, the morphology, glass transition temperature, solubility, and thermoproperties of the polymer may change with isomerization of the chromophore[85-87]. Thus, functional polymers utilizing azo groups may be used in liquid crystal display devices, thin film sensors, and as optical connectors and data storage devices[88-90].

Polymers may incorporate azo chromophores as side chains or as part of the polymer backbone. Moreover, it is possible to diazotise the polymer post polymerization. For example, Scheme 1.2.3 illustrates the coupling reaction used to prepare a functionalised poly(acrylic acid) polymer[88]. The resulting multi-layer polymer films displayed a SHG effect without poling, which was attributed to a well-ordered chromophore film resulting from layer by layer post azo functionalization[88].

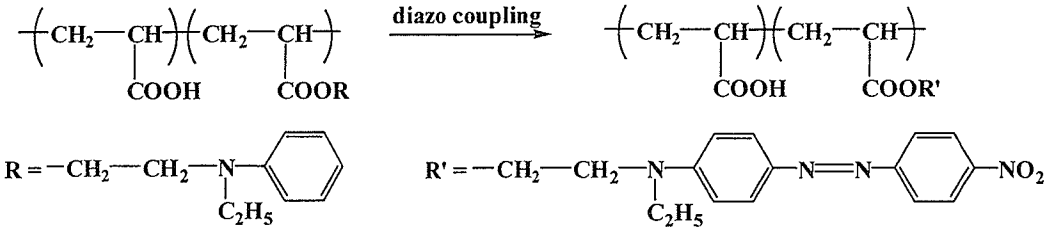

Scheme 1.2.3: Post polymerization diazotization

Wang and colleagues utilized a similar post polymerization coupling to produce polyelectrolytes (PEL). The UV properties of these azo compounds did not change upon inclusion into the polymer, and the polyelectrolytes displayed isomerization rates that were dependant on the structure of the azo chromophore. Moreover, as a result of the azo chromophore, the PEL displayed optical dichromism that could be erased and rewritten. These types of polymers show promise as unique ultrathin multilayers, and

stimuli responsive materials[87]. A recent report by Natansohn and colleagues outlined the preparation of azo-tetraphenyldiaminobiphenyl polymers that exhibited photoconduction and electro-optic properties (Figure 1.2.22). They found that increasing the concentration of the azobenzene group in the polymer caused a bathochromic shift. This is in contrast to the normal hypsochromic shift associated with increasing the concentration of azobenene groups present as side chains, which is explained in steric terms as an anti-parallel arrangement of the side chains. With regards to the azo-tetraphenyldiaminobiphenyl polymers, the authors surmised that the polymer was not flexible enough for a significant anti-parallel arrangement to occur[90].

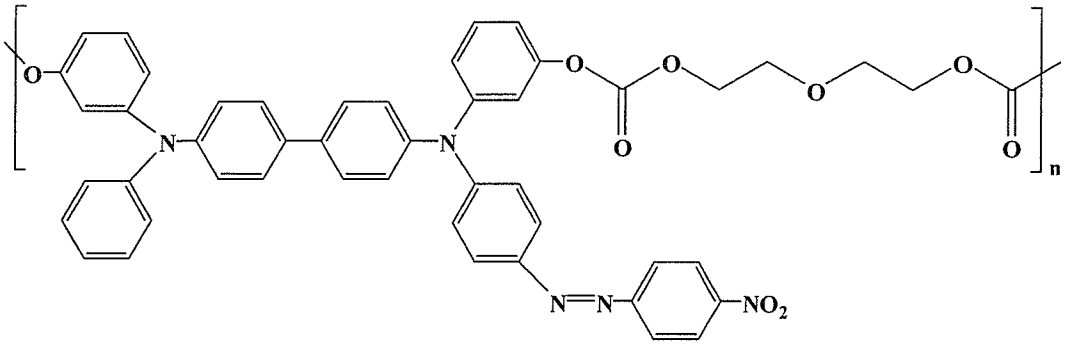

Figure 1.2.22: Azo-tetraphenyldiaminobiphenyl polymer

Inclusion of the azo chromophore into the backbone of the polymer has also been examined[89,91]. McGrath and colleagues examined the isomerization of an azo dendrimer, which displayed a large change in conformation with the corresponding isomerization. The formation of the cis isomer altered the absorption profile of the dendrimer, but was reversible upon relaxation in the dark or irradiation with sunlight[89]. Figure 1.2.23 illustrates the changes induced by isomerization[89].

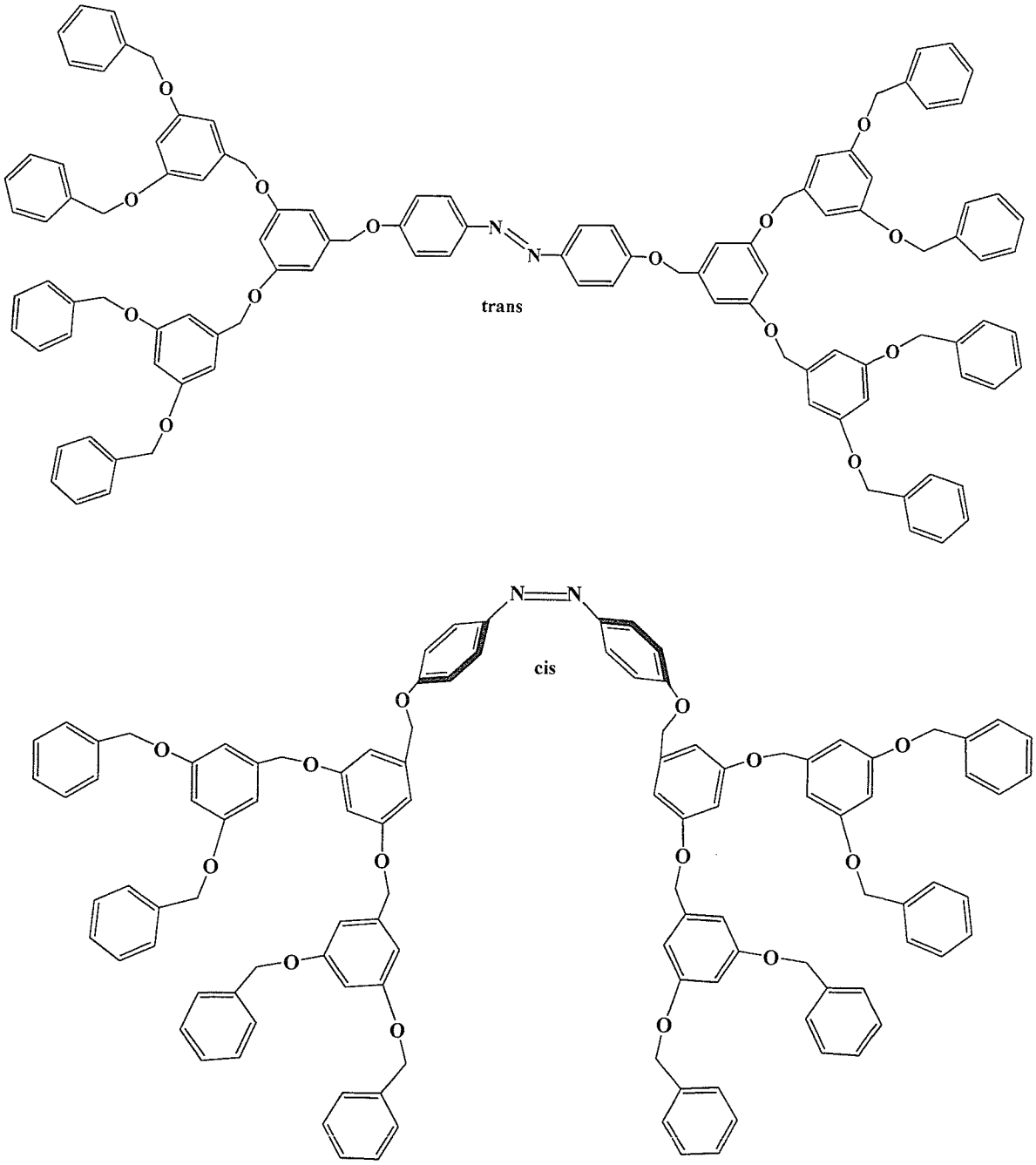

Figure 1.2.23: Photoresponsive dendrimer

Another recent report has communicated the preparation of polymeric catalysts containing azo dyes (Figure 1.2.24)[92]. The polymers are soluble and allow facile monitoring of catalyst concentration, and separation and recovery from the reaction

mixture[92]. The organic catalyst was reusable for up to four cycles with no significant loss of activity. The catalyst incorporating palladium was less robust, as some decomposition was observed upon use[92].

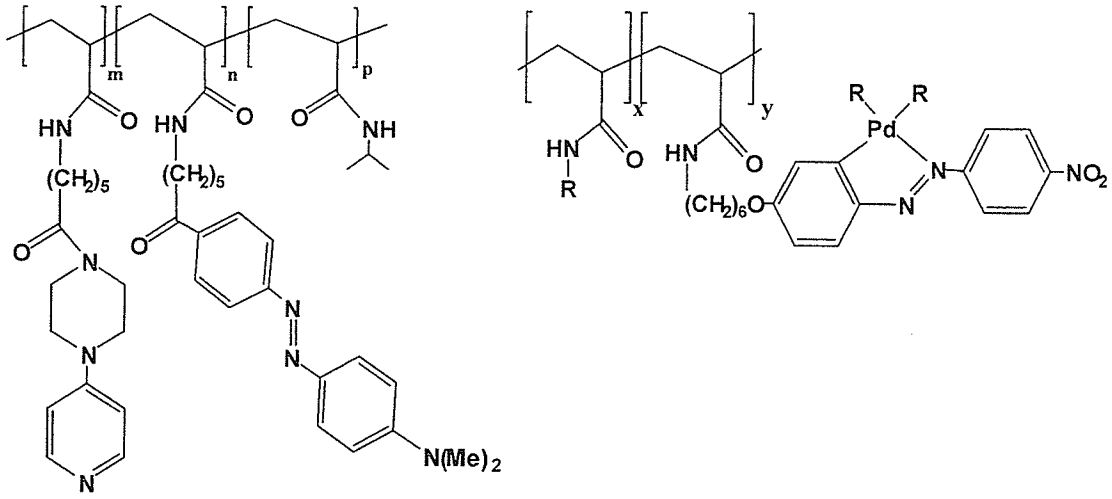

Figure 1.2.24: Azo-catalysts

iii) Azo dyes incorporating transition metals

The inclusion of transition metals into polymers or compounds containing azo functionalities allows one to harness the benefits associated with the transition metal (redox properties, magnetic characteristics, reactivity) in addition to those of the polymer (mechanical properties, processability) and the azo dye (colour, photochromism, solventochromism)[93]. These compounds can exhibit unique electronic properties, and can be used as liquid crystal devices, fluorescence quenchers or highly coloured polarizable polymers[93-96].

Two recent papers have examined rhenium and rhodium complexes incorporating azo chromophores[97-98]. The complexes, illustrated in Figure 1.2.25, displayed intense bands in the UV and visible region of the spectrum[97-98]. The Re complex displayed an absorption band arising from charge transfer between the metal

and the diimine[97], while the Rh complex displayed distinct bands in the UV region from transitions within the ligand orbitals and a band in the visible region attributed to an intra-ligand charge transfer[98]. In addition, the cyclic voltammegram of the Rh complex displayed an oxidation potential that was dependant on the nature of the substituent R. The potential increased linearly with increasing electron-withdrawing power of the substituent, for example, $E_{1/2}$: OMe, H, NO_2: 0.65V, 0.81V, 1.10V, respectively[98].

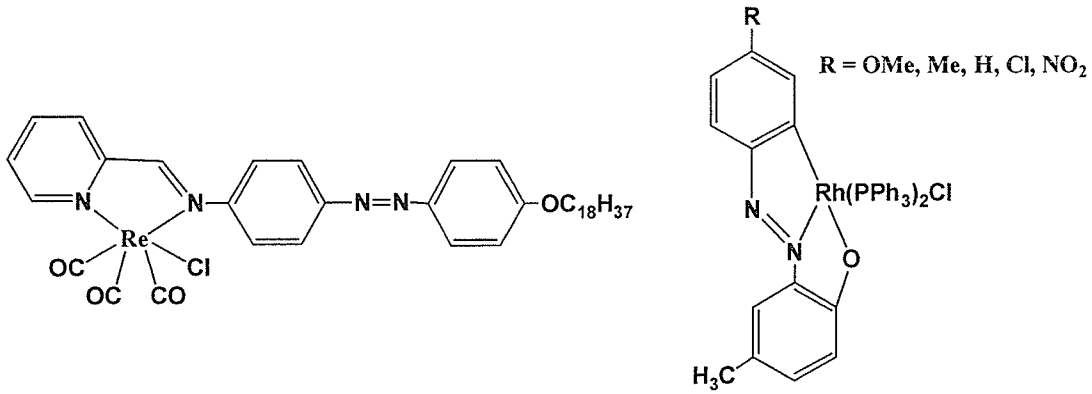

Figure 1.2.25: Re, Rh complexes incorporating azo chromophores

Other research has focused on ferrocene and its effect on dye properties. Tian and colleagues have examined the presence of ferrocene in small dye structures (Figure 1.2.26 A, B)[94,95]. The presence of the ferrocene unit reduced the excited state of the naphtalimide dye through intramolecular electron transfer, and the quenching was observed to decrease upon oxidation of the ferrocene unit. Nishihara and coworkers also examined ferrocene in oligomers and polymers bridged with azo units (Figure 1.2.27)[96]. The organometallic compounds displayed longer wavelength bands than azobenzenes, and displayed altered absorption peaks with oxidation of the ferrocene units. A band at 672 nm was observed upon oxidation that was attributed to a ligand to metal charge transfer band from the π orbital of the azo group to a Fe(III) *d* orbital[96].

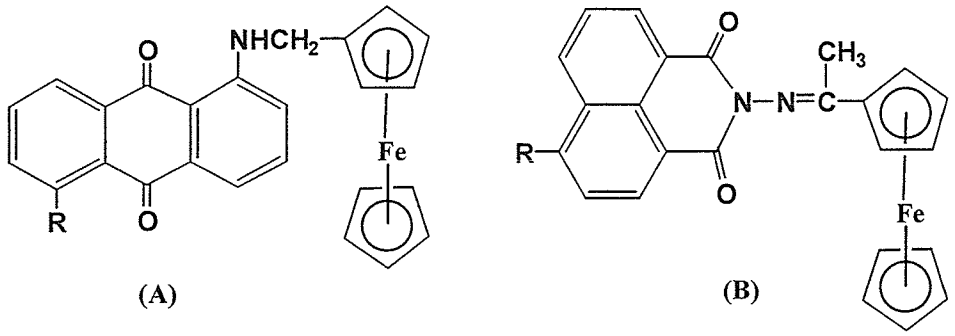

Figure 1.2.26: Ferrocene based dyes

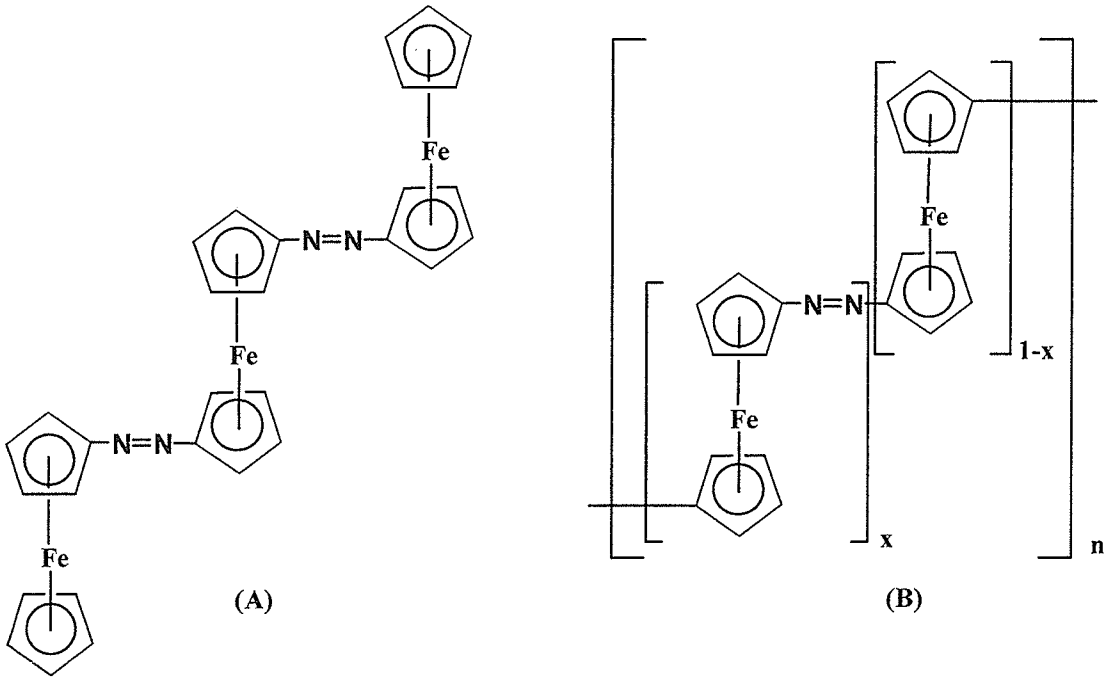

Figure 1.2.27: Azo bridged ferrocene oligomer (A) and polymer (B)

Continuing the work on ferrocene polymers, Manners *et. al.* have examined the poly-(ferrocenylsilanes) illustrated in Figure 1.2.28[93]. The polymers are potentially

useful as non-linear optical materials, and displayed interesting thermal properties, as the melting and thermal decomposition of the polymers occurred at a lower temperature (150-180°C) than the uncoupled azo compound and parent polymer (approximately 300°C)[93].

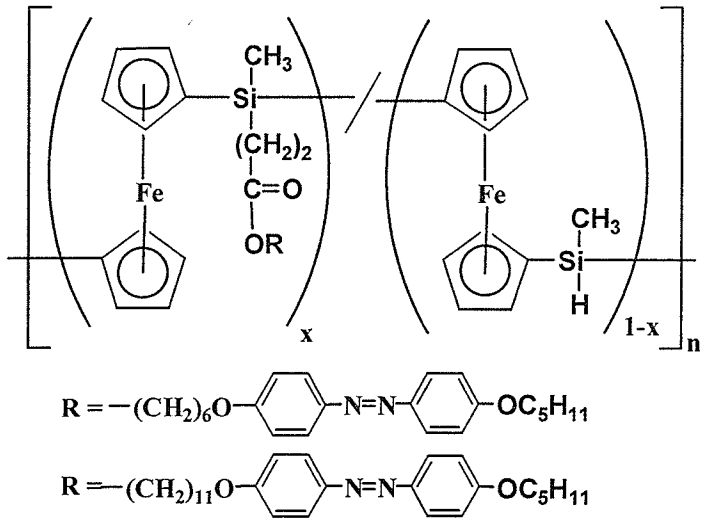

Figure 1.2.28: Poly-(ferrocenylsilane)

1.2.4 Photochemical and Thermal Stability of Azobenzene derived dyes

i) Introduction

The earlier studies pertaining to degradation of azobenzene related dyes focused on the colour of dyed fabrics, and thus much of the work was concerned principally with the fading of colour from the fabrics over time or with irradiation[42,57,69,99]. A minor amount of work was done in organic solvent systems, however development of light-fastness properties proceeded with respect to the fibers themselves, and not photochemical theory[100-102]. A large majority of the early research studied effects that were observed for aminoazobenzenes substituted in the diazo component ortho to the azo bridge (positions 2', and 6').

Investigations into these types of substituted azo compounds found that the presence of an ortho substituent may adversely affect the stability of a dye. In particular, the presence of an ortho nitro group (structure shown in Figure 1.2.29) prevents electron delocalization along the azo bond, due to the proximity of the oxygen[42]. This localization of electron density on the azo group causes the C-N bond near the coupling component to become amenable to scission[42,69].

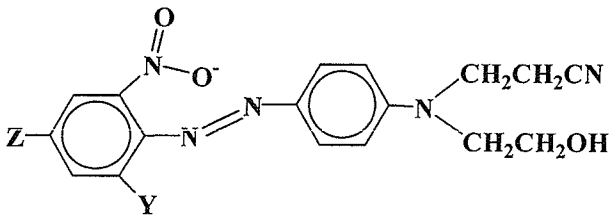

Figure 1.2.29: A 2'-nitro substituted aminoazobenzene

With respect to azo dyes, degradation processes typically occur via a reductive or oxidative mechanism. Studies involving the photoreduction of an azo dye have shown

the presence of a substituted hydrazobenzene, as shown in Figure 1.2.30[57]. However, reduction processes typically will not occur in the presence of oxygen, and indeed for certain instances, the photoreduced product was observed to reform the parent azo dye when oxygen was brought back into the system[101]. Oxidation processes are thus more common, and typically result in the formation of aromatic amines, however product identification is difficult at best[57]. Oxidative degradation causes a hypsochromic shift in the absorption band and, with respect to dyed fibers, usually results from excessive humidity. With regards to solution chemistry, oxidation processes are quite common, and may be initiated via a number of different compounds.

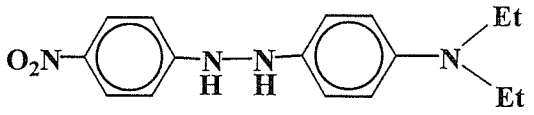

Figure 1.2.30: Hydrazobenzene structure

ii) Remediation of azo dye contaminants

As mentioned above, the initial interest in dye stability was focused on industrial and consumer concerns. However, with the increased awareness, beginning around the 1970s, of water quality and textile waste, there has been a large shift to the examination of remedial techniques with regards to azo dyes. Of particular concern is that, being highly coloured, an azo dye present in solution at a concentration of 1 mg/L is still visible[103]. Azo dyes are the largest class of dye compounds used, and while their environmental input (low tonnage/day) is lower than other contaminants of interest (for example, pesticides and detergents which have emissions on average of 1000s tons/day)[105], the aforementioned colour problem combined with their tendency to resist

degradation processes pose considerable environmental concerns[104-106]. Of particular note is that many dyes are not biodegraded in aerobic conditions found in conventional sewage treatment plants, and are not readily degraded via the direct absorption of visible or ultraviolet light[105]. In addition, while the acute toxicities of azo dyes are generally low (1000-2000 mg/kg), the chronic toxicities are somewhat of an unexplored field, although there have been a number of dyes that have exhibited carcinogenicity in rats[105]. It is for the above reasons that new rigorous water quality guidelines have been imposed, especially in Europe, on wastewater effluent[107]. Although dyes enter the environment via manufacturing, industrial colouration plants and even household use, by far the greatest contributor is the textile colouration industry[105]. Thus there has been a push to generate new, cost effective, remediation techniques with respect to this problem. These newer techniques tend away from flocculation and coagulation processes that simply transfer the pollutant from one phase to another[108-110].

Oxidation techniques have become one of the methods of choice for the removal of dye contaminants in aqueous systems. The primary benefit is the potential for these processes to be implemented within the textile plant itself as a pre-treatment for effluent. This pre-treatment would either completely oxidize the dye, or oxidize it to a lower molecular weight product that can be efficiently removed by conventional municipal water treatment facilities[111]. The most common form of oxidation technique involves the use of hydrogen peroxide, which upon formation of hydroxyl radicals, tends to liberate the azo bond as molecular nitrogen quite quickly[107-111]. A large majority of the research performed in this field has focused on the degradation of anionic azo dyes as shown in Figure 1.2.31[110,111].

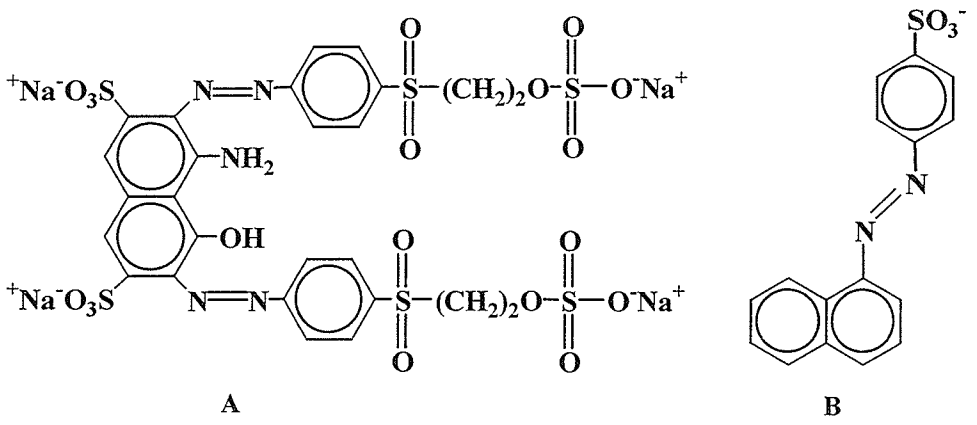

Figure 1.2.31: Examples of azo dyes studied in aqueous oxidation studies

The presence of hydrogen peroxide in irradiated solutions creates the reactive hydroxyl radical which is responsible for the destruction of the organic compound. The generic reaction sequence is provided in Scheme 1.2.4, where RH is a dye molecule[110]. The lifetime of a hydroxyl radical is very short (approximately 70 ns) and the diffusion of the radical in aqueous systems is approximately 2 $x10^{-5}$ cm^2/s, therefore, any oxidation reaction that may destroy an organic compound must occur where the radical is formed, in the aqueous solution. Thus, hydrogen peroxide is not amenable to the destruction of heterogeneous contaminants that are not dissolved in the aqueous phase[107]. Results have indicated that regardless of the dye chosen, that a large majority of the destruction of the dye and colour loss occurs rapidly in the first several minutes of photolysis, with subsequent removal of total organic carbon (TOC) with further irradiation[110].

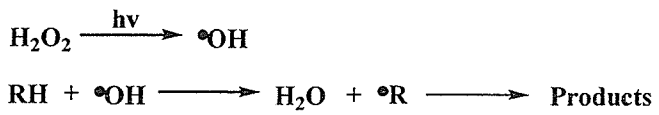

Scheme 1.2.4: Oxidation of an organic molecule initiated by UV-hydrogen peroxide

There are varying techniques of oxidative removal available for organic dyes. One such technique utilizes ferrous ions in conjunction with hydrogen peroxide (Fenton reagent). The Fenton reaction (and photo-Fenton reaction, which incorporates UV light) has been used largely in the destruction of Orange II (structure B in Figure 1.2.31)[112-113]. The reaction scheme for the photo-Fenton process is given in Scheme 1.2.5[112]. One of the possible drawbacks to this process is the release of Fe ions in higher concentrations than allowed by EEB (European Environmental Bureau) regulations (2 ppm). However, Kiwi *et. al.* have used ferrous ions sorbed to a Nafion fiber to limit the movement of the ions, and have found that although attached to the fiber, the ferrous ions do successfully aid in the degradation of Orange II[113].

$$Fe^{+2} + H_2O_2 \longrightarrow Fe^{+3} + OH^- + {}^{\bullet}OH$$

$$Fe^{+3} + H_2O \xrightarrow{h\nu} Fe^{+2} + {}^{\bullet}OH + H^+$$

Scheme 1.2.5: The photo-Fenton process

A recent report by Hoffmann outlined the use of ultrasound combined with aqueous ferrous ions[114]. Sonochemical methods utilize the cavitation bubbles that form in a solvent exposed to ultrasonic radiation. A sonochemical reactor utilizes compression cycles that lower the magnitude of the bubble size (by increasing the pressure), thus causing very high temperatures and pressures to exist inside the bubble cavity. It has been estimated that temperatures between 4000-5000 K, with pressures on the order of hundreds of bars, can exist inside the compressed bubble cavity. These conditions cause water molecules within the cavitation bubble to form both ·OH radicals and ·H radicals that may spontaneously initiate degradation of an organic compound.

Volatile compounds may be degraded by diffusing into the cavitation bubble, while non-volatile contaminants may undergo degradation via the radicals that diffuse out of the bubble and into the bulk media. Hoffmann examined the degradation of azobenzene and a selected number of related dyes and found that the ortho substituted dyes degrade faster than the analogous para-compounds, and that bleaching of the solution occurred within 40 minutes with a three-fold increase in rate when Fe(II) was added to the solution. Figure 1.2.32 provides a comparison of degradation products for the compounds studied[115]. The R group represents *p*-SO_3^-, σ-COO^-, and *p*-COO^-.

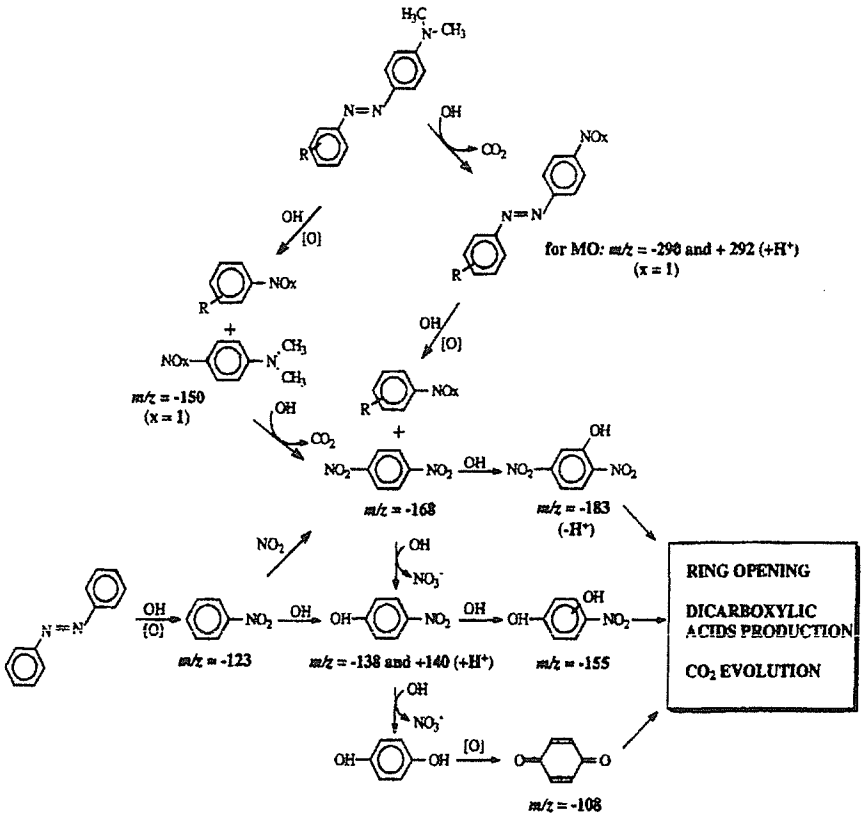

Figure 1.2.32: Sonochemical degradation pathways for the azobenzene dyes studied.

Another process employed is wet oxidation (WO), or promoted wet oxidation (PWO), in which high temperatures and pressures are used to initiate oxidative degradation. The oxidation process utilizes a titanium vessel with a flow of oxygen gas, and a temperature between 160-200°C, with pressures of 20-200 bar[106,108]. These conditions create reactive oxygen species, such as hydroxyl radicals, which can, in a similar manner to H_2O_2, degrade a dye. Figure 1.2.33 provides an illustration of a wet oxidation apparatus[106].

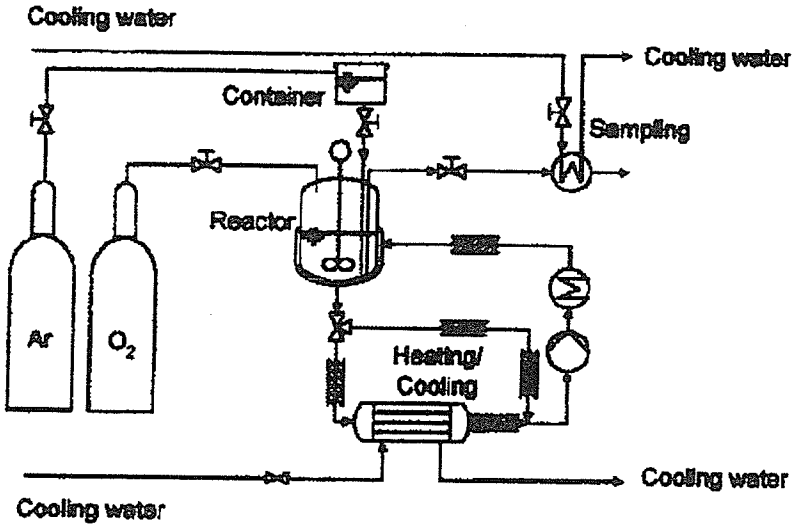

Figure 1.2.33: Wet oxidation apparatus

Lastly, but of no minor note, is the use of metal oxide catalysts for heterogeneous photocatalytic degradation[115-117]. Commonly, TiO_2 has been used to destroy aqueous dye compounds, although FeOOH, Fe_2O_3, ZnO and CuO have also been examined. The process commonly involves sensitization through charge injection into the TiO_2 particle[115]. The dye will become excited (dye*), and inject an electron into the oxide catalyst. This process forms a dye radical species which may degrade, or react with

active oxygen species (hydroxyl radical, superoxide anion radical) generated at the TiO_2 particle surface. The general reaction sequence is shown in Scheme 1.2.6, where CB denotes the conduction band of the metal oxide[115].

$$\text{dye} + h\nu \longrightarrow \text{dye}^*$$

$$\text{dye}^* + \text{MO} \longrightarrow \text{dye}^{+\bullet} + \text{MO}(e^-_{CB})$$

$$\text{MO}(e^-_{CB}) + O_2 \longrightarrow O_2^{-\bullet} + \text{MO}$$

$$\text{dye}^{+\bullet} \longrightarrow \text{Products}$$

$$\text{dye}^{+\bullet} + O_2^{-\bullet} \longrightarrow \text{Products}$$

Scheme 1.2.6: Photosensitization with irradiated TiO_2

iv) Thermolysis

Azo compounds are typically not thermally stability. In fact the facile bond breakage that occurs with respect to aliphatic azo compounds is the reason they have found use as radical initiators in polymer synthesis (*i.e.* AIBN, azobis-isobutyronitrile)[49]. Aromatic azo compounds, however, exhibit greater thermal stability owing to the delocalization of electron density. The aromatic system aids in increasing the strength of the C-N bond, thus raising the stability of the molecule. While the literature regarding the thermal degradation of aromatic azo systems is not extensive, there have been reports involving systems other than AIBN, including a limited overview of azo polymers[44,118]. Polymers containing the azo group in the main chain, such as the polyamides illustrated in Figure 1.2.34, display thermogravimetric analysis curves (TGA) which indicate the onset of decomposition at 300°C[44]. Another study examined a different series of azo main chain polymers (Figure 1.2.35)[44] and noted that the decomposition temperatures (approximately 360°C) did not change significantly with

alteration of the structure of the backbone, thus it was concluded that the weight-loss was due to the cleavage of the azo bond to form molecular nitrogen[44].

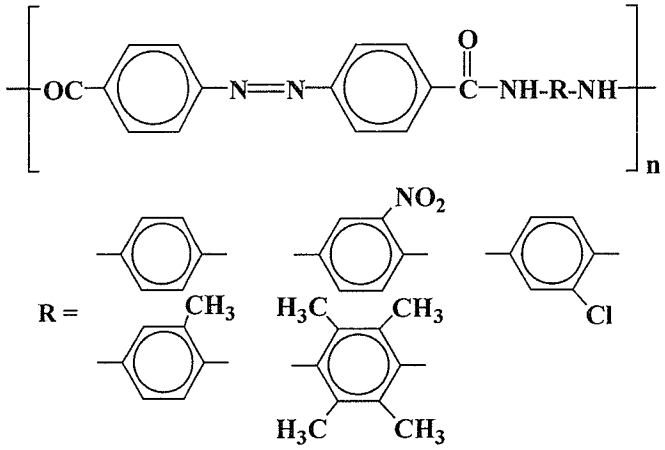

Figure 1.2.34: Azo-polyamide

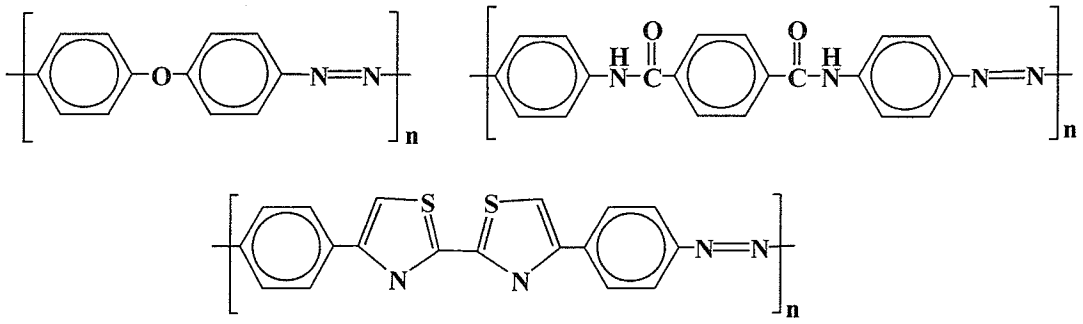

Figure 1.2.35: Azo functionalized polymers

1.3 Instrumental Analysis Techniques

1.3.1 Molecular Spectroscopy

i) Ultraviolet-Visible Absorption and Infrared Spectroscopy

Characterizing a substance via absorption of ultraviolet and visible electromagnetic radiation (emr) is one of the most time-tested analysis methods available. UV/Vis spectrophotometry operates under a simple concept; the sample absorbs light, thus altering the intensity of the beam. The difference in intensity is monitored relative to a reference beam and assigned an absorbance value based on the signal registered by the detector. The absorbance, A, and transmittance, T, of a substance in solution is directly related to its concentration, c ($mol \cdot L^{-1}$), as given in Equation 1.3.1[119]. In Equation 1.3.1, P_0 and P represent the intensity of the radiation prior to and after passing through the tube, ε represents the molar absorptivity (extinction coefficient, $L \cdot mol^{-1} \cdot cm^{-1}$) of the analyte, and b the pathlength of the sample vessel (cm).

Equation 1.3.1: $$\mathbf{A = -\log T = \log(P_0/P) = \varepsilon bc}$$

UV-Vis spectrophotometers incorporate a light source, commonly a deuterium arc lamp or tungsten filament, a splitter mechanism to pass light through both sample and reference (resulting in the terminology of a double beam instrument), and a photodetector such as a photomultiplier or diode array[119]. Figure 1.3.1 illustrates a common design for a double beam spectrophotometer[119-120]. The need for the reference cell arises from the scattering and reflection losses that occur when the light impinges on the sample cell (Figure 1.3.2)[119-120]. Thus a reference sample, made of the same solvent

composition as the analyte sample, accounts for the majority of solvent and sample cell related losses.

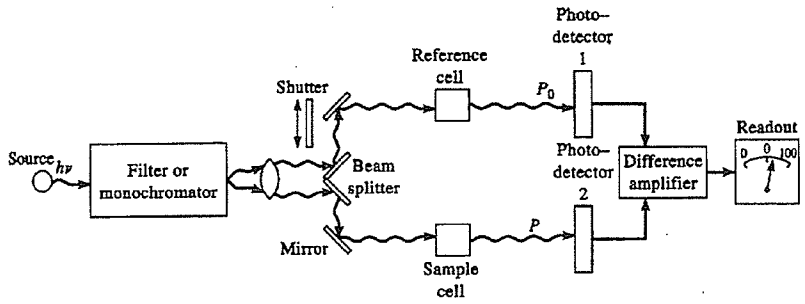

Figure 1.3.1: Schematic of a double beam UV/Vis spectrophotometer

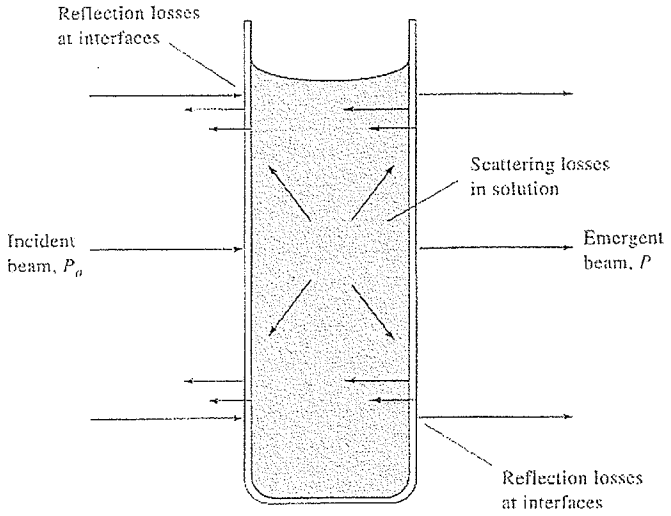

Figure 1.3.2: Reflective and scattering losses associated with UV/Vis spectrophotometry

In principle, infrared spectrophotometry operates very similarly to ultraviolet spectrometry, with the notable difference of the wavelength of absorbed radiation. The infrared region falls between the visible and microwave regions and can be split into

three sections: Near (14,300 cm^{-1}- 4000 cm^{-1}), Mid (4000 cm^{-1}- 600cm^{-1}) and Far (600 cm^{-1}- 200 cm^{-1}) IR[119,121-122].

When irradiated with IR light, a sample will absorb energy resulting in change to its molecular vibrations. In turn, these vibrational excitations are closely tied to various rotational changes. Similar to the situation of absorption of visible light (where each electronic state has many vibrational states associated with it), the association of the rotational states cause the absorbance bands in the IR region to be relatively broad[121].

There are two types of vibrations important in IR spectrometry, stretching and bending. A stretching vibration occurs along a bond axis, while a bending vibration alters bond angles, or the relative placement of a group of atoms in a molecule. Only vibrations that cause an overall change in charge distribution of a molecule will be registered through IR spectrometry. This results from the fact that the detector responds to changes in the electric field of the IR irradiation, which arises from the coupling of the induced electric field (from the molecule's changing dipole) with that of the incident IR radiation[121,123]. Figure 1.3.3 illustrates the common vibrations associated with IR spectrophotometry[121].

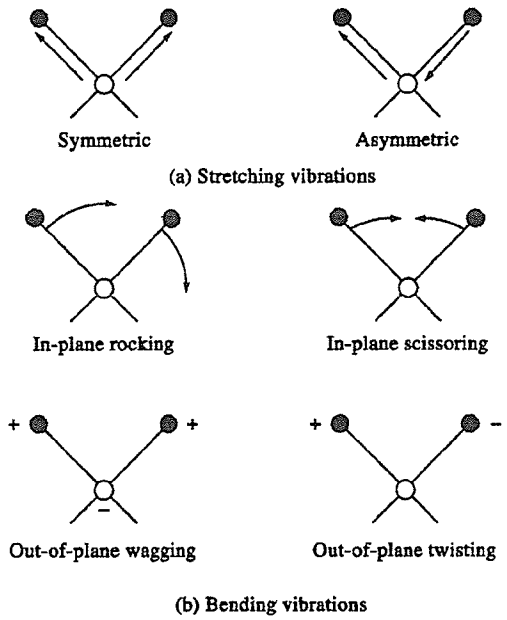

Figure 1.3.3: Molecular vibrations common to IR spectrophotometry (+ indicates movement toward reader, - denotes movement away from reader)

iii) Nuclear Magnetic Resonance Spectrometry

Nuclear magnetic resonance (NMR) spectrometry is one of the most widely used analysis techniques in chemistry. The technique makes use of the fact that under an applied magnetic field, nuclear energy states are split into discrete energy levels[119,121]. The number of levels created depends on the spin quantum number, I and is given by 2nI+1. Common nuclei of interest in NMR studies include ^{1}H, ^{13}C, ^{19}F, and ^{31}P. These nuclei all have a spin quantum number, I, of ½. Thus, upon application of an external magnetic field, they will be split into two levels, a +½ state and a –½ state. Figure 1.3.4 illustrates this phenomenon, where N represents the populations of the two states, α and β[119]. The lower level has a slightly higher population than the β level, with the energy difference between the two levels, ΔE (J), dependant on the magnetogyric ratio (γ, a

constant for a given nucleus, radians·T^{-1}·s^{-1}), Planck's constant (h, J·s), and the magnetic field strength (B_0, T), as shown in Equation 1.3.2[119].

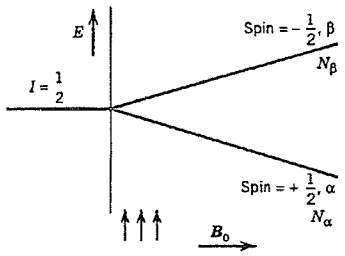

Figure 1.3.4: Splitting of levels under a magnetic field (magnetic field direction parallel to the ordinate)

Equation 1.3.2: $$\Delta E = (h\gamma/2\pi)B_0$$

Once the degeneracy is removed, application of a radiofrequency pulse will cause a net absorption of energy causing the population of the higher state to increase. The frequency of radiation (ν, Hz) required is related to ΔE, and thus directly related to the magnetic field strength, B_0, through Equation 1.3.3. If one envisions the nuclei as precessing around the z-axis (the direction of the applied magnetic field), then the application of a 90° radiofrequency (rf) pulse will direct the magnetic moments (μ) of the nuclei to lie within the xy plane. A receiver coil placed in this plane will detect the magnetization of the nuclei as it relaxes back to the z-axis[119,121]. Figure 1.3.5 illustrates the precession of the nuclei in an applied magnetic field along the z-axis[119].

Equation 1.3.3: $$\nu = (\gamma/2\pi)B_0$$

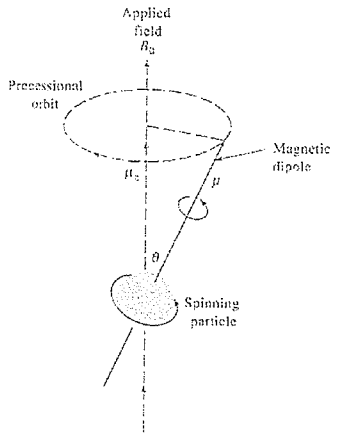

Figure 1.3.5: Precession of a nucleus under the influence of an external magnetic field

NMR spectra display peaks on a frequency ordinate. The frequency domain is produced via Fourier Transformation of a signal acquired in the time domain. The individual peaks, corresponding to individual nuclei on the molecule, will appear at different frequencies depending on the chemical environment they reside in. The chemical shift of a peak (δ), which is defined as the resonance position of the peak of interest relative to a reference compound (δ (ppm) = frequency of absorption in Hz/spectrometer frequency in MHz), is related to the effective field experienced by the nuclei. The effective field arises from the electron density present near the nuclei of interest. For example, the protons of CH_3Cl have less electron density associated with them than in CH_4, thus they are observed 'downfield' (3-4ppm), compared to CH_4 ($\approx$ 0.9 ppm), since they are effectively deshielded by the chlorine[119]. The simple concept of electron density is useful in a cursory explanation of chemical shift, however, in truth the situation is rarely that simple. One must examine effects of magnetic anisotropy to better understand and predict chemical shifts.

Electrons under the influence of a magnetic field will circulate, thus creating an induced magnetic field. For example, in aromatic systems the application of B_0 creates a ring current of electrons perpendicular to the applied field. This in turn creates an induced magnetic field in the same direction as the applied field at the aromatic protons. This lowers the external rf field necessary to bring the protons into resonance, thus they absorb (resonate) downfield at higher ppm values ($\approx$ 7ppm)[119,121]. Figure 1.3.6 illustrates this phenomenon[119].

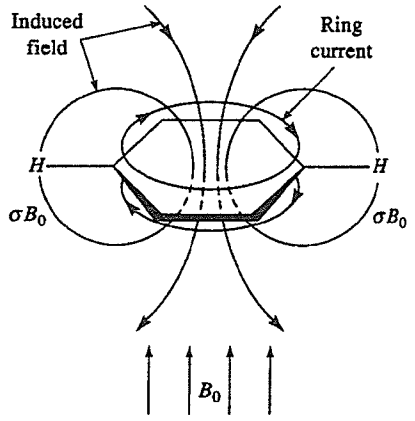

Figure 1.3.6: Deshielding of aromatic protons

In addition to the chemical shift being affected by neighbouring atoms, the appearance of the peak itself can change depending on the nearby nuclei in a process termed spin-spin splitting. With regards to ^{1}H NMR spectra, a proton signal will be split for each non-equivalent neighbouring proton in close proximity (typically 3-4 bonds removed). Coupling arises from the tendency for neighbouring spins to pair themselves with the spin of the nuclei of interest. As an example, the protons of ethane are all equivalent and thus would show as a single peak. However, in chloroethane

($ClCH_2CH_3$) the methylene group is not equivalent to the methyl group, and will be split into a quartet, while the methyl would appear as a triplet. The peak multiplicity is governed by [2(I)(n)+1], where n is the number of neighbouring protons and I is the spin quantum number of the neighbour. The value in Hz for the distance between the peaks is termed the coupling constant, J[119,121].

1.3.2 Thermal and Chromatographic Techniques

i) Thermogravimetric Analysis (TGA)

Thermogravimetric techniques monitor the mass of a substance as a function of applied temperature[119,122,124]. The instrument is illustrated in Figure 1.3.7[122]. A balance, holding the sample pan, is enclosed in a furnace that is heated during the course of the analysis. Changes in the mass of the analyte are recorded with temperature. The balance beam is commonly made of quartz or ceramic, as temperatures up to 1000°C are common. A flow of inert gas is typically introduced into the sample area to prevent oxidation of the sample during analysis. TGA techniques are commonly employed in polymer chemistry to determine the temperature resistance of a material, which is of paramount importance with regards to its application purposes.

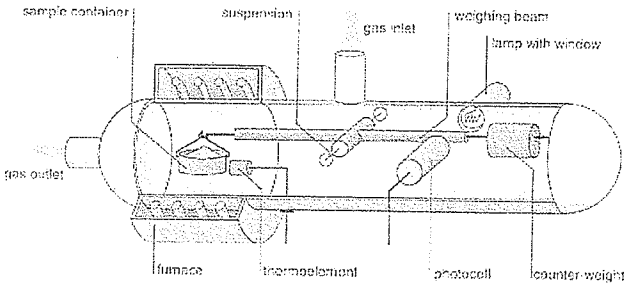

Figure 1.3.7: TGA apparatus

ii) Gel Permeation Chromatography (GPC)

Also known as size exclusion chromatography, GPC determines the average molecular weight of large molecules. Commonly used for polymer analysis, GPC works similarly to conventional chromatography techniques, however, there is one important difference. In GPC, no interaction of the analyte with the column's stationary phase occurs. Separation of species is accomplished via the ability, or lack thereof, of a sample to enter into the pores of the stationary phase (Figure 1.3.8)[122]. The smaller the analyte (i.e. the lower the molecular weight) the greater is its ability to enter the pores, thus requiring a longer time to pass through the column. Conversely, high molecular weight samples have less 'freedom of movement' and tend to elute first.

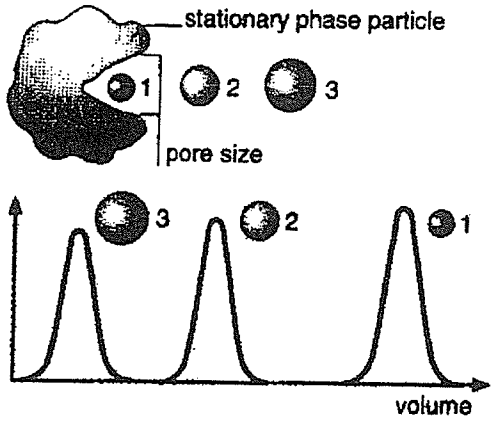

Figure 1.3.8: Relation between analyte particle size and elution order in GPC

Molecular weights are determined via a calibration graph commonly constructed from polystyrene standards. GPC provides two important molecular weight values: Mw and Mn. It is important to note that for a given polymer peak eluted, there may be polymeric chains of differing length within that peak. If N_x is the number of different chain lengths present, then the weight fraction of each chain is N_xM_x. Mw represents the

weight average molecular weight, and relates the mass of the chains ($N_xM_x^2$) to the weight fraction. Mn, however, relates the weight fraction to the total number of polymeric chains in the sample (Equation 1.3.4 A and B)[125]. The two values can be used together to determine the polydispersity index (PDI), which relates the range of molecular weights present in a given sample. The higher the PDI, the greater the range of molecular weights in the eluted peak.

Equation 1.3.4:

$$\mathbf{Mw} = \frac{\Sigma N_x M_x^2}{\Sigma N_x M_x} \quad \textbf{A} \qquad \mathbf{Mn} = \frac{\Sigma N_x M_x}{\Sigma N_x} \quad \textbf{B}$$

iii) Gas Chromatography-Mass Spectrometry (GC-MS)

Coupling mass spectrometry with a gas chromatograph allows simultaneous separation and mass spectral analysis of complex mixtures. The sample is effectively separated using a capillary column in conjunction with a suitable GC temperature program. Upon leaving the column the eluate is passed through an interface en route to the mass spectrometer. The analyte is then ionized, conventionally by an EI source, and passed through a mass analyzer (*i.e.* quadrapole, magnetic sector, time of flight) en route to the detector (commonly a channel electron multiplier)[119,122].

1.4 Chemical Actinometry

Determining the intensity of a light source is a key step in photochemistry experiments. It is required in order for the quantum yield (Φ, the amount of chemical conversion / amount of photons absorbed) of a photochemical reaction to be calculated, and is needed if an interlaboratory comparison is to be made. The most common means of calculating the intensity of a light source is via a chemical actinometer. An actinometer is a substance that has a known quantum yield, which is preferably near unity. Moreover, the compound should be versatile enough to accommodate a variety of photolytic conditions and wavelengths. Upon irradiation, the compound must cleave to yield readily detected products that do not absorb at wavelengths near those of the actinometer[126-128]. The actinometry experiments must be performed under low light conditions, and should necessarily use the same apparatus and glassware employed in the photolysis experiments for which the intensity of light is required.

Historically, a number of compounds have been examined as potential actinometers. $Mn(C_2O_4)_3^{-3}$, $Co(C_2O_4)_3^{-3}$, $Cr(C_2O_4)_3^{-3}$, $Ur(C_2O_4)_3^{-3}$, and $Fe(C_2O_4)_3^{-3}$ have all been examined, with different degrees of success[126,128-129]. Of the chemical actinometers available, by far the most common choice is the ferrioxalate actinometer, $Fe(C_2O_4)_3^{-3}$. The remaining compounds all suffer from low Φs that decrease with increasing wavelength, and typically require long reaction times. The uranyl oxalate actinometer commonly requires six hours for reaction, while the chromium salt displays even less photoactivity[128,129]. The cobalt analogue fairs little better as it displays low quantum yields and thermal instability[130]. Conversely, ferrioxalate has a Φ near unity, requires seconds to minutes for reaction, is relatively stable to heat, produces products

which do not absorb radiation yet are easily detected, and exhibits only slight variations in Φ between 254-500 nm, a range in which most conventional light sources fall[127]. It should be noted that if a quantum yield is to be determined for an analyte which photolyzes slowly, then an actinometer which reacts with an equal rate may be desired. However, in determining the intensity of a light source no direct comparison is being made to the quantum yield of the analyte and actinometer, thus a faster photolysis rate is typically desired.

Ferrioxalate undergoes photolytic cleavage according to the reactions given in Scheme 1.4.1[130]. The production of Fe(II) is spectrometrically followed at 510 nm via complexation with 1,10-phenanthroline[126-131]. The increase in Fe(II) mirrors the loss of ferrioxalate, and a first-order plot for appearance of Fe(II) provides a rate constant, k_p, which is used in conjunction with Equation 1.4.1 to calculate the intensity of light, $I_{\lambda 0}$ ($Ein \cdot L^{-1} \cdot min^{-1}$). Φ_p represents the quantum yield of the ferrioxalate (Table 1.4.1)[128], $\varepsilon_{p\lambda}$ is the molar absorptivity of the phenanthroline complex, 1.11 x 10^{-4} $L \cdot mol^{-1} \cdot cm^{-1}$, and l is the path length of the photolysis tube (cm)[131].

Scheme 1.4.1:

$$[Fe(C_2O_4)_3]^{-3} \xrightarrow{H_3O^+} [Fe(C_2O_4)]^{+} + 2(C_2O_4)^{-2}$$

$$[Fe(C_2O_4)]^{+} \xrightarrow{h\nu} Fe^{+2} + (C_2O_4)^{-}$$

$$(C_2O_4)^{-} + [Fe(C_2O_4)]^{+} \longrightarrow 2CO_2 + Fe^{+2} + (C_2O_4)^{-2}$$

Equation 1.4.1:

$$I_{\lambda 0} = -k_p/(2.303)(\Phi_p)(\varepsilon_{p\lambda})(l)$$

Table 1.4.1: Quantum Yields of ferrioxalate at different wavelengths of light[128]

Wavelength (nm)	Quantum Yield
254	1.25
302	1.24
405	1.14
436	1.11

The ferrioxalate process must be conducted in acidified solutions to prevent the precipitation of ferrous oxalate. However, despite this one criterion, the process shows remarkable versatility when compared to the other aforementioned actinometers. The reaction is relatively independent of temperature, with only slight changes observed per 10°C change. Furthermore, unlike with the other actinometers, there is no need to purge the system of oxygen, and any back reaction of ferrous ions with free oxalate (which would decrease the Φ) is negligible[128].

2.0 Experimental

2.1 Chemicals

Anhydrous aluminium chloride, aluminium powder, chlorobenzene, ferrocene, 4-chlorotoluene, 1,4-dichlorobenzene, 4-chloroxylene, ammonium hexafluorophosphate, sodium tetrafluoroborate, bisphenol-A, bisphenol-P, 4,4'-bis(4-hydroxyphenyl)valeric acid, 4-4'-biphenol, 4-4'-thiobisbenzenethiol, , piperizine, 1,8-octanedithiol, dimethylaminopyridine (DMAP), dicyclohexylcarbodiimide (DCC), resorcinol, 1-(4-aminophenyl)-ethanone, 4-aminobenzoic acid, 4-aminophenol, 2-(methyl-phenyl-amino)-ethanol, 2-(ethyl-phenyl-amino)-ethanol (all supplied by Aldrich), 4-nitroaniline (British Drug House), aniline (Fisher), 4-hydroxysulphone (Fluka), sodium acetate, sodium nitrite, 1,10-phenanthroline (all supplied by BDH), potassium carbonate, potassium ferrioxalate, anhydrous magnesium sulphate, sodium hydroxide (all supplied by Mallinckrodt), were used without purification. All solvents were reagent grade and used without purification.

2.2 Instrumentation

^{1}H and ^{13}C NMR spectra were recorded at 200 MHz and 50 MHz, respectively, on a Varian Gemini 200 NMR spectrometer. Chemical shifts were referenced to solvent residues and coupling constants were calculated in hertz. ^{13}C spectra were proton decoupled and recorded as an attached proton test (APT) with a delay time (τ) of 7 ms, which resulted in inverted CH and CH_3 carbon resonances (C and CH_2 resonances appeared as conventional peaks above the noise). Infrared spectra were recorded on a Bomem, Hartmann and Braun FT-IR spectrophotometer as KBr pellets. UV-Vis

spectra were obtained with quartz cuvettes of 10mm pathlength on a Shimadzu UV-250IPC recording spectrophotometer. Thermogravimetric analyses were obtained on a Mettler Toledo TGA/SDTA851^e under a steady stream of N_2 (50 ml/min) with a heating rate of 15°/min. GPC analyses were performed on a Waters 1525 GPC system equipped with Waters Styragel HR3 and HR4 7.8 x 300 mm columns at 40°C, a Waters 2410 refractive index detector and a 200μL sample loop. Molecular weights were calculated relative to polystyrene standards. Flow rates were 1.0 ml/min THF. Photolyses were performed in a Rayonette photochemical reactor equipped with sixteen 300 nm lamps or eight 254 nm lamps. Xe irradiations were performed in a photolysis vessel equipped with a PE 150 Xe power supply, reflective surfaces and a Xe arc 3718 lamp. Pyrolytic sublimation was performed in a Buchi GKR-51 pyrolytic sublimator connected to a vacuum pump. GC-MS analyses used a HP5890 GC coupled to a HP5970 MSD. The column was a 30 meter SPB-5 with a 0.25 mm inner diameter and a 0.25 μm film thickness. Temperature program was as follows: 100°C (3 min), 10°C/min to 285°C (40 min). Injection volume was 1 μl.

2.3 Actinometry

(i) Calibration graph for Fe(II)

A 5 mM solution of $FeSO_4 \cdot 7H_20$ was prepared in 0.05 M H_2SO_4. An aliquot of the solution was removed and combined with 1 ml of 0.1% 1,10-phenantroline, followed by 2 ml of 0.6 M sodium acetate buffer (pH = 4.4, adjusted with 1.0 M NaOH) and water to produce the desired concentration of Fe(II). Samples were mixed after each addition. Total volumes were 20 ml. Concentrations of Fe(II) were as follows: 2 μM, 5

μM, 10 μM, 25 μM, 50 μM, and 100 μM. The resulting solutions sat for at least 30 minutes, after which time their absorbencies at 510 nm were recorded. A calibration plot was constructed using ferrous ammonium sulphate as the source of Fe(II) ions at different concentrations.

(ii) Intensities of light

Photolyses were performed with 254 nm, 300 nm, and a Xe lamp in 50 ml Pyrex centrifuge tubes. The three types of light sources, 254 nm, 300 nm, and the Xe lamp, were specifically chosen to represent a range of spectral wavelengths, namely low wavelength (high energy) UV, near visible UV and simulated sunlight (representing all wavelengths), respectively. All solutions were prepared in the dark. An aliquot of a 60 mM stock solution of ferrioxalate in 0.05 M H_2SO_4 was taken and diluted to yield a 6 mM solution in 0.05 M H_2SO_4. 35 ml samples were removed from this solution and irradiated with a given wavelength of light for a set time. Following irradiation, the samples were immediately worked up.

Work up consisted of combining a 4 ml aliquot of the irradiated solution with 1 ml of the 1,10-phenanthroline solution, 2 ml of buffer and 13 ml of water. Solutions were stirred after each addition. Total volume was 20 ml, and the solutions were allowed to sit for at least 30 min prior to analysis. Thereafter, their absorbance at 510 nm was recorded.

In addition to the irradiated samples, a blank sample consisting of H_2SO_4, 1,10-phenanthroline, and buffer, in the same concentrations as the actual samples, was made. This sample was used as the blank for the spectrophotometer. A background sample used to correct for the presence of ambient light during the experiments was also made.

This consisted of a solution that was worked up in the same manner as the irradiated samples, with the exception that the solution was not irradiated.

2.4 Synthesis Procedures

(i) Synthesis of cyclopentadienyliron complexes

η^6-chlorobenzene-η^5-cyclopentadienyliron hexafluorophosphate, η^6-1,4-dichlorobenzene- η^5-cyclopentadienyliron hexafluorophosphate, and η^6-1,4-dichlorobenzene- η^5-cyclopentadienyliron tetrafluoroborate complexes (**1a-c)** were prepared as previously described[132,133].

Synthesis of compounds **3a-h, 4a-b**: The η^6-arene- η^5-cyclopentadienyliron salt complexes (2 mmol) were combined with a dinucleophile (1 mmol), and K_2CO_3 (2.5 mmol), in a 50 ml round bottom flask. The starting materials were dissolved in 10 ml of DMF and stirred under N_2 overnight. The solution was then poured into a 10% (v/v) HCl solution to which 4 mmol of ammonium hexafluorophosphate or sodium tetrafluoroborate was added. The precipitated product was collected via suction filtration and rinsed with copious amounts of water. Upon drying, the yellow granular solid was rinsed with diethyl ether.

Complex **4a-b** was prepared in a similar manner, by mixing 1 mmol of compound **3b** or **3c** with 0.5 mmol of **2b** in a 50 ml round bottom flask. Thereafter the procedure mirrored that outlined above.

(ii) Synthesis of azo dye starting materials

Synthesis of dyes **9a-f**: The aniline or aniline derivatives (0.02 mol) were dissolved in a mixture of 50 ml of concentrated HCl:water (1:1 v/v) and heated if necessary to dissolve the aniline. The solution was stirred and cooled to 0-5°C and maintained at this temperature while a sodium nitrite solution (0.022 mol in 40 ml water) was added dropwise. The presence of excess nitrous acid in the amine solution was tested using a starch-iodide paper. The diazonium solution was further stirred for 30 min at which time the excess nitrous acid destroyed by addition of 0.5-1.0 g of urea to the solution. To this, a solution of the appropriate coupling component was added (0.02 mol dissolved in 20 ml of acetic acid and cooled to 0-5°C by the addition of crushed ice). The reaction was stirred for 2 hours at which point the pH of the solution is adjusted to pH 4-5 by adding 10% sodium acetate, causing precipitation of the crude dye. The dye was collected, washed with water and recrystallized from ethanol.

Synthesis of dye **9g** required a slight alteration to the aforementioned procedure. Resorcinol (coupling component) was dissolved in sodium hydroxide and cooled to 0-5°C with ice. To this, the diazonium solution was added slowly within 30 minutes. The reaction was stirred for two hours. Neutralization of the reaction mixture at the end of the synthesis requires acetic acid to bring the pH to 6.

iii) Reaction of azo dyes with cyclopentadienyliron complexes

Starting complexes **10**, **12**, **14**, **16a-d**, were prepared as previously reported[18,132,133].

Synthesis of complexed dyes **11a-b**, **15**, **17a-d**: An appropriate mmol ratio of complex to dye (1:1, 1:2, and 2:1, for **11a-b**, **15**, and **17a-d**, respectively) was mixed in a

50 ml round bottom flask with an excess of K_2CO_3, and stirred in DMF under N_2 overnight. The coloured solution was then precipitated into 10% HCl, to which a molar excess of ammonium hexafluorophosphate was added. The solid product was collected via suction filtration, washed with water, ether and dried.

Synthesis of complexed dyes **13a-c**: Complex **12** (1 mmol), azo dyes **9a-c** (1.2 mmol) and DMAP (1.2 mmol) were combined in 3 ml of DMSO and 10 ml of CH_2Cl_2. The solution was stirred under N_2 for five minutes and then DCC (1.2 mmol) was added, and the reaction proceeded at room temperature for 16 h. The complex was added to a 10% HCl solution containing NH_4PF_6 (2 mmol), extracted with CH_2Cl_2, washed with water and dried over $MgSO_4$. The solution was dried, dissolved in acetone and filtered into ether resulting in an orange or red precipitate, which was collected in a crucible and dried.

UV-Vis Spectroscopy: UV spectra of the dyes were recorded in DMF, ethanol and a 10% HCl (5 M) solution in ethanol. The complexed dye compounds typically displayed poor solubility in ethanol, thus it was necessary to solubilize the dye with µl amounts of acetonitrile prior to addition of ethanol. Test spectra acquired using dyes soluble in ethanol illustrated that the use of a 0.1% solution of acetonitrile in ethanol did not change the observed wavelength maxima of the dyes. All samples were run against blank solutions of appropriate compositions.

iv) Polymerization of complexed dyes

Preparation of polymers **19a-i**: The complex **13a-c** (0.25 mmol), dinucleophile **18a-c** (0.25 mmol) and K_2CO_3 (1 mmol) were dissolved in 2 ml of DMF and stirred

under N_2 at 60°C overnight. The solution was poured into 10% HCl to which NH_4PF_6 (0.5 mmol) was added. The coloured polymer was collected in a crucible, washed with water and ether and then dried.

2.5 Photolytic demetallation

i) Decomplexation of **3a-h, 4a-b**: The complex (0.1 mmol) was dissolved in a 4:1 mixture of CH_2Cl_2:CH_3CN (total volume 35 ml) in a 50 ml Pyrex centrifuge tube. The tube was capped with a septum, purged with N_2 for 10 minutes, and photolyzed. Samples were photolyzed with 300 nm light for various times, ranging from 15 minutes to 8 hours, to determine the time required for successful demetallation. For complex **4a** the procedure was repeated with the other light sources (254 nm, Xe lamp). Regardless of the light source employed, once irradiated, the solution was then rotoevaporated to dryness, and the residue redissolved in chloroform. Samples were washed with water (3 x 20 ml), dried with magnesium sulphate, filtered and concentrated to approximately 1-2 ml. Samples were precipitated in cold hexane and stored at 0°C overnight. Thereafter, the product was collected via suction filtration and dried prior to analysis.

Due to the higher solubility of compounds **6a-c,f-g** in hexane, the dried chloroform solution was concentrated to dryness and placed under vacuum overnight. The oil residue was rinsed with hexane and further dried under vacuum.

Solvent related trials were photolyzed as described above with the following exception. For the CH_2Cl_2 trial, distilled dichloromethane was used, and samples were weighed out in a glove box under a N_2 atmosphere. The sealed tubes were removed from the glove box and immediately photolyzed with 300 nm light.

ii) Photolytic decomplexation of complexed dyes **11a-b, 13a-c, 15, 17a-d**:

The complexed dyes (0.1 mmol) were dissolved in a 4:1 (compounds **11a-b**, **15**, **17a-d**) or 1:1 (**13a-c**, due to limited solubility in CH_2Cl_2) ratio of CH_2Cl_2:CH_3CN. Total volumes were 35 ml. Photolysis was carried out for 3.5 hours with 300 nm lamps. Following photolysis, sample solutions were concentrated to dryness, and dissolved in ether. The starting complexes were not readily soluble in ether, thus any remaining complexed sample was selectively removed. The ether was washed repeatedly with water, and thereafter dried with anhydrous magnesium sulphate, filtered, and concentrated to dryness. If starting material remained, the residue was dissolved in ether and eluted through a silica gel column. The coloured elute was rotary-evaporated to dryness and the residue stored under vacuum for several hours prior to analysis.

Decomplexation of polymers **19a-i**: The complexed azo dyes were photolytically demetallated to yield compounds **24a-i**. The complexed polymers (0.01 mmol) were dissolved in a 1:1 ratio of CH_2Cl_2:CH_3CN. Polymers **19c,f,h,i** required the addition of 5 ml of DMSO and a 10 minute sonication period to aid solubility. Total volumes were 40 ml. Photolysis was carried out at 300 nm for 4 hours in Pyrex centrifuge tubes. The irradiated solutions were rotoevaporated to dryness (the solutions containing DMSO were washed with water prior to evaporation to remove the DMSO) and chloroform was added to solubilize the polymer. The chloroform solution was then washed with water, dried with anhydrous magnesium sulphate, filtered, concentrated using a rotary evaporator, and added to cold ether. The residue was stored under vacuum for several hours prior to analysis.

2.6 Photocatalytic/Thermal degradation

(i) H_2O_2 catalyzed oxidation

H_2O_2 catalyzed degradation of **9d, 11b, 24d**: The dye (1 mg) was dissolved in 5mL of CH_3CN to which 30 ml of doubly distilled water was added. Absorbance readings were recorded at the time of preparation (t=0) and at specific timed intervals during their photolysis with 300nm light. Aliquots were transferred to a clean and dry cuvette, and returned to the parent solution after recording the visible absorbance. Comparison samples were prepared by irradiating dye and solvent without H_2O_2 present.

H_2O_2 catalyzed degradation of **9g, 17d**: The initial study involving **9g** illustrated a slow rate of degradation using the procedure outlined above. Thus a slightly modified procedure was followed which incorporated the addition of 2 drops of concentrated ammonia solution. The solution, without H_2O_2, was made and allowed to sit for 30 minutes to allow for the appearance of the 323 nm λ_{max} peak. After 30 minutes, 1 ml of H_2O_2 was added and an aliquot immediately transferred to a 10 mm pathlength quartz cuvette. Only the absorbance at λ_{max} (323 nm) was measured over time by utilizing a continued exposure time course experiment. This experiment monitored the absorbance at the set wavelength over time, and did not scan through the UV-Vis spectrum. A solution without H_2O_2, and completely sealed to light, was prepared for comparison. At specific time intervals an aliquot of solution was removed and used to record a UV-Vis spectrum. Compound **17d** utilized the same procedure as for **9g**, however, 250 μL of H_2O_2 was added and the absorbance at 445 nm was followed via a time course experiment.

(ii) Thermal degradation

The dye (20 mg) was sealed in a 20 ml glass vial equipped with a septa lined cap. Samples were purged under a steady flow of N_2 gas throughout the experiment. Samples were heated in a sand bath at approximately 300°C for 15 minutes. Upon cooling, the samples were rinsed with acetone and chloroform in an attempt to isolate products.

3.0 Results and Discussion

3.1 Actinometry

Ferrioxalate actinometry was used to calculate the intensity of the three light sources (300 nm, 254 nm, and simulated sunlight (Xe lamp). Photolyses were carried out for varying amounts of time, depending on the wavelength of light used. The experiments utilizing 300 nm light required 20-30 seconds for the determination of the rate of formation of Fe(II). Alternatively, irradiation with 254 nm and simulated sunlight required up to 3-5 minutes of exposure. The absorbance values of the solutions were compared to a calibration graph, which was prepared from the absorbencies of known concentrations of Fe(II), to determine Fe(II) concentration. This allowed a first-order rate graph to be constructed for the appearance of the Fe(II) species. As an example, the rate of appearance of Fe(II) for the Xe experiment is illustrated in Figure 3.1.1.

The linear regression of the data provided a slope (kp) that was used in conjunction with Equation 1.4.1 to calculate the intensity of light. The slope from the formation of the Fe(II) species is opposite that of the decomposition of ferrioxalate, thus the value of –kp is used in Equation 1.4.1. The inner diameter of the photolysis tube (l in Equation 1.4.1) was determined to be 2.476 cm with vernier callipers. Table 3.1.1 provides the rate of formation of the Fe(II) species, the correlation coefficient (R), and the intensity of light for the three light sources. It is interesting to note that while the 254 nm light is more energetic than the other wavelengths, it displayed the lowest intensity. This can be partly attributed to the lower number of lamps (8) used when

compared to the 300 nm photoreactor (16), and the increased absorbance of wavelengths below 280 nm by the photolysis tube itself[127].

Equation 1.4.1: $$I_{\lambda 0} = -k_p/(2.303)(\Phi_p)(\varepsilon_{p\lambda})(l)$$

Table 3.1.1: Intensities of the light sources

λ	k_p (s^{-1})	R value	Intensity (Ein $L^{-1}min^{-1}$)
300	0.00791	0.9824	6.0×10^{-5}
254	0.00691	0.9788	5.2×10^{-6}
Xe	0.03504	0.9831	3.0×10^{-5}

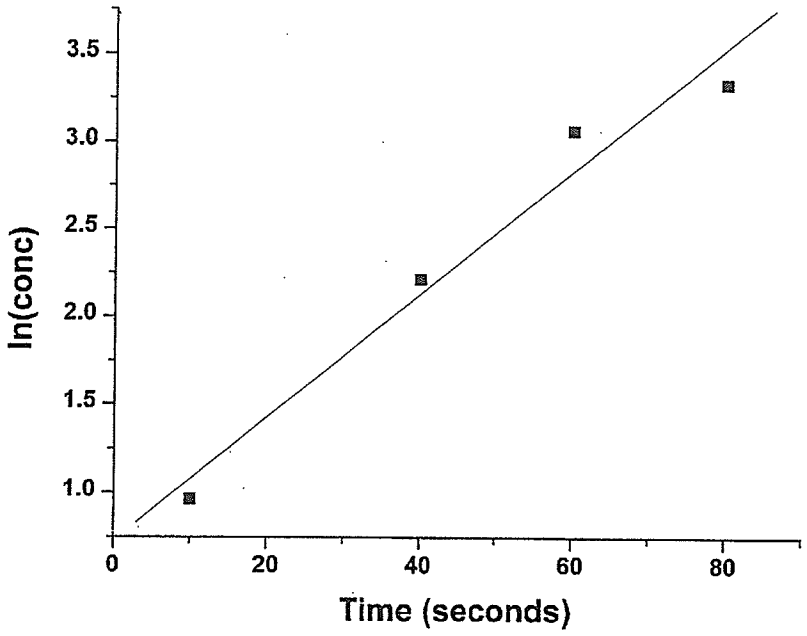

Figure 3.1.1: Rate of formation of Fe(II) with simulated sunlight

3.2 Decomplexation Study

3.2.1 Synthesis of organoiron complexes

Utilizing the excellent electron withdrawing power of the $CpFe^+$ moiety, a series of bimetallic complexes were synthesized as shown in Scheme 3.2.1. These compounds were isolated in good yield and characterized by NMR, IR, and TGA techniques. Reaction of **3b-c** with dinucleophile **2b** in a 2:1 molar ratio allowed for the isolation of a tetrametallic compound, **4a-b** (Scheme 3.2.2).

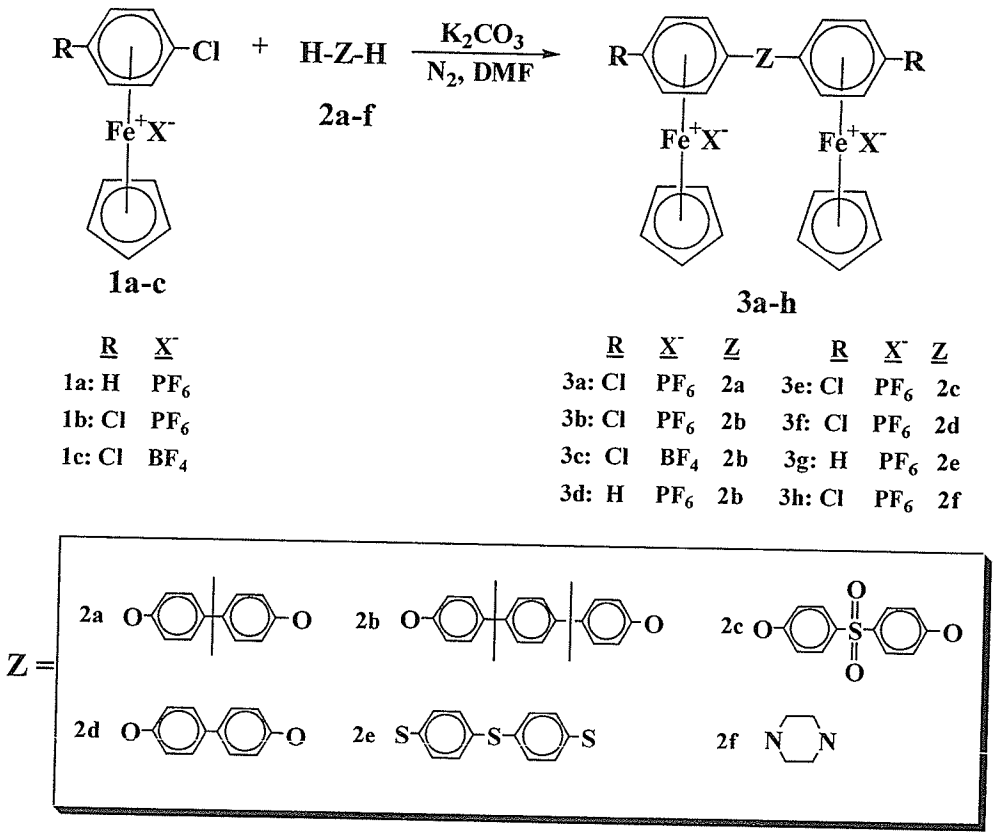

Scheme 3.2.1

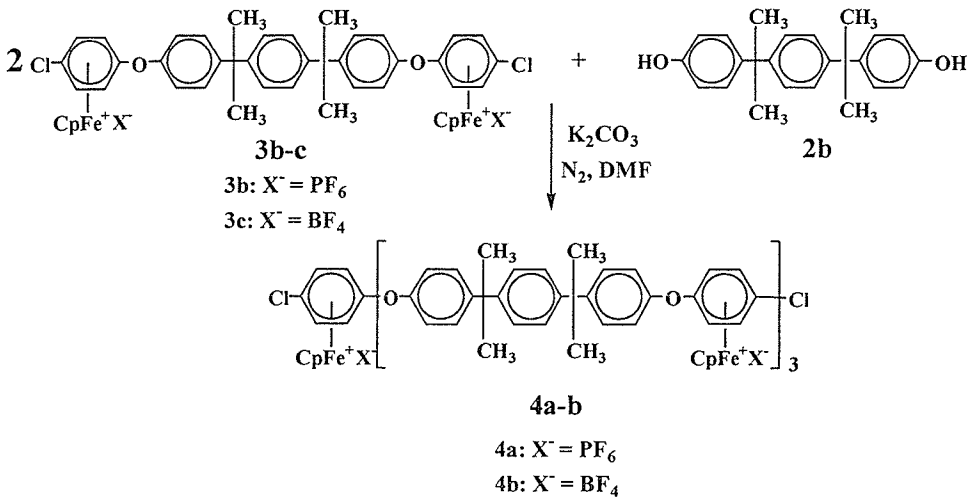

Scheme 3.2.2

The ^{1}H and ^{13}C NMR spectra of the complexes displayed the characteristic resonances associated with cyclopentadienyliron complexes (Table 3.2.1, 3.2.2). Figures 3.2.1 and 3.2.2 present the ^{1}H NMR spectra of complexes **3b** and **3f** for comparison. The intense singlet located at 5.37 ppm (**3b**) and 5.42 ppm (**3f**) represents the equivalent protons on the Cp ring. The eight complexed aromatic protons appear as two doublets resonating between 6.5 and 7.0 ppm. The complexed aromatic protons alpha to the ether bond appear at 6.48 ppm and 6.61 ppm for compounds **3b** and **3f**, respectively. The remaining aromatic protons resonate at values customary for aromatic protons. Complex **3b** displays an intense singlet in this region that is attributed to the aromatic protons isolated on either side by the isopropylidene groups. The remaining singlet at 1.71 ppm in the spectrum of **3b** represents the equivalent methyl protons of the isopropylidene groups. The multiplet at 2.04 ppm is the protons of the referenced acetone solvent.

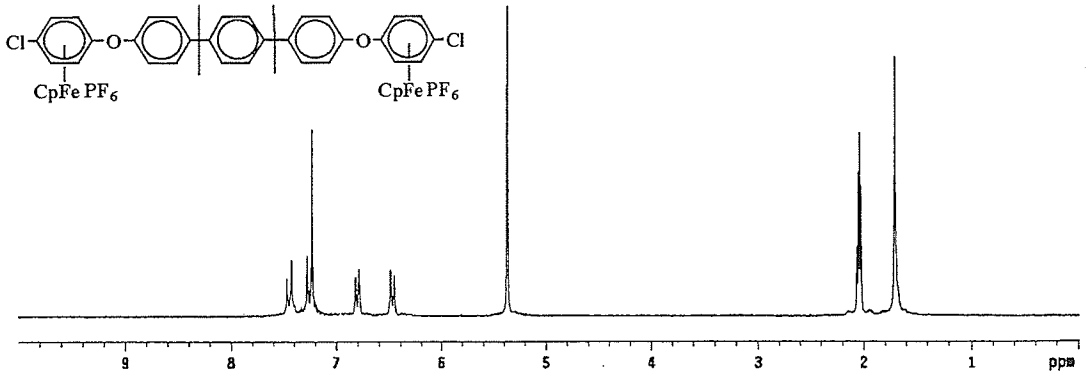

Figure 3.2.1: ^{1}H NMR spectrum of bimetallic complex **3b**

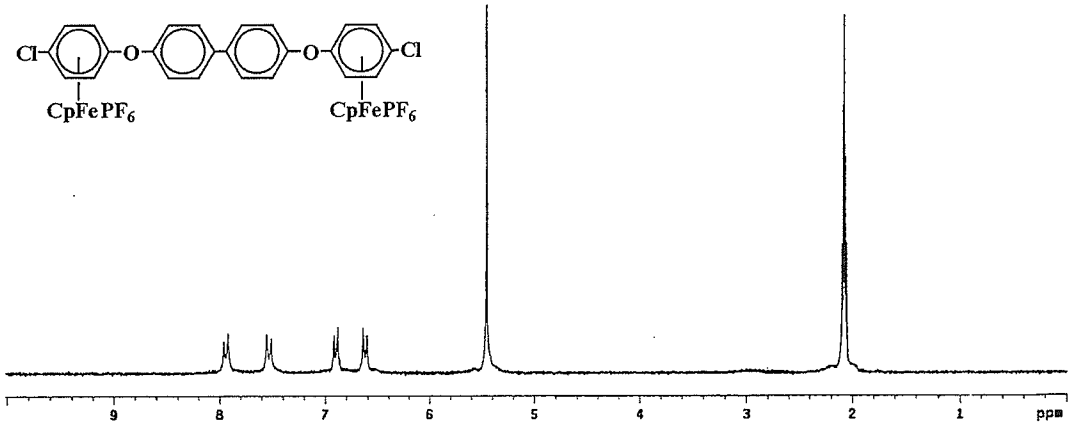

Figure 3.2.2: ^{1}H NMR spectrum of bimetallic complex **3f**

Formation of complex **4a-b** altered the NMR spectra when compared to the bimetallic starting material. Figure 3.2.3 and 3.2.4 illustrate the ^{1}H and ^{13}C NMR spectra for compound **4a**. The most striking difference in the ^{1}H spectrum is the appearance of a second Cp resonance (at 5.28 ppm), which is attributed to the Cp ring pendant to an arene containing two etheric bonds. Additionally, a new singlet at 6.31 ppm appears, which represents the complexed aromatic protons of this same arene ring. The uncomplexed aromatic protons continue to resonate at relatively the same

frequency, however the region is necessarily more complicated due to the larger number of protons associated with the structure. Lastly, the methyl protons still appear as a singlet, albeit a slightly broader one, at 1.65 ppm.

The ^{13}C NMR spectra illustrate similar characteristics with two resonances appearing for the carbons of the Cp ring (78.99 ppm and 80.44 ppm). The peaks at 104.18 ppm and 131.59 ppm are attributed to the quaternary carbons on the complexed aromatic rings. The 104.18 ppm resonance results from the quaternary carbon attached to the chlorine substituent, while the other represents those with an ether bond. The three non-equivalent CH carbons of the complexed rings (75.95, 77.17, 87.87 ppm) appear near the Cp peaks, and represent the arene rings bordered by two ether linkages (75.97 ppm) and the complexed arenes at the ends of the molecule (77.17, 87.87 ppm). The peaks at 31.14 ppm and 42.93 ppm represent the methyl carbons and the quaternary carbon of the isopropylidene group, respectively. The multiplet at 29 ppm is the methyl carbons of the referenced acetone solvent.

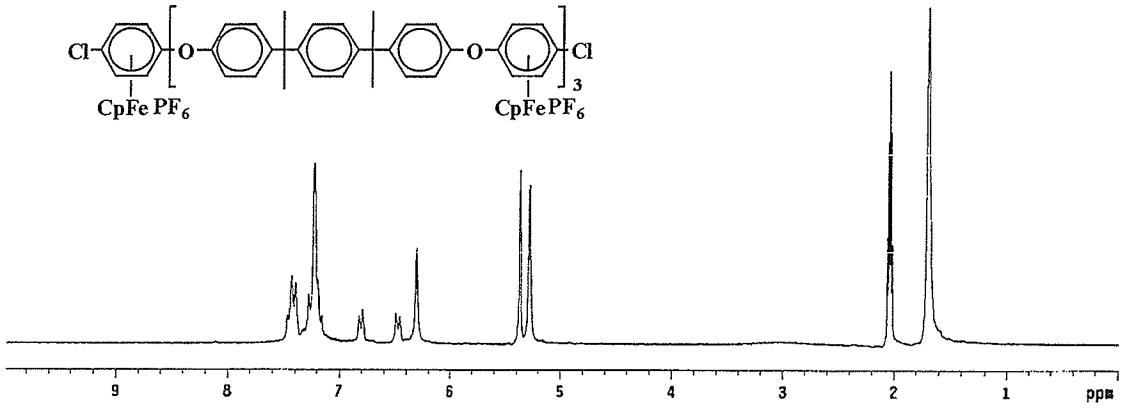

Figure 3.2.3: ^{1}H NMR spectrum of tetrametallic complex **4a**

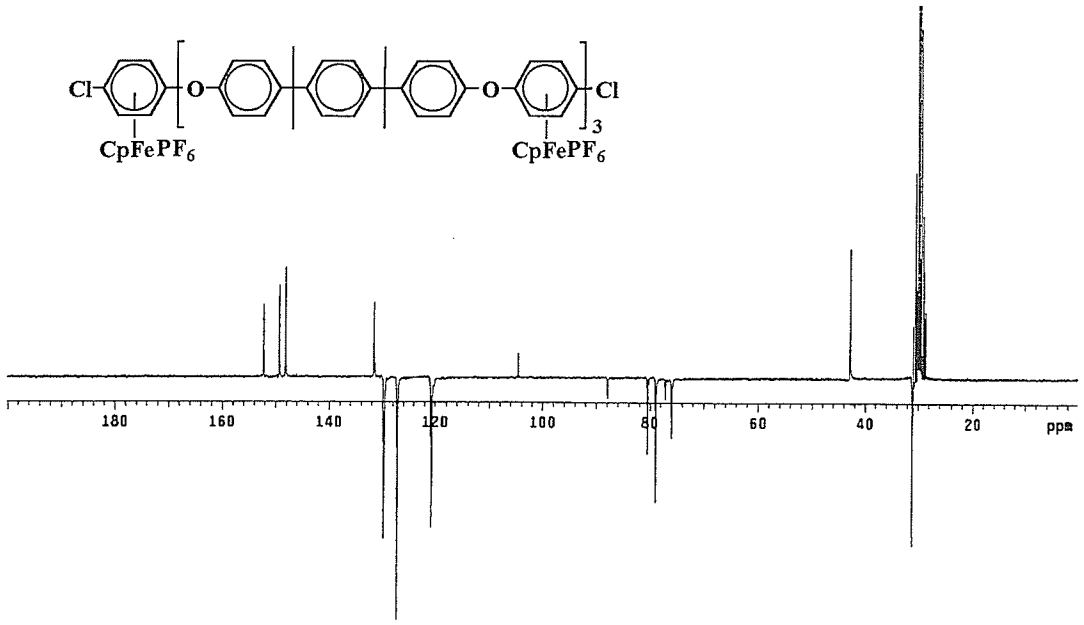

Figure 3.2.4: ^{13}C NMR spectrum of tetrametallic complex **4a**

IR spectra of the complexes displayed absorbances attributed to the $CpFePF_6$ or $CpFeBF_4$ moiety. While no noticeable change is associated with the NMR spectra of the analogues, the IR spectra do show a significant difference (Table 3.2.3). The PF_6 analogue causes a large peak in the 840-845 cm^{-1} region (arising from P-F bond vibrational changes), while the BF_4 complexes produce a broad band centred in the 1080-1085 cm^{-1} region (arising from B-F bond vibrational changes). Figure 3.2.5 and 3.2.6 provide the IR spectra of compounds **4a** and **4b** for comparison.

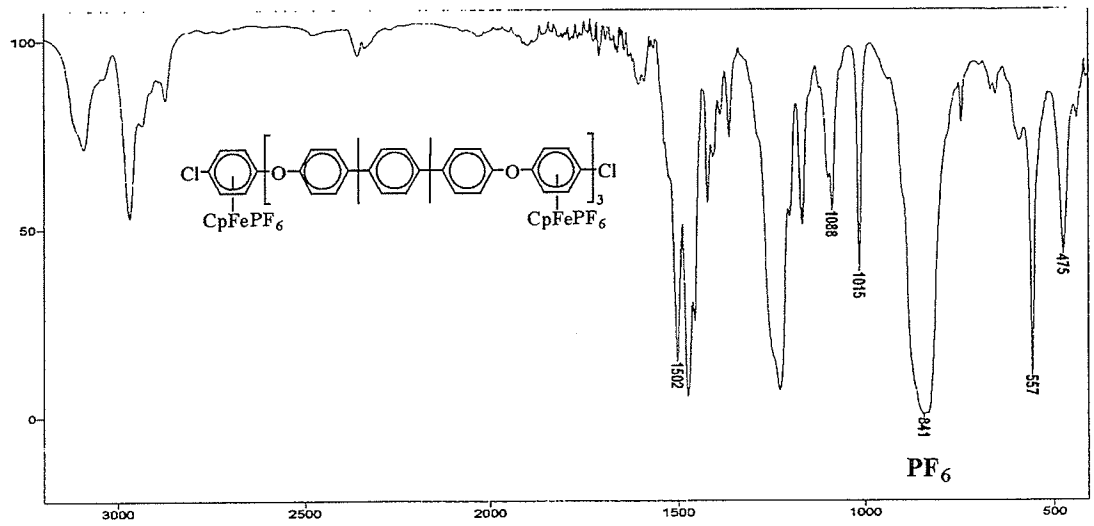

Figure 3.2.5: IR spectrum of **4a**

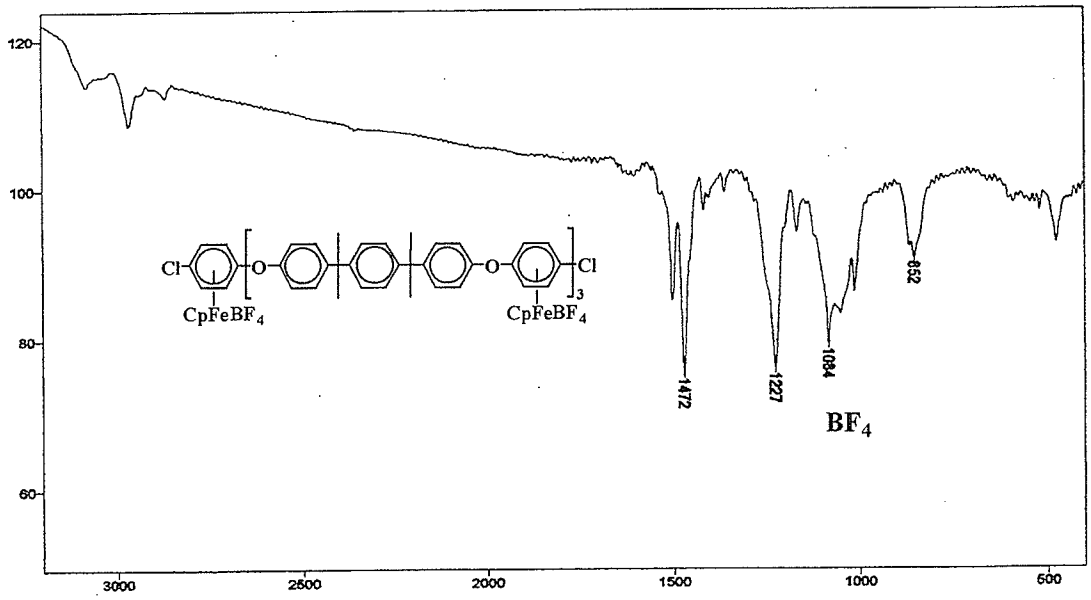

Figure 3.2.6: IR spectrum of **4b**

Thermogravimetric analysis of complexes **3a-h** and **4a-b** illustrated two distinct weight losses. The first loss, occurring between 220-250°C represented the liberation of the $CpFe^{+}$ moiety. The remaining weight loss is attributable to the destruction of the organic backbone. The confirmation of these weight losses is evident when the TGA

curve is compared to those of other molecules, such as the starting complexes (**1a-c**), their organic analogues, and macromolecular samples containing similar aryl-ether linkages. These compounds display weight losses at similar temperatures, with the temperature of the second weight loss typically increasing as the molecular weight of the aryl ether molecule increases[14-17]. Figure 3.2.7 provides the TGA curve for compound **4b**, which illustrates the two weight losses. Table 3.2.3 provides the numerical data for complexes **3a-h**, and **4a-b**.

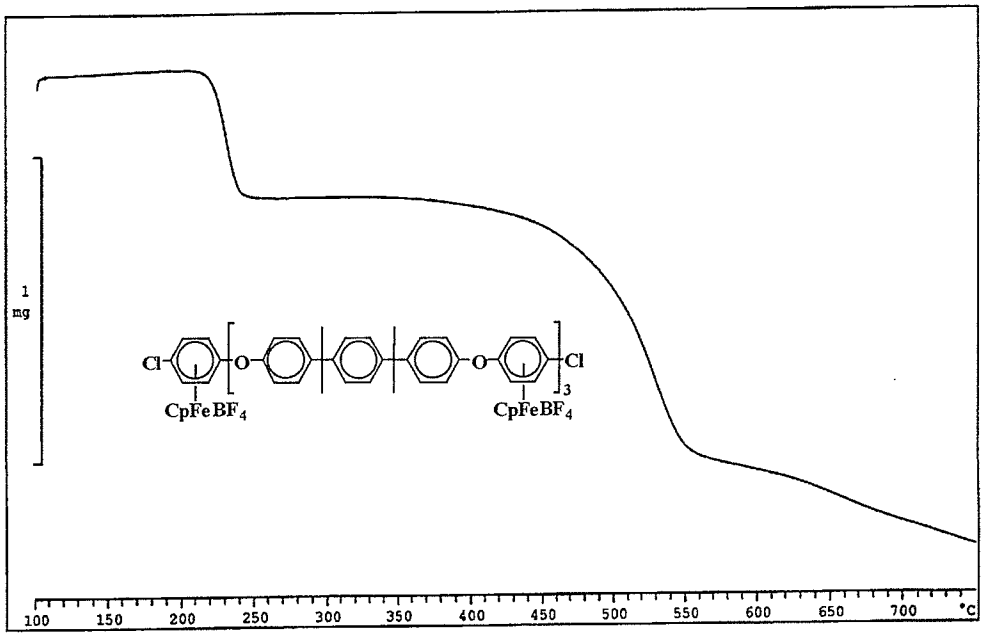

Figure 3.2.7: TGA curve for complex **4b**

Table 3.2.1: ^{1}H NMR data for complexes **3a-g, 4a-b**

δ (ppm) in acetone-d_6				
	Aromatic H	**Complexed ArH**	**Cp**	**CH_2, CH_3**
3a	7.29 (d, 4H, J=8.9) 7.49 (d, 4H, J=6.6)	6.48 (d, 4H, J=7.0) 6.81 (d, 4H, J=7.0)	5.37 (s, 10H)	1.77 (s, 6H) CH_3
3b	7.23-7.28 (m, 8H) 7.45 (d, 4H, J=8.6)	6.48 (d, 4H, J=7.0) 6.81 (d, 4H, J=6.6)	5.37 (s, 10H)	1.71 (s, 12H) CH_3
3c	7.22-7.28 (m, 8H) 7.45 (d, 4H, J=8.5)	6.48 (d, 4H, J=6.9) 6.79 (d, 4H, J=6.8)	5.35 (s, 10H)	1.72 (s, 12H) CH_3
3d	7.17-7.28 (m, 8H) 7.45 (d, 4H, J=8.6)	6.27-6.37 (m, 6H) 6.44-6.50 (m, 4H)	5.25 (s, 10H)	1.71 (s, 12H) CH_3
3e	7.52 (d, 4H, J=8.9) 8.14 (d, 4H, J=8.8)	6.62 (d, 4H, J=6.9) 6.86 (d, 4H, J=6.9)	5.29 (s, 10H)	-------
3f	7.51 (d, 4H, J=8.5) 7.91 (d, 4H, J=8.2)	6.61 (d, 4H, J=6.6) 6.87 (d, 4H, J=6.3)	5.42 (s, 10H)	-------
3g	7.59 (d, 4H, J=8.9) 7.76 (d, 4H, J=9.0)	6.39-6.58 (m, 10H)	5.23 (s, 10H)	-------
3h	-------	6.20 (d, 4H, J=7.0) 6.62 (d, 4H, J=7.4)	5.20 (s, 10H)	3.83 (s, 8H) CH_2
4a	7.19-7.27 (m, 24H) 7.41 (d, 12H, J=7.0)	6.31 (s, 8H) 6.48 (d, 4H, J=7.0) 6.81 (d, 4H, J=7.0)	5.28 (s, 10H) 5.36 (s, 10H)	1.69 (s, 36H) CH_3
4b	7.17-7.26 (m, 24H) 7.40 (d, 12H, J=7.1)	6.29 (s, 8H) 6.46 (d, 4H, J=7.0) 6.80 (d, 4H, J=7.2)	5.28 (s, 10H) 5.39 (s, 10H)	1.65 (s, 36H) CH_3

Coupling constants calculated in Hz

Table 3.2.2: ^{13}C NMR data for complexes **3a-g, 4a-b**

δ (ppm) in acetone-d_6							
	quat ArC	**ArCH**	**Comp. quat**	**Comp. ArCH**	**Cp**	**CH_2/CH_3**	**Other**
3a	149.64 151.74	121.10 130.01	104.72 133.64	76.94 87.74	80.36	31.11 CH_3	42.10*
3b	148.14 149.96 151.60	120.81 127.12 129.84	104.68 133.81	76.97 87.97	80.32	31.06 CH_3	42.92*
3c	148.24 149.99 151.53	120.79 127.06 129.89	104.44 133.78	76.97 87.96	80.30	31.10 CH_3	42.90*
3d	148.37 149.90 151.93	121.07 127.28 129.91	134.58	77.74 85.74 87.84	78.06	31.13 CH_3	43.03*
3e	129.60 157.61	120.24 120.55	104.04 137.59	78.07 86.68	79.43	-------	-------
3f	138.85 153.75	122.07 130.11	104.97 133.58	77.45 87.88	80.52	-------	-------
3g	128.46 138.20	133.61 137.17	109.59	87.69 87.85 89.58	79.45	-------	-------
3h	-------	-------	102.76 125.86	68.44 86.91	78.42	46.21 CH_2	-------
4a	148.16 149.31 152.27	120.65 127.12 129.69	104.18 131.59	75.95 77.14 87.87	78.99 80.44	31.14 CH_3	42.93*
4b	148.10 149.35 152.23	120.63 127.09 129.89	104.15 131.68	75.90 77.09 87.93	78.97 80.40	31.19 CH_3	42.86*

*denotes quaternary carbon

Table 3.2.3: Yield, IR, and TGA data for complexes **3a-h**, **4a-b**

	%Yield	IR (cm^{-1})	TGA_{onset}	TGA_{endset}	$TGA_{midpoint}$	% Weight loss
3a	88	841 (PF_6^-)	242 312	271 349	259 325	36 26
3b	95	842 (PF_6^-)	251 340	278 399	265 367	29 39
3c	90	1084 (BF_4^-)	245 338	274 392	260 365	30 35
3d	85	841 (PF_6^-)	220 371	253 415	237 393	28 30
3e	85	841 (PF_6^-)	229 325	242 388	236 359	26 23
3f	90	822 (PF_6^-)	238 315	263 365	252 332	34 28
3g	80	842 (PF_6^-)	226 317	250 374	239 345	25 31
3h	80	842 (PF_6^-)	245 430	253 483	250 453	26 41
4a	95	842 (PF_6^-)	241 524	282 591	262 548	20 55
4b	90	1084 (BF_4^-)	222 496	239 549	231 520	39 68

3.2.2 Selection of wavelength of light

Complex **4a** was chosen as a test compound to determine which light source was best suited to photolytically decomplexing the samples. The reason **4a** was chosen was that the demetallated product (**5**) displayed low solubility in hydrocarbon solvents such as hexane, which aided in precipitation and isolation of the product (**5**), but was soluble in halogenated solvents so as to permit facile workup. The demetallation sequence is displayed in Scheme 3.2.3.

Photolysis with any of the light sources liberated the pure organic analogue. Regardless of wavelength, once successfully demetallated, the NMR, IR and TGA spectra were the same. Tables 3.2.4 and 3.2.5 provide the spectroscopic and thermal data. Samples were irradiated at various times (15, 30, 45, 60, 120, 180, 300, 480 minutes) to determine the time required to decomplex the sample. It was observed that once decomplexed, irradiation for further time produced no noticeable affect on the product. The ^{1}H and ^{13}C spectra of compound **5** are provided in Figure 3.2.8 and 3.2.9. These spectra were obtained after 1 hour of 300 nm light irradiation. As is evident, successful decomplexation can be established by the loss of the Cp resonance and downfield shift of the complexed aromatic protons. The aromatic protons are thoroughly overlapped, however one can distinguish the large singlet at 7.12 ppm denoting the equivalent protons on the aromatic rings with terminal isopropylidene linkages. The methyl peaks appear at 1.65 ppm as a broad singlet. The ^{13}C spectrum displayed a similar loss of the Cp resonance. Four aromatic CH peaks were observed for the aromatic CH carbons alpha to the ether groups due to the slight differences existing between those near the terminus of the molecule and those located in the middle.

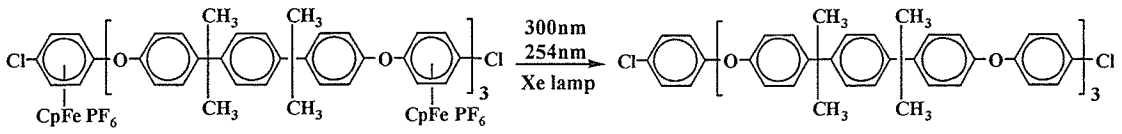

4a

Scheme 3.2.3

5

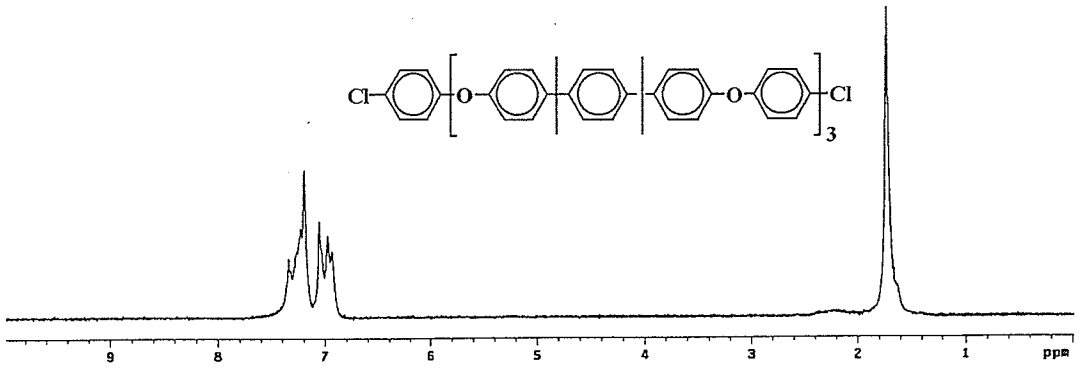

Figure 3.2.8: ^{1}H NMR spectrum for compound **5**

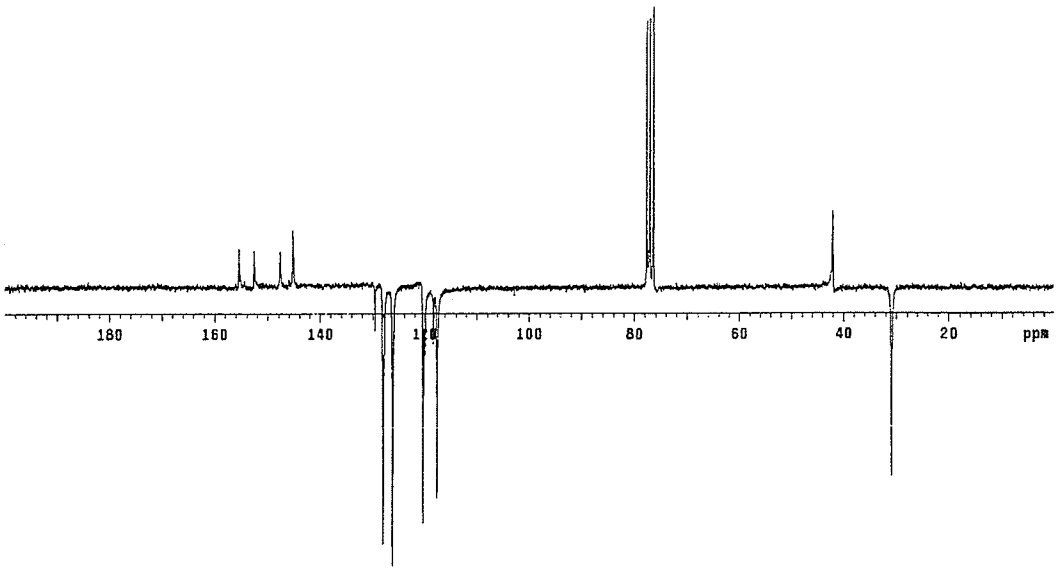

Figure 3.2.9: ^{13}C NMR spectrum for compound **5**

The difference between the three wavelengths of light used lies in the time required for the photolytic decomplexation to be complete. The 300 nm irradiations were complete in 1 hour, while those using a Xe lamp required 5 hours and those with 254 nm light required 8 hours. The differences can partly be explained by intensity differences, with the 300 nm > Xe > 254 nm as discussed in Section 3.1. Another plausible reason is that the absorbance of the iron moiety falls in the range of 300-450 nm[26-28,134]. The UV spectrum of **4a** displayed a small band in the 350-400 nm region, which is consistent with a ligand field transition of an organoiron complex[26-28,134]. Thus, irradiation with wavelengths near this absorbance would facilitate decomplexation. This could also explain why the Xe lamp (which produces all wavelengths of the solar spectrum) showed a faster rate than 254 nm. The lower intensity of the Xe lamp, when compared to the 300 nm photoreactor, would explain why the 300 nm rate was higher than that observed with the Xe lamp.

Samples that were irradiated for less than the required time displayed peaks in the NMR and IR that corresponded to complexed material. ^{1}H NMR spectra displayed Cp resonances, while IR spectra and TGA curves exhibited the presence of the iron moiety with an absorbance at 840 cm^{-1} (P-F bond vibration), and a weight loss near 230°C, respectively. Upon successful decomplexation, the IR absorbance between 840-845 cm^{-1} disappeared and revealed an absorbance around 830 cm^{-1} that was hidden previously. TGA curves of compound **5** displayed only one weight loss corresponding to destruction of the organic molecule.

Figures 3.2.10 and 3.2.11 display the IR spectra of a 300 nm photolysis of **4a** after 15 minutes and 1 hour, respectively. As is evident, the 15 min photolysis is not

complete, while at 1 hour, the absorbance due to the $CpFePF_6$ group is no longer present. As a comparison, Figure 3.2.12 and 3.2.13 present the IR spectra of **4a** after a 5 hour photolysis with 254 nm light, and simulated sunlight. Similarly, Figure 3.2.14 presents a TGA curve comparing a 1 hour 300 nm photolysis with a 5 hour 254 nm photolysis. As is evident, the 254 nm sample displays the presence of starting complex **4a**.

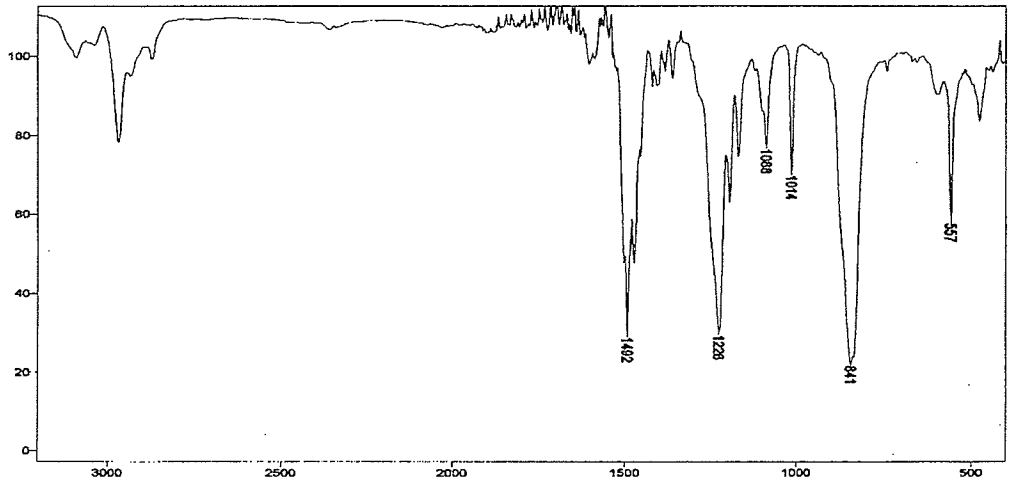

Figure 3.2.10: 15 min photolysis of **4a** with 300nm light

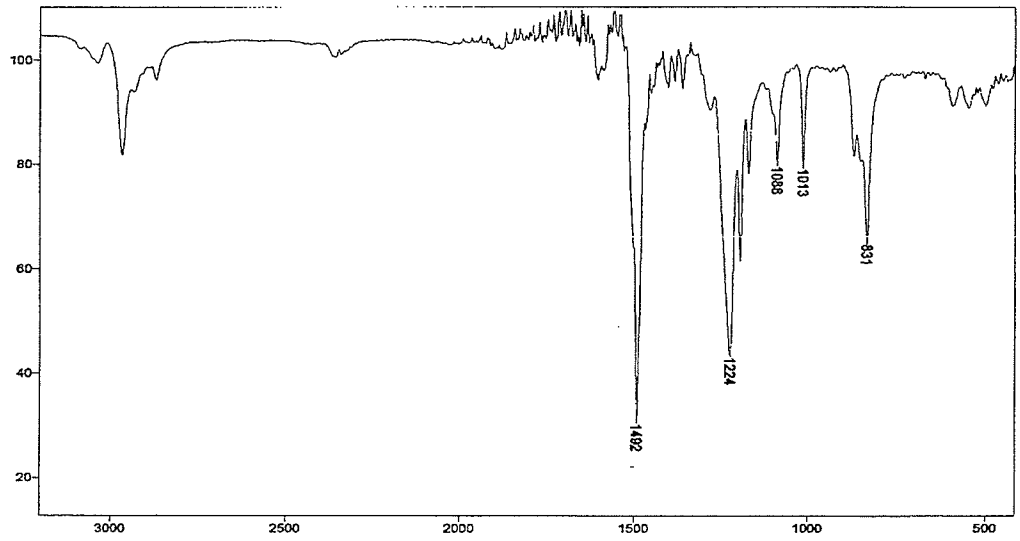

Figure 3.2.11: 1 hour photolysis of **4a** with 300nm light

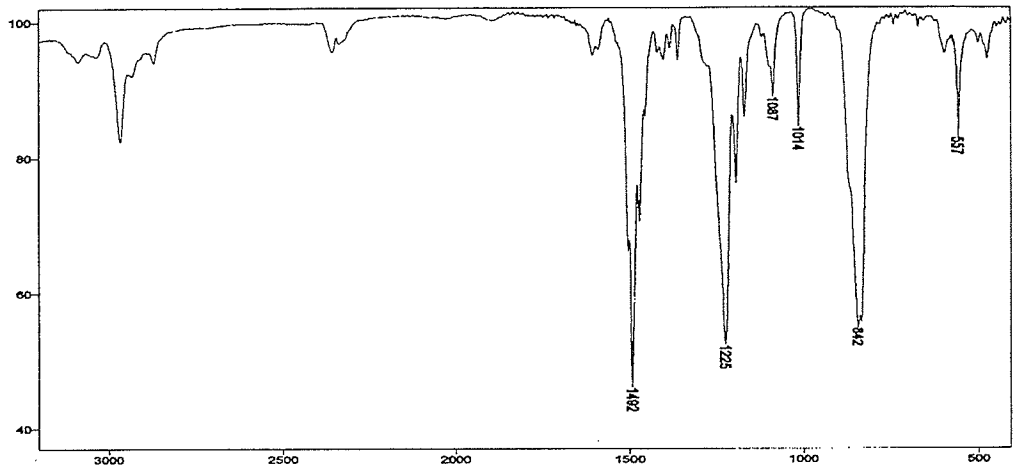

Figure 3.2.12: 5 hour photolysis of **4a** with 254 nm light

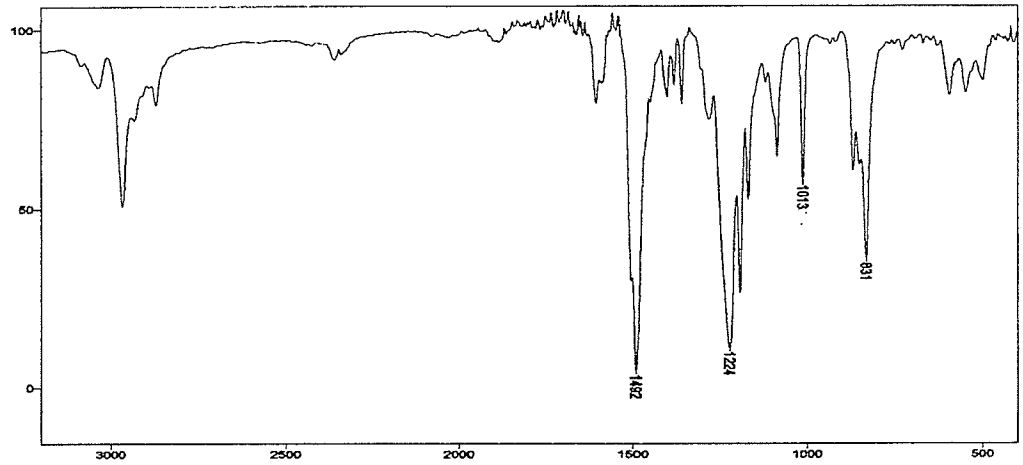

Figure 3.2.13: 5 hour photolysis of **4a** with a Xe lamp

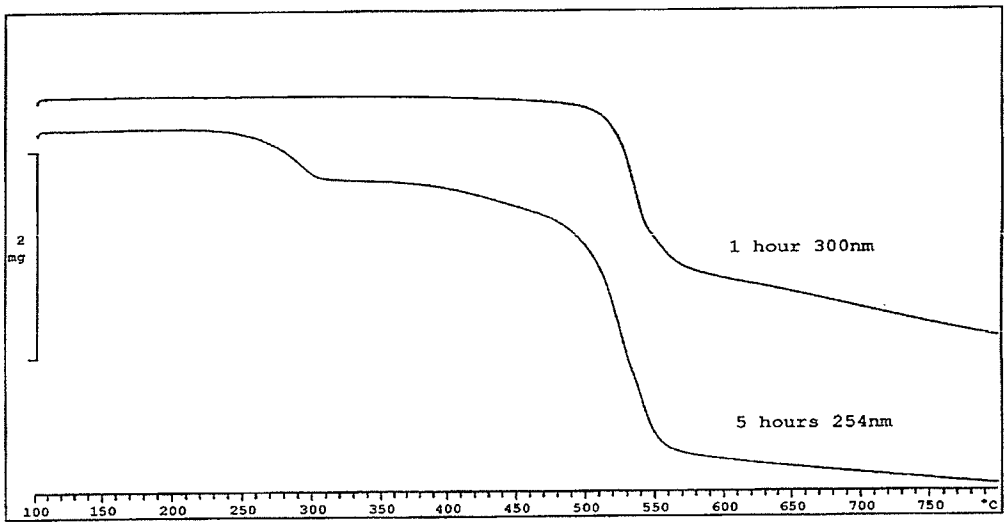

Figure 3.2.14: TGA curves of a 1 hour 300 nm and a 5 hour 254 nm irradiation of **4a**

Table 3.2.4: ^{1}H and ^{13}C data for decomplexed compound **5**

δ (ppm) in chloroform-d						
	^{1}H Aromatic H	**^{1}H CH_3**	**^{13}C Ar quat**	**^{13}C ArCH**	**^{13}C CH_3**	**^{13}C Others**
5	6.87 (d, 12H, J=8.9) 6.96 (d, 12H, J=6.0) 7.12 (s, 12H) 7.15-7.29 (br m, 16H)	1.65 (s, 36H)	145.32 147.67 152.64 155.48	117.53 118.22 119.91 120.32 126.26 128.01 129.60	30.87	42.04*

Coupling constants calculated in Hz *quaternary carbon

Table 3.2.5: Yield, IR and TGA data for compound **5**

	%Yield	**IR (cm^{-1})**	**TGA_{onset}**	**TGA_{endset}**	**$TGA_{midpoint}$**	**%loss**
5	75	832	521	552	537	54

3.2.3 Choice of solvent and anion

Given that the fastest successful decomplexation was observed with 300 nm light, all subsequent experiments utilized this wavelength. A study of the effects of the choice of solvent and the nature of the anion were investigated following the wavelength study.

i) Solvent

As outlined in Section 1.1.1, the use of any slightly nucleophilic solvent will allow photolytic decomplexation to occur. However, there remained the question of whether the times for the decomplexation would change depending on the nature of the solvent. Using complex **4a**, and 300 nm light, a series of solvent experiments were conducted. Four new solvent compositions were prepared and compared to the previous results with 300 nm light (which used a 4:1 CH_2Cl_2:CH_3CN mixture). Solutions of pure CH_3CN, 1:1 CH_2Cl_2:CH_3CN, pure CH_2Cl_2, and a 3.5:1:0.5 CH_2Cl_2:CH_3CN:CH_3OH mixture were used. CH_3CN was present in all but one of the solvent choices due to the established success with this solvent[24-30].

The results showed that using any solvent composition which incorporated acetonitrile allowed successful decomplexation of **4a** to occur in 1 hour with 300 nm light. The only noticeable change for CH_3CN containing solvents was observed with the sample containing methanol. For these photolyses, there was no observation of a blue colour in the water washings during subsequent workup that was typically observed with the other samples. The colour may be attributed to a type of ferrous cyano hydrate, $Fe^{III}_4[Fe^{II}(CN)_6]15H_2O$, or ferricenium tetrachloroferrate, $[Fe(C_5H_5)_2]FeCl_4$[26]. The lack of this colouration indirectly supports the role of the more nucleophilic methanol in the

liberation of the organic backbone. Lastly, the trial employing only distilled CH_2Cl_2 was observed to take longer than those with CH_3CN present. Successful decomplexation was observed to require 3 hours when no CH_3CN was included in the solvent mixture.

ii) Anion

A comparison of compounds **4a** and **4b** subjected to 300 nm light photolysis utilizing a 4:1 CH_2Cl_2:CH_3CN ratio was performed. It was found that inclusion of BF_4^-, which is known to be more nucleophilic than PF_6^-, caused no change in the decomplexation time. Although, as outlined in Section 1.1.1, the mechanism of decomplexation may vary, no change in the end product, or time required to produce it, was observed. Samples of **4b** irradiated for 15, 30, 60, 120, and 180 minutes displayed the same trend as **4a**; successful decomplexation in 1 hour, with no change observed with further irradiation.

3.2.4 Comparison with pyrolytic sublimation

Since it has been established that successful decomplexation of **4a** can be performed in about an hour in numerous solvent ratios incorporating CH_3CN, a comparison to another conventional technique was examined. Pyrolytic sublimation was used for compound **4a**. The sample was heated under vacuum to 250°C for 1-3 hours, after which time the apparatus was cooled and the 'cold-finger' rinsed with chloroform. A 1 hour pyrolysis of **4a** did not form compound **5**. Thus, a 2 and 3 hour pyrolysis was performed that did form the product, **5**, but the yield of the reaction was only 20%. Given that the 1 hour photolysis produced **5** in approximately 75% yield, the pyrolytic

demetallation technique offered no advantages for complex **4a** when compared to photolysis with 300 nm light.

3.2.5 Decomplexation of organoiron complexes

Photolysis of compounds **3a-h** with 300 nm light in a 4:1 CH_2Cl_2:CH_3CN solvent mixture allowed for the isolation of the organic analogues **6a-g** (Scheme 3.2.4). The times required were on the order of 45 minutes to 1 hour for **6a-c**, and **6e**, with compounds **6d**, **6f** and **6g** requiring only 30 minutes for successful decomplexation. Tables 3.2.6 and 3.2.7 provide the spectroscopic and thermal data for compounds **6a-g**.

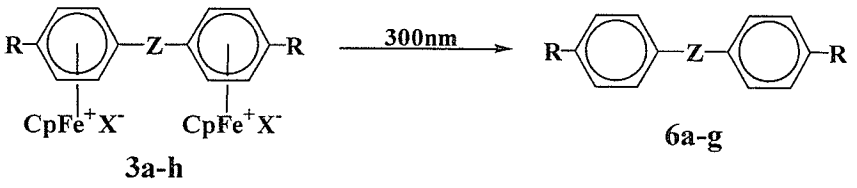

3a-h **6a-g**

	R	X^-	Z
3a:	Cl	PF_6	2a
3b:	Cl	PF_6	2b
3c:	Cl	BF_4	2b
3d:	H	PF_6	2b
3e:	Cl	PF_6	2c
3f:	Cl	PF_6	2d
3g:	H	PF_6	2e
3h:	Cl	PF_6	2f

	R	Z
6a:	Cl	2a
6b:	Cl	2b
6c:	H	2b
6d:	Cl	2c
6e:	Cl	2d
6f:	H	2e
6g:	Cl	2f

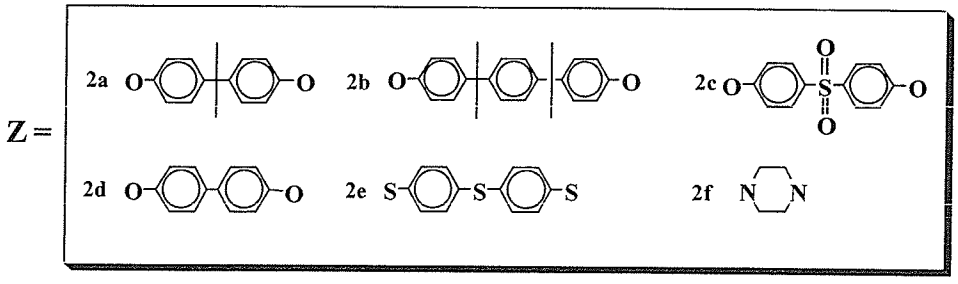

Scheme 3.2.4

The ^{1}H and ^{13}C NMR spectra of compounds **3d** and **6c** are provided for comparison in Figures 3.2.15 and 3.2.16. The spectra display the characteristic loss of the Cp resonance, and the downfield shift of the formerly complexed aromatic protons. The aromatic region of the ^{13}C spectrum of **6c** displays six aromatic CH carbon peaks in accordance with the decomplexed structure. This compares well with the metallated form in which three aromatic CH carbon peaks resonate between 80-95 ppm due to complexation of the terminal arenes, while the other three aromatic carbon CH peaks appear in the aromatic region.

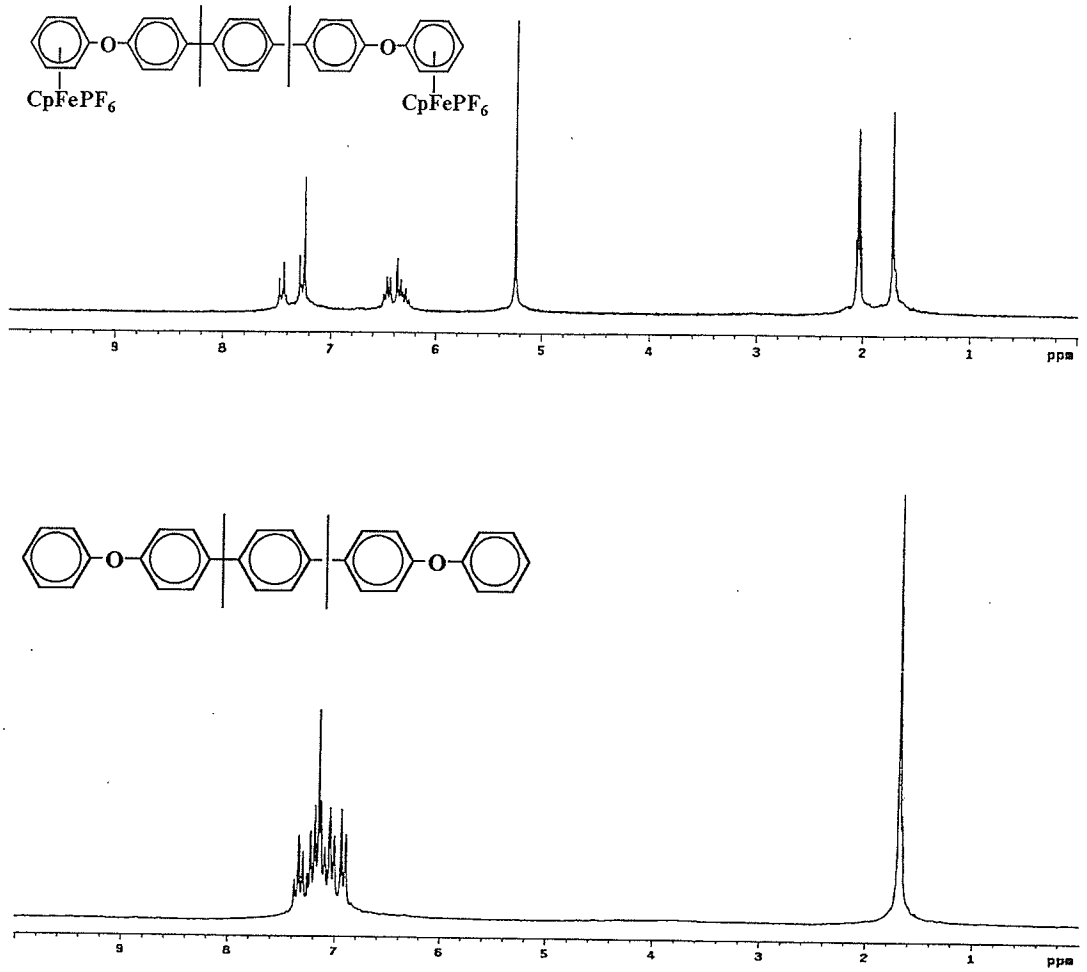

Figure 3.2.15: ^{1}H NMR spectra of **3d** (top) and **6c** (bottom)

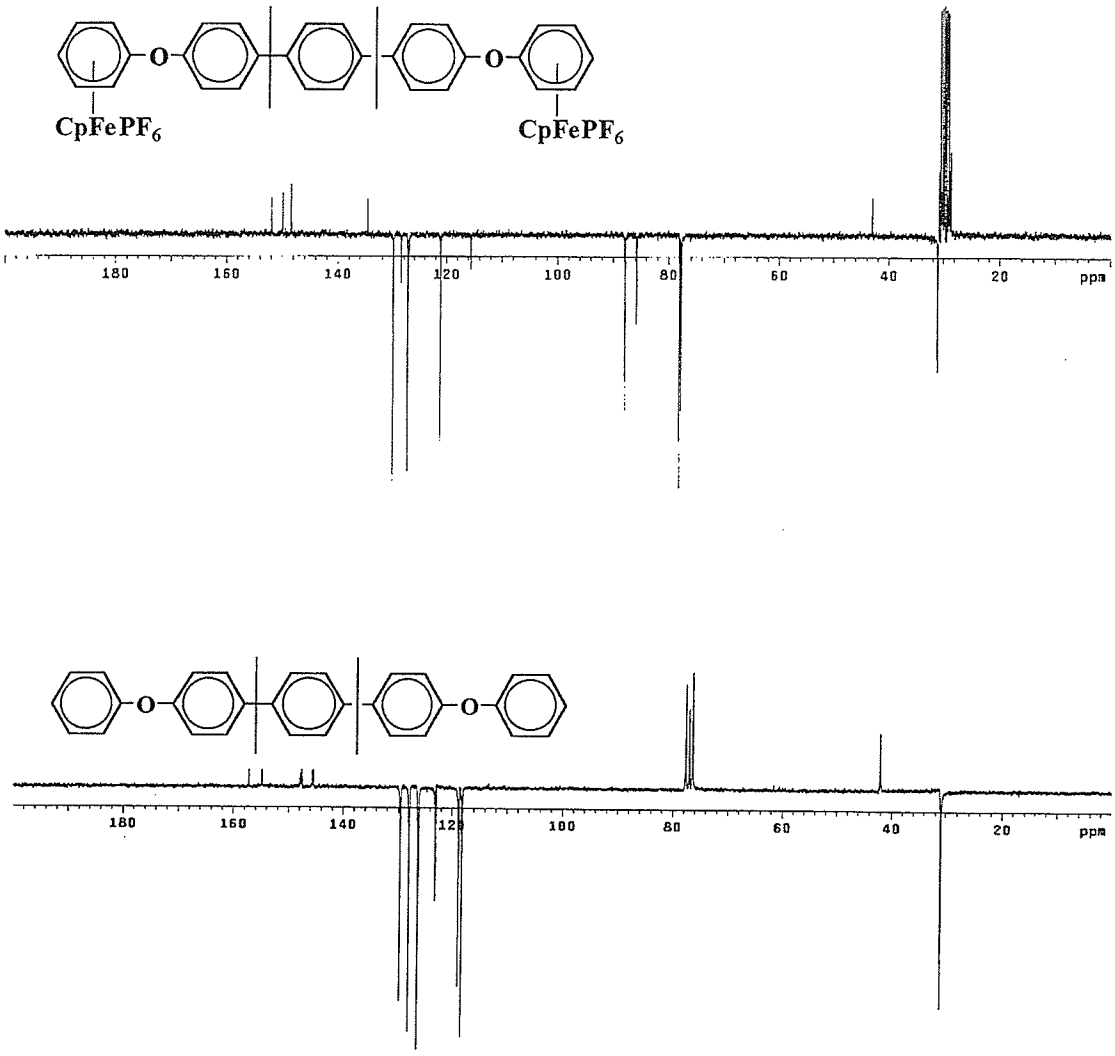

Figure 3.2.16: ^{13}C NMR spectra of **3d** (top) and **6c** (bottom)

Analysis of the IR spectra of compounds **6a-g** illustrated the appearance of a similar peak near 830 cm^{-1}, as observed with compound **5**. Table 3.2.7 lists the wavenumber of this peak for compounds **6a-g**. Figure 3.2.17 displays the change in the IR spectrum upon decomplexation of **3e** to form **6d**. The TGA curve of the decomplexed samples showed only one weight loss, corresponding to destruction of the organic compound, for compounds **6a-c,e-f**, while compounds **6d** and **6g** displayed two

weight losses. These weight losses did not match those of the complexed analogues, thus may be attributed to the formation of intermediate thermolysis products which themselves underwent degradation with increased temperature. Figure 3.2.18 provides the TGA curves for complex **3h** and its organic analogue **6g** for comparison.

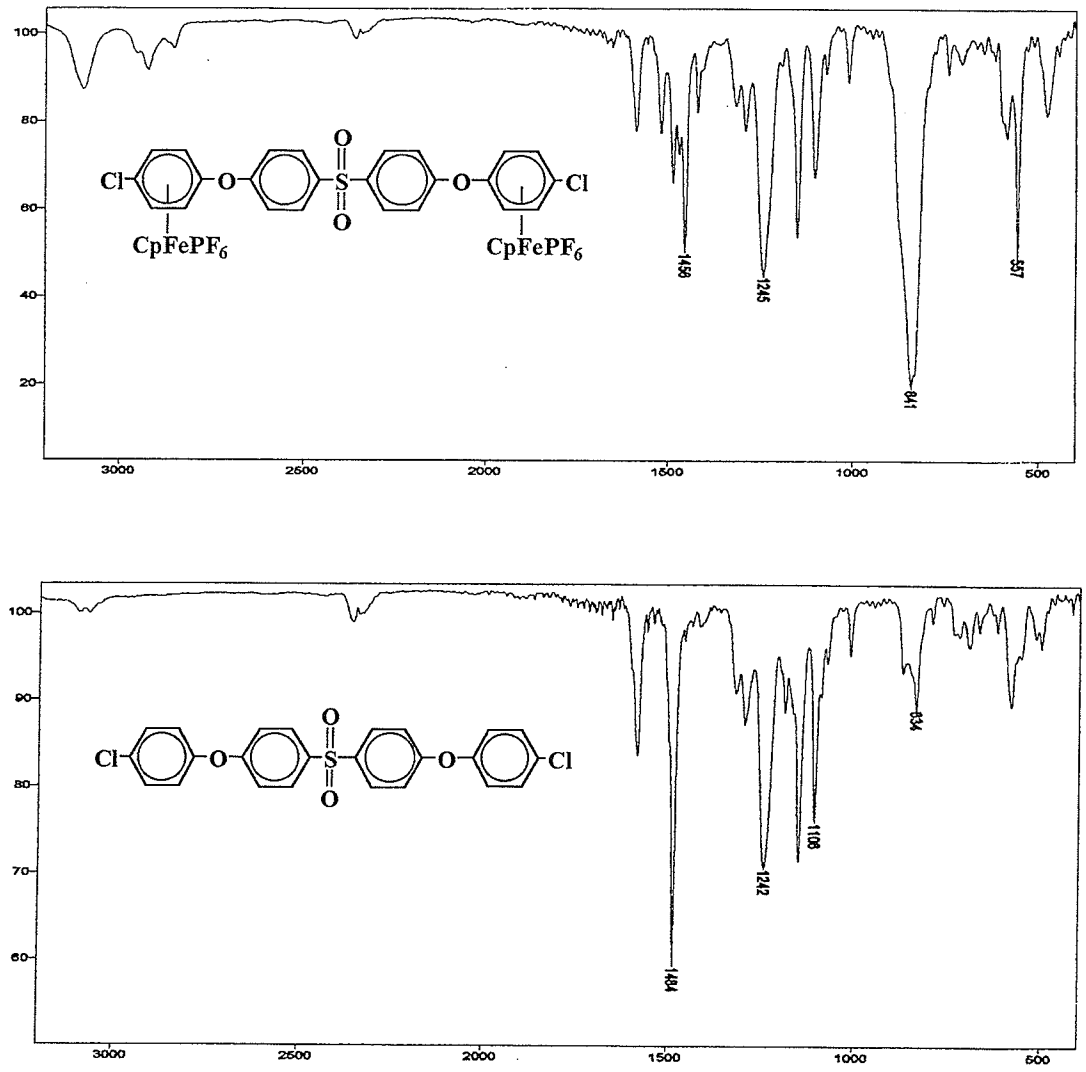

Figure 3.2.17: IR spectrum of **3e** (top) and **6d** (bottom)

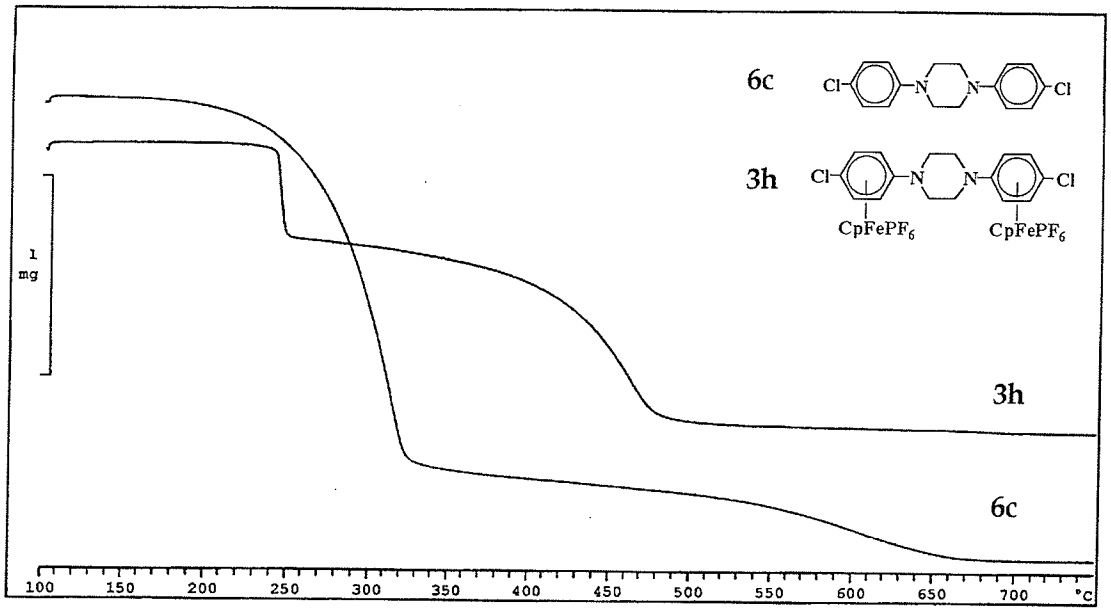

Figure 3.2.18: TGA curves for complex **3h** and its decomplexed analogue **6g**

Table 3.2.6: ^{1}H and ^{13}C NMR data for compounds **6a-g**

δ (ppm) in chloroform-d						
	^{1}H Aromatic H	**^{1}H CH_2,CH_3**	**^{13}C quats**	**^{13}C ArCH**	**^{13}C CH_2,CH_3**	**^{13}C Others**
6a	7.15-7.24 (m, 8H) 7.47 (d, 4H, J=8.6) 7.55 (d, 4H, J-8.2)	1.95 (s, 6H) CH_3	127.4 145.8 154.61 155.98	118.29 119.90 128.09 129.61	30.97 CH_3	42.10*
6b	6.86-6.96 (m, 8H) 7.13 (s, 4H) 7.20 (d, 4H, J=8.9) 7.27 (d, 4H, J-8.9)	1.67 (s, 12H) CH_3	145.94 147.52 154.40 155.92	118.15 119.84 126.20 128.90 129.51	30.85 CH_3	42.06*
6c	6.92 (d, 4H, J=8.6) 7.01-7.05 (m, 4H) 7.09-7.23 (m, 12H) 7.30-7.38 (m, 4H)	1.69 (s, 12H) CH_3	145.51 147.51 154.59 157.23	118.10 118.72 122.96 126.20 127.98 129.57	30.89 CH_3	42.05*
6d	6.95-7.07 (m, 8H) 7.36 (d, 4H, J=9.0) 7.82-7.90 (m, 4H)	-------	135.61 151.64 153.40 161.49	117.75 121.54 129.76 130.16	-------	-------
6e	6.99 (d, 4H, J=8.5) 7.05 (d, 4H, J=8.5) 7.31 (d, 4H, J=8.9) 7.53 (d, 4H, J=8.6)	-------	128.32 135.85 155.77 156.26	119.12 120.10 128.26 129.73	-------	-------
6f	7.22 (s, 8H) 7.29-7.36 (m, 10H)	-------	133.57 134.29 135.21	127.20 128.99 130.56 131.78 131.32	-------	-------
6g	6.91 (d, 4H, J=8.2) 7.24 (d, 4H, J=8.2)	3.31 (s, 8H) CH_2	131.03 149.57	117.61 129.03	49.38 CH_2	------

Coupling constants calculated in Hz *quaternary carbon

Table 3.2.7: Yield, IR and TGA data for compounds **6a-g**

	%Yield	IR (cm^{-1})	TGA_{onset} (°C)	TGA_{endset} (°C)	$TGA_{midpoint}$ (°C)	% Weight loss
6a	81	828	351	405	376	53
6b	80	829	356	426	390	63
6c	90	835	375	432	397	61
6d	84	834	345 480	422 539	385 510	29 16
6e	85	822	347	385	362	81
6f	67	833	327	388	358	45
6g	93	817	278 430	323 649	298 596	73 13

3.3 Azo dyes containing cationic cyclopentadienyliron moieties

3.3.1 Synthesis of azo dye starting materials

A series of 'parent' azo dye compounds were synthesized via conventional techniques as illustrated in Scheme 3.3.1. The dyes were specifically chosen due to their ability to undergo a subsequent reaction with a cyclopentadienyliron complex, and were characterized using NMR, IR, TGA and UV-Vis techniques (Tables 3.3.2-3.3.4).

The ^{1}H and ^{13}C NMR spectra of **9d** are provided in Figure 3.3.1 and 3.3.2, respectively. The ^{1}H spectrum displays doublets in the aromatic region, which is consistent with the structure. The doublet at 6.81 ppm is characteristic of aminoazobenzene dyes and belongs to the aromatic protons alpha to the amino nitrogen. The doublet resonating furthest downfield, at 8.04 ppm, results from the protons alpha to the carboxylic acid group. The multiplets between 3.5-3.9 ppm are attributed to the methylene protons of the ethyl groups, while the methyl proton resonates as a triplet at 1.17 ppm. Lastly, the small peak around 4.7 ppm and 13 ppm are due to the hydrogens located on the alcohol and carboxylic acid, respectively.

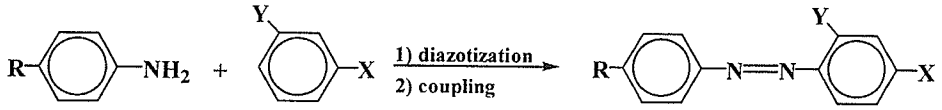

7a-e **8a-c** **9a-g**

	R
7a:	H
7b:	NO_2
7c:	$COCH_3$
7d:	COOH
7e:	OH

	X	Y
8a:	1	H
8b:	2	H
8c:	OH	OH

	X	Y	R
9a:	1	H	H
9b:	1	H	NO_2
9c:	1	H	$COCH_3$
9d:	1	H	COOH
9e:	1	H	OH
9f:	2	H	OH
9g:	OH	OH	OH

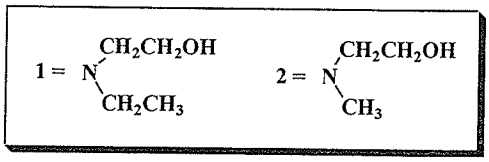

Scheme 3.3.1

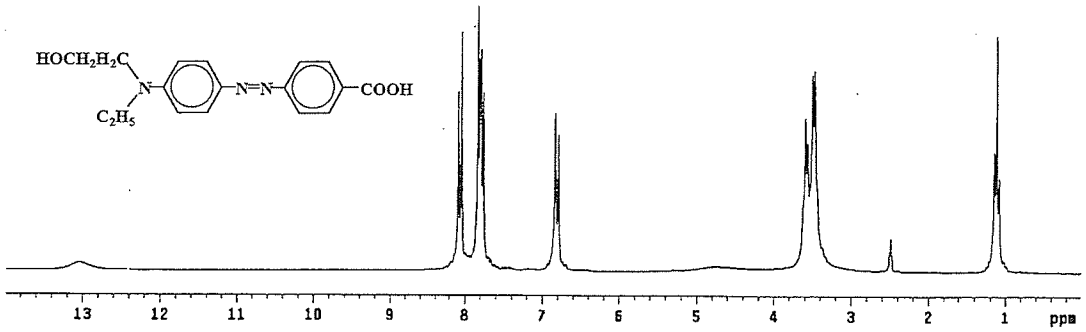

Figure 3.3.1: ^{1}H NMR spectrum for **9d**

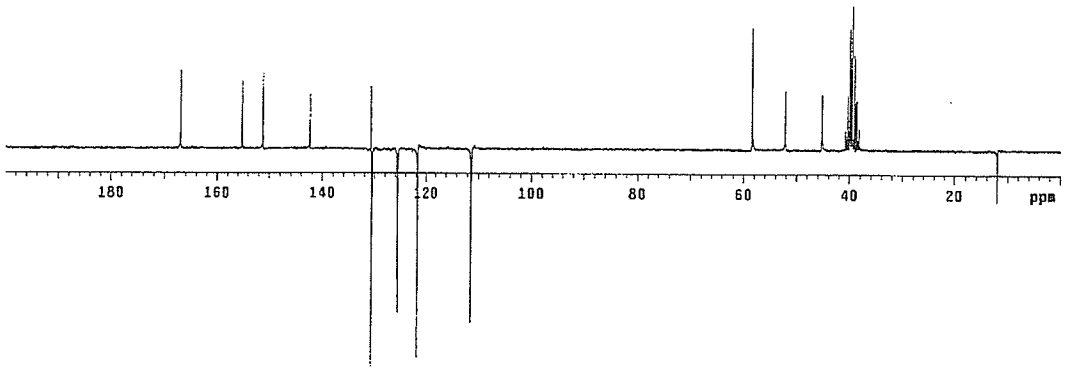

Figure 3.3.2: ^{13}C NMR spectrum for **9d**

The ^{13}C NMR spectrum displays five quaternary carbons, which is consistent with the structure (four aromatic quaternary carbons and one carbonyl carbon). The quaternary carbon furthest downfield denotes the carbonyl, while the quaternary carbons alpha to the azo bond resonate at 155.18 ppm, and 142.37 ppm for the azo component and coupling component, respectively. Of the remaining quaternary carbons, the 151.23 ppm resonance belongs to the quaternary carbon alpha to the amino group, while the 130.71 ppm peak results from the carbon alpha to the carboxylic acid group.

The visible absorption of the dyes were recorded in dimethylformamide, ethanol and a solution of 10% HCl in ethanol. Table 3.3.1 provides the values of the wavelength maxima. As was expected, the dyes displayed bathochromic shifts in DMF when compared to ethanol, and exhibited characteristic ammonium and azonium bands upon acidification (Section 1.2.2, *viii*). The azonium peak commonly displayed a high wavelength shoulder or was slightly split into two peaks. This is due to the strong acid used, which may protonate both nitrogens of the azo group. Dyes containing stronger electron-withdrawing groups showed longer wavelength absorption bands. Figure 3.3.3 illustrates the difference between the presence of a 4'-$COCH_3$ group (**9c**) and a 4'-NO_2 (**9b**) group on the UV-Visible spectrum of an aminoazobenzene.

Table 3.3.1: Wavelength maxima (nm) for azo dyes **9a-g**

Compound	DMF	Ethanol	Ethanol/HCl
9a	416	413	318 ; 521 ; 541
9b	501	487	326 ; 515 ; 534
9c	463	453	330 ; 522 ; 540
9d	452	442	321 ; 518 ; 539
9e	418	409	357 ; 564
9f	414	407	358 ; 567
9g	388	385	385 ; 498

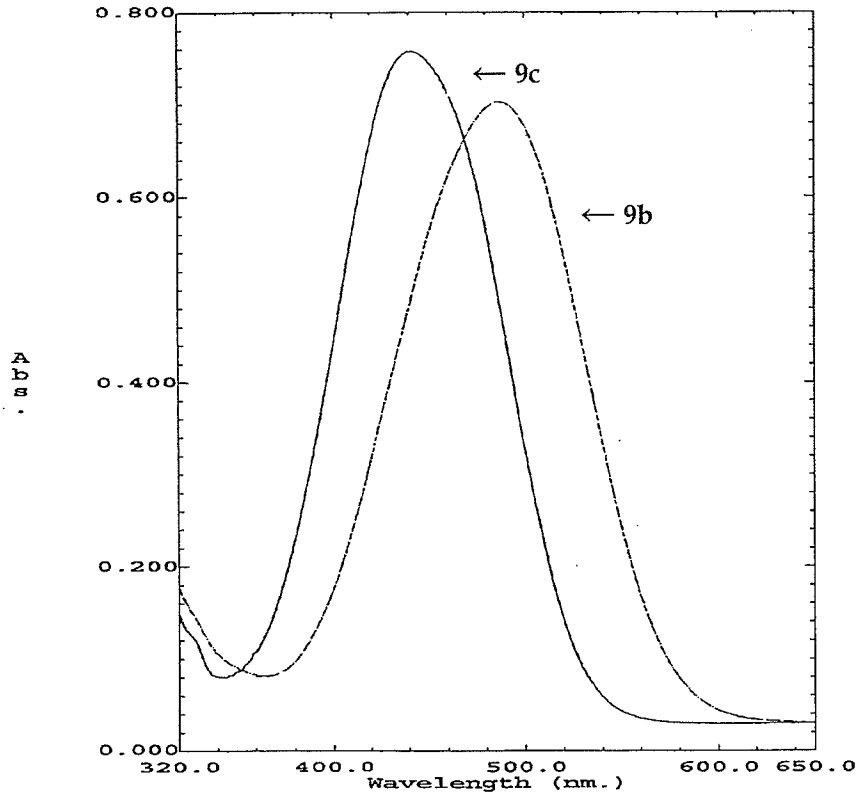

Figure 3.3.3: UV-Vis absorbance of **9b** and **9c** in ethanol

Table 3.3.2: ^{1}H NMR data for dyes **9a-g**

δ (ppm) in acetone-d_6				
	Aromatic H	**CH_2**	**CH_3**	**Others**
9a	6.85-6.99 (m, 2H) 7.38-7.48 (m, 2H) 7.49-7.53 (m, 2H) 7.75-7.86 (m, 3H)	3.48-3.69 (m, 4H) 3.78 (q, 2H, J=6.1)	1.21 (t, 3H, J=7.0)	3.90 (s, 1H) OH
9b	6.91 (d, 2H, J=9.3) 7.87 (d, 2H, J=9.3) 7.96 (d, 2H, J=9.0) 8.36 (d, 2H, J=9.0)	3.52-3.67 (m, 4H) 3.81 (q, 2H, J=6.0)	1.23 (t, 3H, J=7.1)	3.95 (s, 1H) OH
9c	6.72-6.93 (m, 2H) 7.72-7.81 (m, 4H) 8.00-8.15 (m, 2H)	3.26-3.70 (m, 8H)	1.13 (m, 3H) 2.60 (s, 3H)	4.85 (s, 1H) OH
9d	6.81 (d, 2H, J=8.9) 7.78 (d, 2H, J=8.9) 7.81 (d, 2H, J=8.6) 8.04 (d, 2H, J=8.6)	3.54-3.67 (m, 4H) 3.74-3.83 (m, 2H)	1.17 (t, 3H, J=6.6)	4.73 (s, 1H) OH 13.04 (s, 1H) COOH
9e	6.83 (d, 2H, J=9.2) 6.94 (d, 2H, J=8.9) 7.72 (d, 2H, J=8.9) 7.75 (d, 2H, J=9.2)	3.48-3.61 (m, 4H) 3.77 (q, 2H, J=6.9)	1.19 (t, 3H, J=7.1)	3.86 (s, 1H) OH aliphatic 8.79 (s, 1H) OH aromatic
9f	6.84 (d, 2H, J=9.4) 6.95 (d, 2H, J=8.6) 7.73 (d, 2H, J=8.6) 7.76 (d, 2H, J=9.4)	3.55-3.62 (m, 2H) 3.72-3.82 (m, 2H)	3.11 (s, 3H)	3.89 (s, 1H) OH aliphatic 8.82 (s, 1H) OH aromatic
9g	6.39 (d, 1H, J=2.7) 6.58 (dd, 1H, J=8.8, 2.5) 7.04 (d, 2H, J=9.0) 7.68 (d, 1H, J=8.6) 7.76 (d, 2H, J=9.0)	-------	-------	10.14 (s,1H) 10.36 (s, 1H) 12.47 (s, 1H)

Table 3.3.3: ^{13}C NMR data for compounds **9a-g**

δ (ppm) in acetone-d_6				
	quat	**ArCH**	**CH_2**	**CH_3**
9a	142.15 150.58 152.48	111.08 121.72 124.98 129.16 129.38	45.05 52.11 58.32	11.98
9b	142.52 146.65 151.84 156.26	111.42 122.35 124.89 126.14	45.27 52.17 58.37	11.99
9c	136.53 142.45 151.28 155.17 197.18 (C=O)	111.26 121.76 125.65 129.45	45.19 52.15 58.38	12.01 26.79
9d	130.71 142.37 151.23 155.18 166.95 (C=O)	111.26 121.67 125.58 130.51	45.18 52.16 58.38	12.01
9e	143.88 147.54 151.01 159.88	112.01 116.39 124.59 125.24	46.19 53.31 60.03	12.35
9f	144.09 147.51 152.95	112.20 116.41 124.63 125.06	55.31 59.94	39.42
9g	132.98 144.79 156.29 152.43 160.67	103.93 109.27 116.85 124.23 134.62	-------	-------

Table 3.3.4: Yield, IR and TGA data for dyes **9a-g**

	Yield	IR (cm^{-1})	TGA_{onset}	TGA_{endset}	$TGA_{midpoint}$	% Weight Loss
9a	90	3412 (OH)	221	256	239	84
9b	93	3281 (OH)	262	321	291	75
9c	92	3429 (OH) 1663 (C=O)	252	292	271	34
9d	93	2998 (OH) 1682 (C=O)	211	254	236	44
9e	95	3246 (OH)	215	253	235	46
9f	90	3194 (OH)	210	257	237	40
9g	92	3199 (OH)	236 541	241 672	239 612	14 49

3.3.2 Reaction with cyclopentadienyliron complexes

A variety of cyclopentadienyliron complexed azo dyes were prepared as shown in Schemes 3.3.2-3.3.5. The versatility of the metal-mediated nucleophilic aromatic substitution methodology allowed for the isolation of complexed dyes that varied significantly in structure. Dyes **11a-b** are examples of monometallic complexes that incorporate the aminoazobenzene functionality. Alternatively, dyes **13a-c** have the dye chromophore positioned in a pendant manner to the complexed chain, while dyes **17a-d** are bimetallic complexes which enclose the azo dye between two complexed arenes. Lastly, complexed dye **15** is classified as a disazo dye due to the presence of two azo groups[69]. All dyes were structurally characterized by NMR, and IR spectrometry and TGA (Tables 3.3.7-3.3.11).

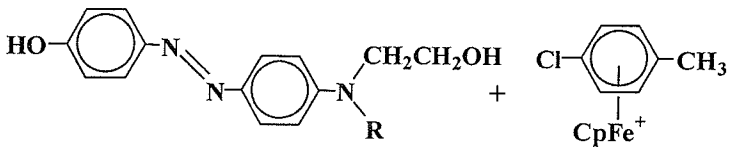

9e-f **10**

9e: R = CH_2CH_3
9f : R = CH_3

K_2CO_3
N_2, DMF

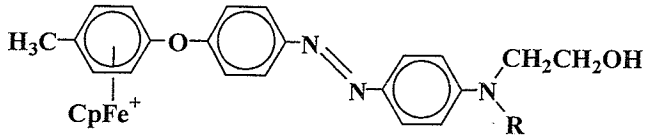

11a-b

11a: R = CH_2CH_3
11b: R = CH_3

Scheme 3.3.2

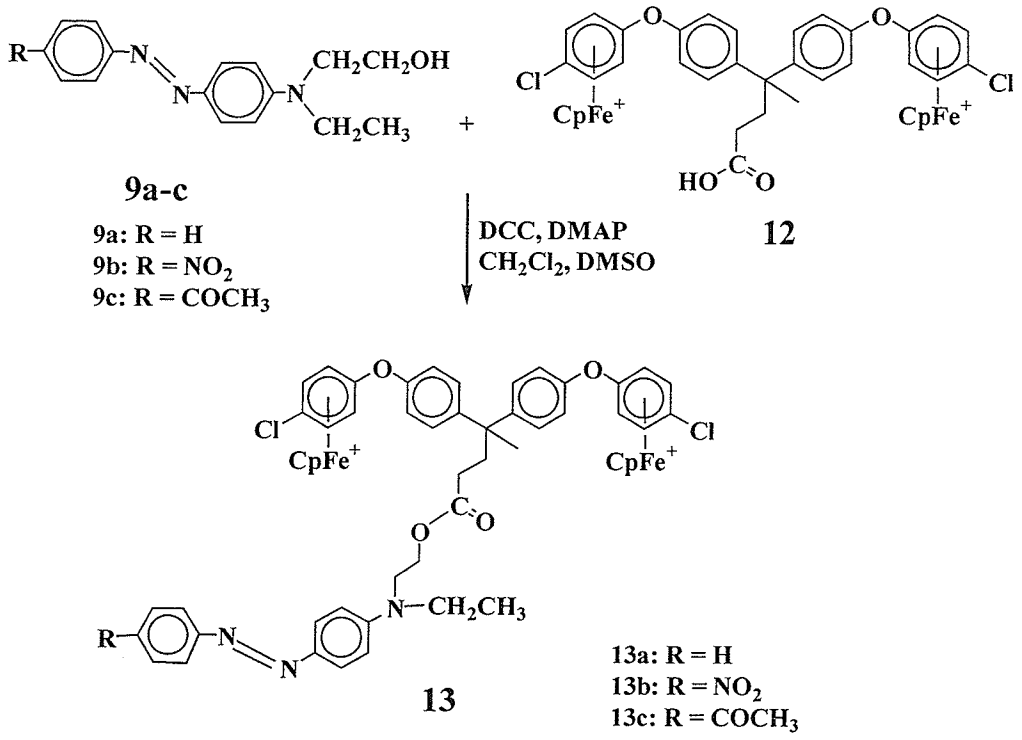

Scheme 3.3.3

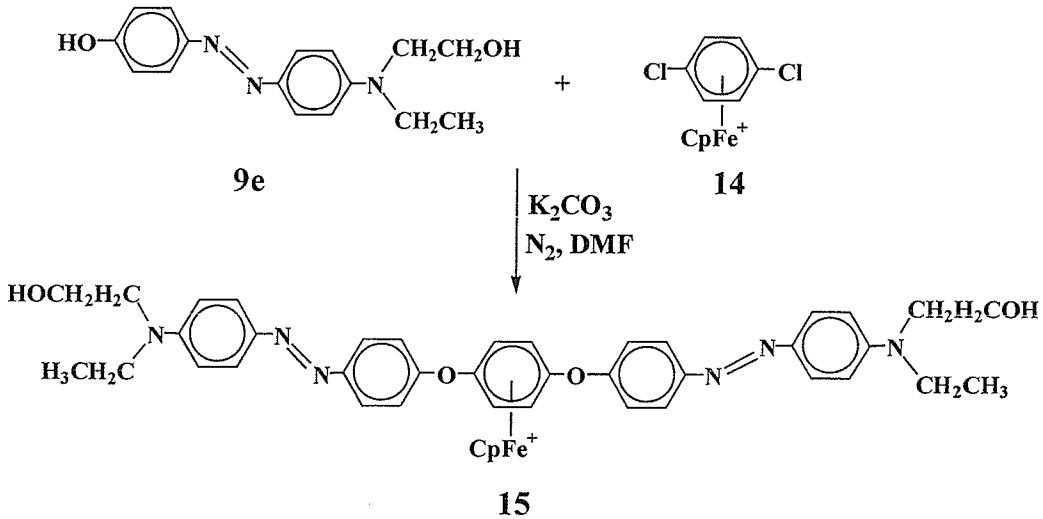

Scheme 3.3.4

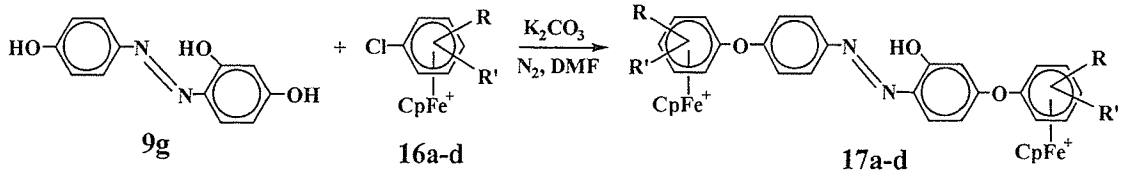

16a: R = R' = H
16b: R = *p*-CH_3, R' = H
16c: R = *m*-CH_3, R' = H
16d: R = *p*-CH_3 R'= *m*-CH_3

17a: R = R' = H
17b: R = *p*-CH_3, R' = H
17c: R = *m*-CH_3, R' = H
17d: R = *p*-CH_3 R'= *m*-CH_3

Scheme 3.3.5

i) Complexed dyes synthesized from ***9a-f***

Figure 3.3.4 presents the ^{1}H NMR spectrum of complexed dye **13a**. The Cp and complexed aromatic proton resonances can be clearly distinguished, in addition to the doublet at 6.99 ppm, which denotes the aromatic protons alpha to the amino bond. The series of peaks between 2-4.5 ppm represent the various methylene protons, while the methyl protons appear upfield at 1.22 ppm and 1.68 ppm.

The ^{13}C NMR of **13a** is provided in Figure 3.3.5. As can be seen, there are a series of quaternary carbons, with the furthest downfield representing the carbonyl carbon of the new ester link. The other noteworthy peak is that of the quaternary aliphatic carbon resonating at 45.42 ppm, which falls along side the peaks for the methylene carbons of the molecule.

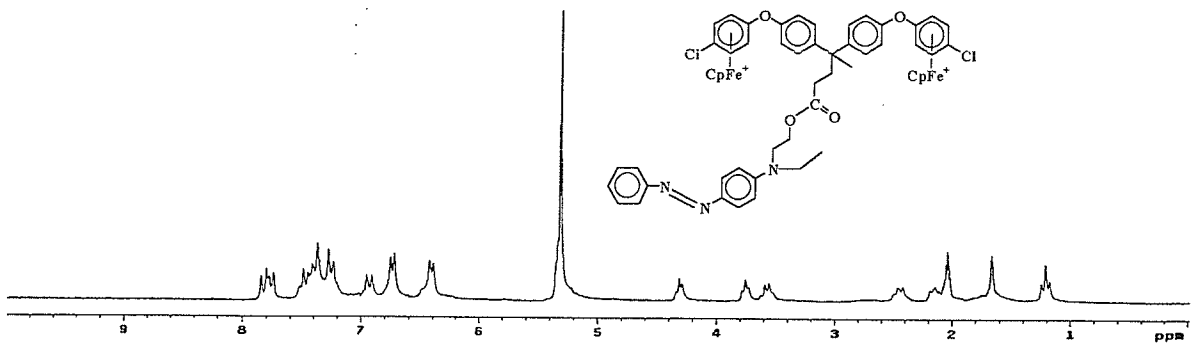

Figure 3.3.4: ^{1}H NMR spectrum of **13a**

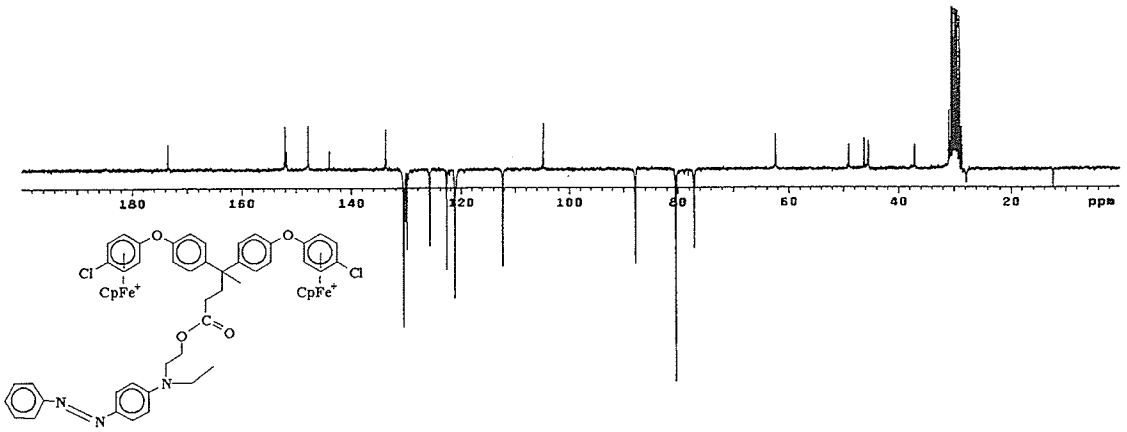

Figure 3.3.5: ^{13}C NMR spectrum of **13a**

The visible absorbance of the dyes was altered to varying degrees upon inclusion of complexed arenes. Given that the wavelength maxima of azo compounds are greatly influenced by the structure of the dye, it is understandable that the various types of complexed dyes would exhibit varying degrees of change when compared to their parent starting material. Table 3.3.5 provides the wavelength maxima of dyes **11a-b**, **13a-c** and **15** in DMF, ethanol and acidified ethanol. Also included in Table 3.3.5 are the wavelength maxima of the corresponding parent dye, and the shift in wavelength observed on formation of the complexed dye. For the HCl/ethanol trials, the difference between peaks is taken from the azonium bands marked with an asterisk.

Table 3.3.5: Wavelength maxima of dyes **11a-b**, **13a-c** and **15**

Parent Dye	λ_{max}	**Complexed Dye**	λ_{max}	$\Delta\lambda_{max}$
DMF				
9e	418	11a	436	+18
9f	414	11b	434	+20
9a	416	13a	421	+5
9b	501	13b	491	-10
9c	463	13c	452	-11
9e	418	15	441	+23
Ethanol				
9e	409	11a	423	+14
9f	407	11b	420	+17
9a	413	13a	414	+1
9b	487	13b	483	-4
9c	453	13c	452	-1
9e	409	15	423	+14
EtOH/HCl				
9e	357 ; 564*	11a	328 ; 540*	-24
9f	358 ; 567*	11b	324 ; 539*	-28
9a	318 ; 521* ; 541	13a	522* ; 544	+1
9b	326 ; 515* ; 534	13b	515* ; 538	0
9c	330 ; 522* ; 540	13c	522* ; 545	0
9e	357 ; 564*	15	340 ; 545*	-19

Compound **13a** in DMF did not display the same degree of shift in λ_{max} when compared to **13b-c**. This can be attributed to the lack of an electron-withdrawing group on the azo component. The coupling reaction of **9a** with **12**, which forms the complex, removes the hydroxyl group on the amino functionality, and creates an ester group. Thus the electron donating capability of the coupling component is reduced. This results in less electron migration and a corresponding hypsochromic shift of the absorption band, which is clearly observed for **13b** and **13c** in DMF (-10 nm, and -11 nm, respectively). The phenomenon is not as noticeable in ethanol due to the natural hypsochromic shift associated with less polar solvents, which results from a reduced stabilization of the excited state. The reason that **13a** does not show a hypsochromic

shift (indeed, a small bathochromic shift is observed) may be due to the lower degree of electron migration associated with **13a** when compared to **13b-c**. The lowered electron-donating ability of the coupling component has less of an effect in **13a** since it lacks an electron-withdrawing group in the azo component. This would necessarily result in less of a change, and the bathochromic shift itself may result from a steric interaction that is not observed in the other analogues.

Another interesting property of **13a** is the noticeable n-π^* band around 380 nm in DMF (Figure 3.3.6). Interestingly, since **9a** also displays the two peaks in DMF, the inclusion of the bimetallic complex did not inhibit this trait. The two peaks result from the lack of electron-withdrawing groups on **13a** which, should they be present, would cause a shift of the π-π^* band and thus overpower the n-π^* band. In fact, this is exactly what is observed for **13b-c**, with no n-π^* band being observed. The n-π^* band is only observed in DMF due to the greater ability of this solvent to stabilize the excited state, thus enhancing the separation of the two bands.

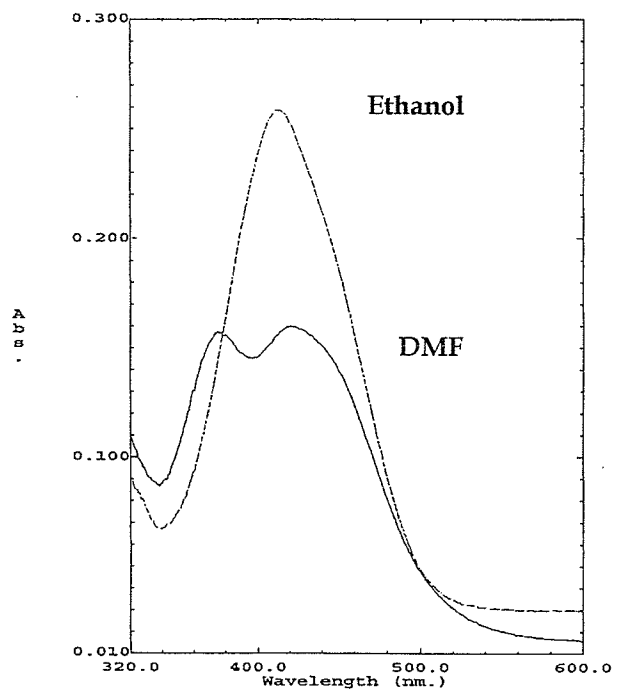

Figure 3.3.6: λ_{max} of **13a** in DMF and ethanol

As was evident with **13a-c**, the position of λ_{max} may change upon inclusion of a complexed arene. This effect greatly depends on the location of the complexed arene relative to the azo group. Altering the coupling component has shown to cause hypsochromic shifts, however, bathochromic shifts are observed when the complexed arene is near the azo component. Dyes **11a-b** and **15** display very interesting changes in their absorption bands when bonded to a complexed arene. The absorption maxima are observed to shift bathochromically, when the complexed dyes are compared to the starting dyes. Figure 3.3.7 illustrates this shift by comparing **11a** to the parent **9e** in ethanol. This effect can be attributed to the addition of the complexed arene to the dye structure. The inclusion of the complexed arene effectively removes an electron-donating OH group from the azo component and replaces it with an electron-withdrawing arene. While no direct conjugation occurs between the two aromatic rings

due to the ether linkage, the presence of the complexed arene is sufficient to enhance the electron migration from the coupling component to the azo bridge, thus resulting in a bathochromic shift.

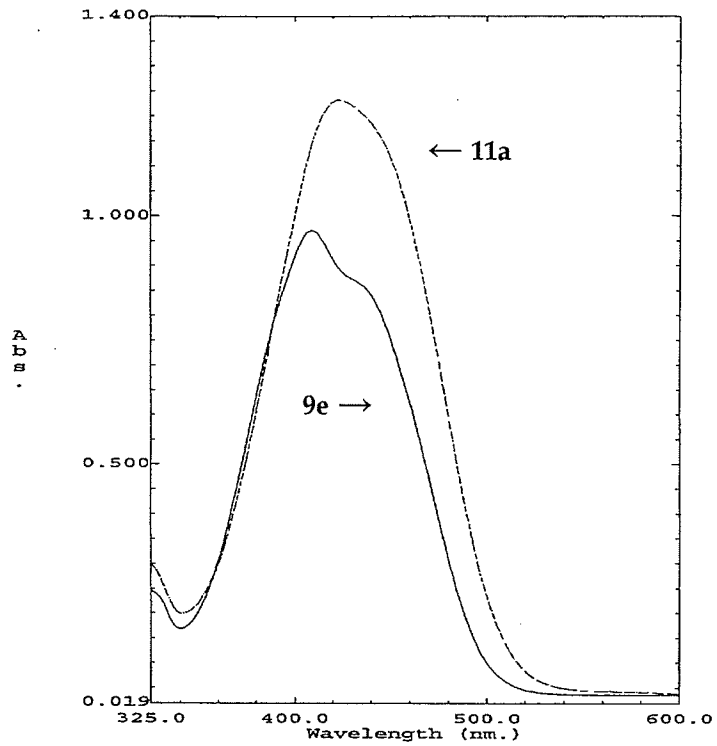

Figure 3.3.7: λ_{max} of **11a** and **9e** in ethanol

Overall, the dyes **11a-b** and **15** display the common characteristics of azo dyes. They exhibit solvent dependant absorption bands (Figure 3.3.8) and show significant changes with acidification. Indeed, the λ_{max} in acid aids in substantiating the influence of the complexed arene.

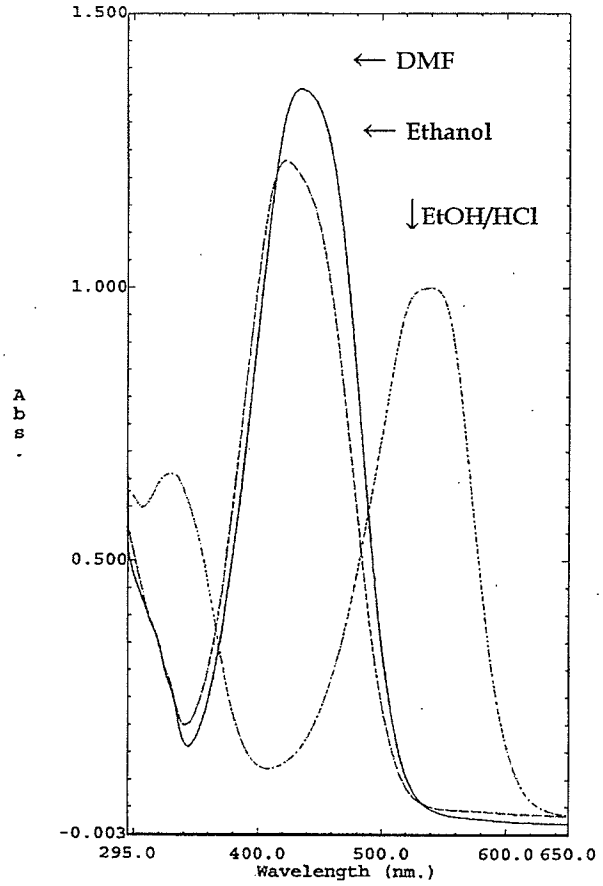

Figure 3.3.8: Solvent dependence of λ_{max} for **11a**

In acidified ethanol, complexed dyes **11a-b**, and **15** are observed to display hypsochromic shifts. This is to be expected, since under acidified conditions, the migration of electron density flows away from the azo bond and towards the amino nitrogen (Section 1.2.2, solvent effects). The presence of electron-withdrawing groups near, or attached to, the azo component (such as the complexed arene) will lessen this migration and thus increase the energy difference between the ground and excited states. Moreover, the lower degree of migration causes the β-nitrogen of the azo bond to have a greater basicity, thus it is preferentially protonated in acidic solution. This can be illustrated by examining the spectra of **11a** and **9e** in ethanol/HCl (Figure 3.3.9). The

parent dye, without a strong electron-withdrawing group in the azo component, displays two peaks, one attributed to the ammonium cation (357 nm) and one for the azonium cation (564 nm). The heights of these peaks are nearly identical. However, upon complexation, the spectrum changes to that of **11a**. This spectrum shows a distinct difference between the two bands, as the ammonium band is significantly smaller and less intense than the azonium band, as a result of the increased electron density on the azo bridge. Dyes **11b** and **15** display similar characteristics, with a nearly indistinguishable ammonium band observed for **11b**.

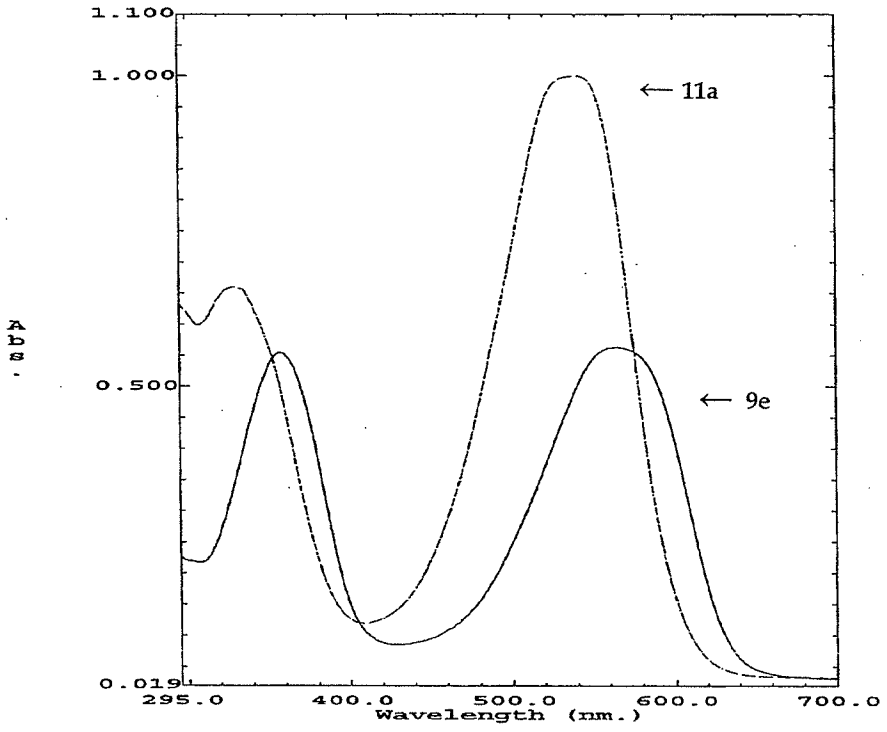

Figure 3.3.9: Absorption bands of **11a** and **9e** in ethanol/HCl

*ii) Reaction of **9g** with cyclopentadienyliron complexes*

The complexed dyes **17a-d** differed from previous dyes in that they were not aminoazobenzenes. Reaction of **9g** with complexed arenes in a 1:2 mmol ratio resulted in bimetallic structures that were 'capped' on either end. The dyes displayed interesting properties arising from the possible hydrazone tautomer present. Dyes containing an ortho hydroxy group have the ability to exist in the hydrazone form[135-137]. These dyes typically display an extremely low field (12-15 ppm) resonance in their ^{1}H spectra, arising from the N-H bond formed, and a carbonyl carbon resonance in the ^{13}C NMR[135]. Furthermore, due to the rapid exchange between the tautomers on the δ time scale, the NMR spectrum of the tautomers may display only one set of peaks, instead of the expected two sets of peaks that would arise from the azo and hydrazone forms[135]. Figure 3.3.10 shows the possible tautomeric pair that could exist for compound **9g**.

The uncertainty regarding which form is predominant, and whether equilibrium exists, for dye **9g** (and the complexed dyes synthezised from it, **17a-d**), originates from the presence of both a low field resonance (which would denote a N-H bond) and a slightly higher field resonance (which would denote a O-H bond), in addition to the lack of a carbonyl carbon in the ^{13}C NMR spectra. For example, dye **9g** displayed a strong resonance at 12.47 ppm, which implied a N-H bond[135]. However, no low field ^{13}C resonance was observed which would have implied the existence of a carbonyl carbon[135]. The spectra of the complexes (**17a-d**) displayed similar characteristics. The notable differences for dyes **17a-d** are noted in that there were two peaks downfield, which implied the presence of an N-H and a O-H bond. For example, dye **17c** displayed a peak at 9.65 ppm and at 13.05 ppm. The former peak may be attributed to the OH

group, however, the latter peak would imply the formation of a N-H bond. Figure 3.3.11 compares the ^{1}H NMR spectra of **9g** and **17c**. Interestingly, upon addition of D_2O, both low field resonances were observed to disappear, which implied that those resonances were indeed resulting from exchangeable hydrogens. Figure 3.3.12 and 3.3.13 presents the ^{1}H NMR spectra of **9g** and **17c** with the addition of D_2O. Despite the uncertainty regarding the azo-hydrazone tautomers, the dyes displayed the correct number of aromatic resonances in both ^{1}H and ^{13}C spectra and exhibited ^{1}H coupling constants and integrations which fell into expected values, thus leading to the conclusion that the dyes were successfully synthesized, regardless of which tautomer predominated.

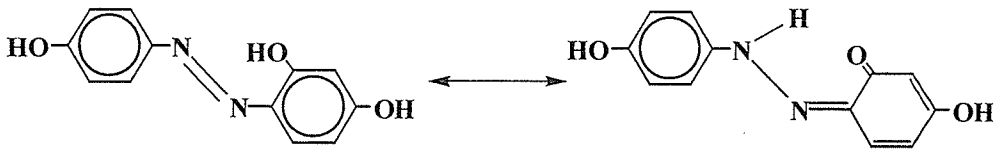

Figure 3.3.10: Tautomers of **9g**

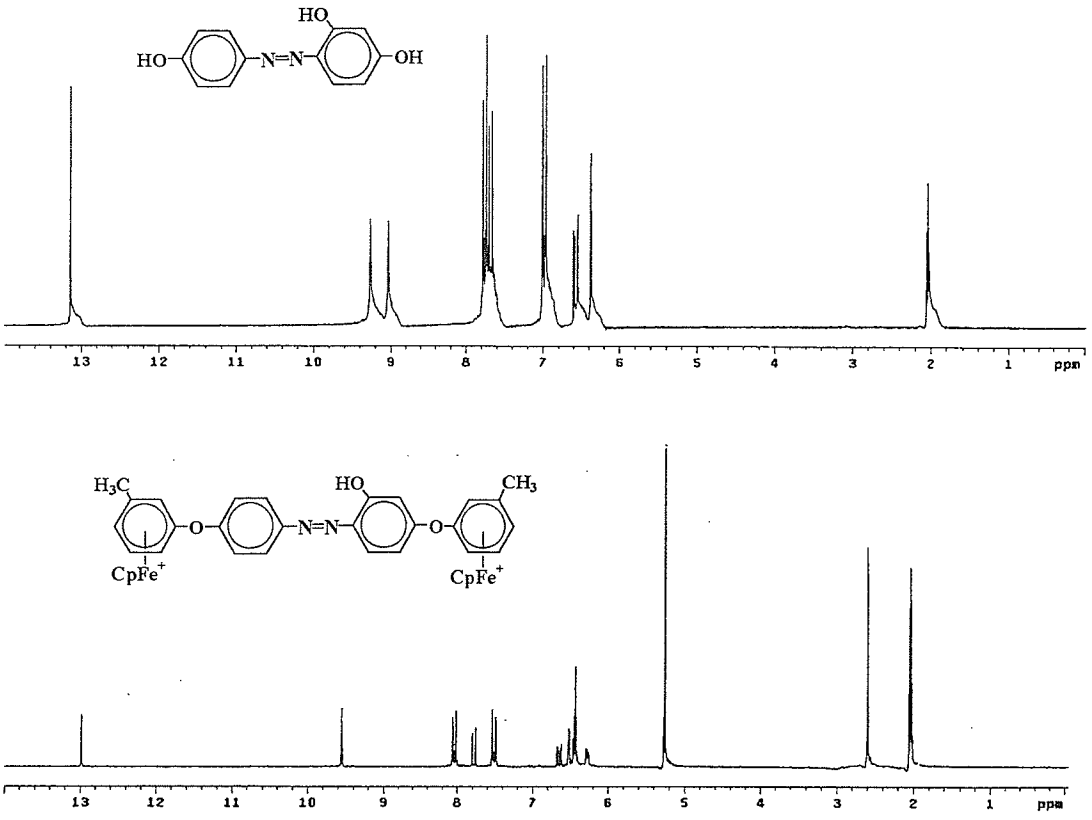

Figure 3.3.11: ^{1}H NMR spectra for **9g** (top) and **17c** (bottom)

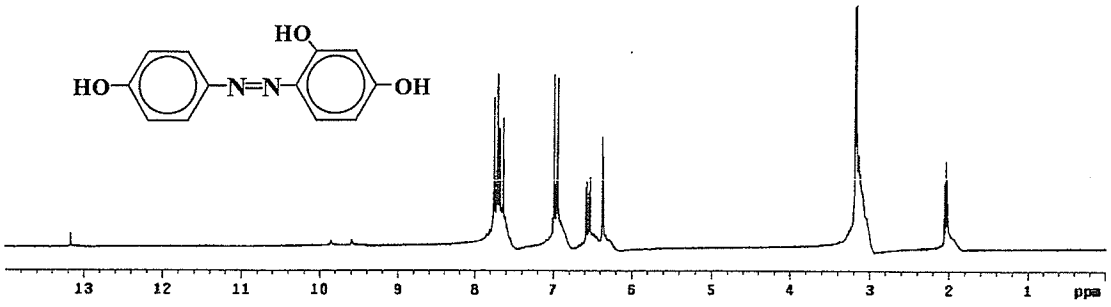

Figure 3.3.12: ^{1}H NMR spectra of **9g** with addition of D_2O

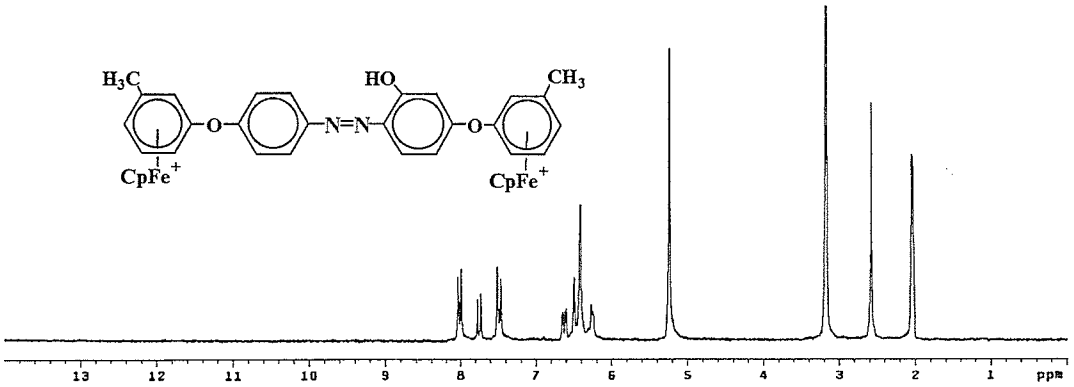

Figure 3.3.13: ^{1}H NMR of **17c** with addition of D_2O

The UV-Vis properties of dyes **17a-d** showed a slight bathochromic shift in DMF, corresponding to the presence of the complexed arene. Very little changes are observed otherwise. Table 3.3.6 lists the wavelength data in the solvents used. For the ethanol/HCl trials, the difference is taken between the bands marked with an asterisk. Upon acidification no ammonium band is observed, due to the lack of an amino group, and only a small azonium band around 490 nm arises. This is largely due to the hydrazone form that would inhibit protonation of the azo group. Figure 3.3.14 provides the spectrum of **17a** in acidified ethanol.

Table 3.3.6: λ_{max} of dyes **17a-d**

Parent Dye	λ_{max}	Complexed Dye	λ_{max}	$\Delta\lambda_{max}$
DMF				
9g	388	17a	391	+3
9g	388	17b	397	+9
9g	388	17c	398	+10
9g	388	17d	397	+9
Ethanol				
9g	385	17a	385	0
9g	385	17b	387	+2
9g	385	17c	387	+2
9g	385	17d	387	+2
EtOH/HCl				
9g	385 ; 498*	17a	383 ; 495*	-3
9g	385 ; 498*	17b	385 ; 496*	-2
9g	385 ; 498*	17c	385 ; 500*	+2
9g	385 ; 498*	17d	385 ; 496*	-2

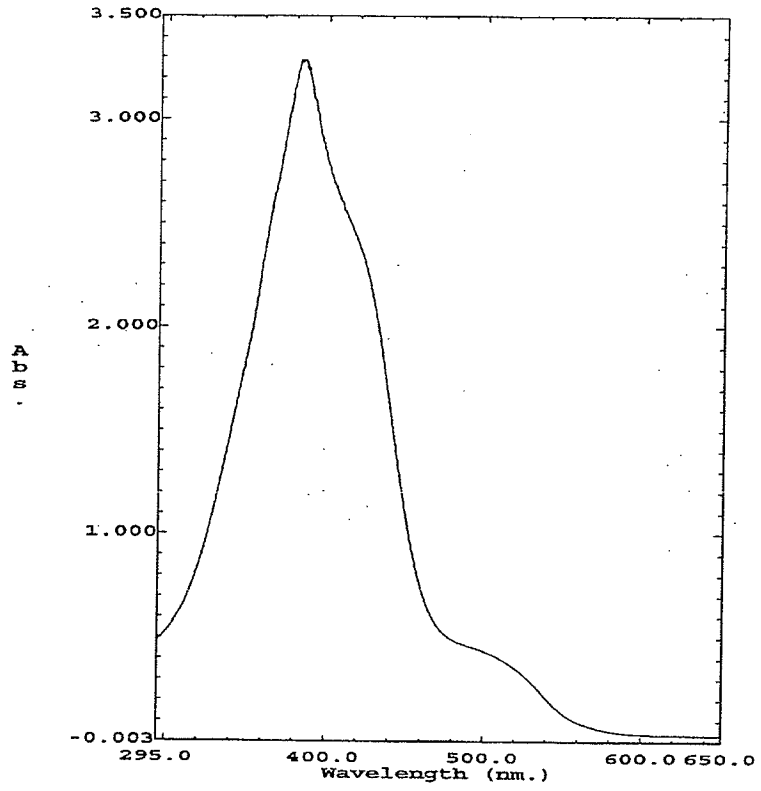

Figure 3.3.14: UV-Vis spectrum of **17a** in ethanol/HCl

iii) Thermogravimetric analysis

The TGA curves of the complexed dyes displayed characteristic losses of the metal moiety from the molecule between 200-230°C. The compounds then displayed a second, and typically, final weight loss between 440-500°C. Complexes **11a** and **13a** displayed final weight losses at higher temperatures. Due to the lower degree of substitution in these two complexes, the higher temperature associated with final decomposition may be attributed to the formation of lower molecular weight aromatic compounds that have higher thermal stabilities than their substituted analogues. Figure 3.3.15 provides the TGA curve of **13b** as an example.

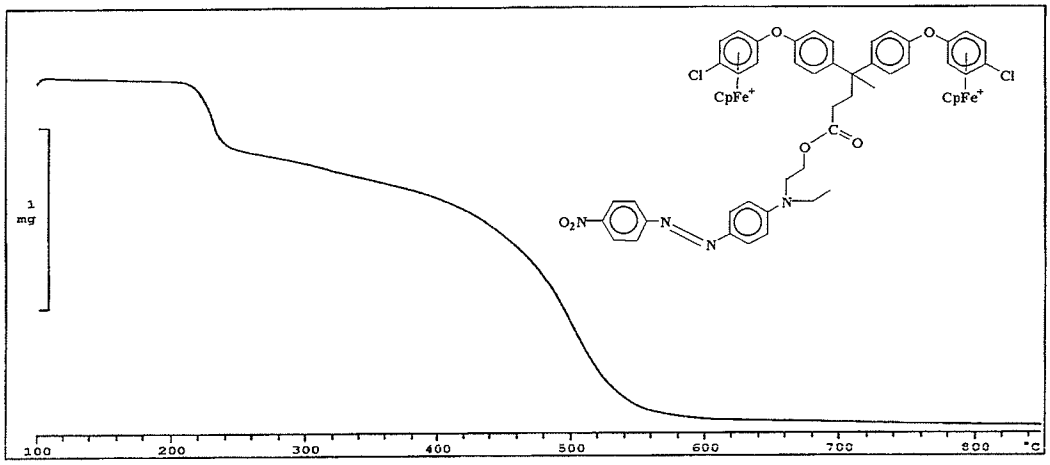

Figure 3.3.15: TGA curve of **13b**

Table 3.3.7: ^{1}H NMR data for complexed dyes **11a-b ; 13a-c and 15**

δ (ppm) in acetone-d_6				
	Aromatic H	**Complexed ArH**	**Cp**	**CH_2, CH_3**
11a	6.89 (d, 2H, J=9.0) 7.44 (d, 2H, J=8.6) 7.83 (d, 2H, J=9.0) 7.95 (d, 2H, J=9.0)	6.39 (s, 4H)	5.24 (s, 5H)	1.22 (t, 3H, J=7.0) CH_3 2.50 (s, 3H) CH_3 3.60 (t, 2H, J=4.0) CH_2 3.79 (q, 2H, J=5.4) CH_2 3.93 (t, 2H, J=5.4) CH_2
11b	7.45-7.48 (m, 2H) 7.51-7.53 (m, 2H) 8.07 (d, 2H, J=9.0) 8.15 (d, 2H, J=9.0)	6.41 (s, 4H)	5.24 (s, 5H)	2.52 (s, 3H) CH_3 3.50 (s, 3H) CH_3 3.90-3.97 (m, 4H) CH_2
13a	6.94 (d, 2H, J=9.0) 7.26 (d, 4H, J=9.0) 7.40-7.47 (m, 7H) 7.76 (d, 2H, J=7.0) 7.82 (d, 2H, J=9.4)	6.44 (d, 4H, J=6.6) 6.76 (d, 4H, J=6.7)	5.32 (s, 10H)	1.22 (t, 3H, J=7.0) CH_3 1.68 (s, 3H) CH_3 2.12-2.20 (m, 2H) CH_2 2.41-2.50 (m, 2H) CH_2 3.58 (q, 2H, J=7.4) CH_2 3.77 (t, 2H, J=5.5) CH_2 4.32 (t, 2H, J=5.5) CH_2
13b	6.99 (d, 2H, J=9.4) 7.27 (d, 4H, J=9.0) 7.39 (d, 4H, J=9.0) 7.89 (d, 2H, J=9.4) 8.34 (d, 2H, J=9.0)	6.46 (d, 4H, J=6.25) 6.78 (d, 4H, J=7.0)	5.35 (s, 10H)	1.24 (t, 3H, J=7.0) CH_3 1.68 (s, 3H) CH_3 2.10-2.19 (m, 2H) CH_2 2.37-2.49 (m, 2H) CH_2 3.58-3.69 (m, 2H) CH_2 3.78-3.86 (m, 2H) CH_2 4.30-4.39 (m, 2H) CH_2
13c	6.96 (d, 2H, J=9.0) 7.26 (d, 4H, J=8.6) 7.39 (d, 4H, J=9.0) 7.78-7.89 (m, 4H) 8.09 (d, 2H, J=8.6)	6.47 (d, 4H, J=6.3) 6.74 (d, 4H, J=6.6)	5.32 (s, 10H)	1.67 (s, 3H) CH_3 1.23 (t, 3H, J=7.1) CH_3 2.09-2.21 (m, 2H) CH_2 2.39-2.51 (m, 2H) CH_2 2.61 (s, 3H) CH_3 3.48-3.62 (m, 2H) CH_2 3.79 (t, 2H, J=5.6) CH_2 4.33 (t, 2H, J=5.6) CH_2
15	6.96 (d, 4H, J=8.6) 7.46 (d, 4H, J=8.6) 7.86 (d, 4H, J=9.0) 7.96 (d, 4H, J=8.6)	6.39 (s, 4H)	5.41 (s, 5H)	1.15-1.27 (m, 6H) CH_3 3.58-3.65 (m, 4H) CH_2 3.68-3.82 (m, 4H) CH_2 3.92-4.09 (m, 4H) CH_2

Coupling constants calculated in Hz

Table 3.3.8: ^{13}C NMR data for complexed dyes **11a-b ; 13a-c** and **15**

δ (ppm) in acetone-d_6								
	quat ArC	**ArCH**	**Comp. quat**	**Comp. ArCH**	**Cp**	**CH_2**	**CH_3**	**Others**
11a	132.49 154.87	122.10 123.95 127.89	101.61	77.44 87.69	78.45	55.60 59.53 65.89	12.11 19.73	------
11b	132.52 154.77	118.70 122.39 122.94	101.79	77.68 87.83	78.58	58.40 59.03	19.83 42.50	------
13a	143.98 147.83 151.73 152.00	112.30 121.22 125.88 129.91 130.39 130.57	104.82 133.80	77.04 87.79	80.40	30.73 37.09 46.22 48.99 62.42	12.31 27.76	45.42* 173.53*
13b	144.17 147.82 148.17 151.94 152.95 157.41	112.55 121.22 123.30 125.54 127.04 130.56	104.78 133.80	76.99 87.75	80.39	30.69 37.06 46.19 49.08 62.28	12.34 27.75	45.70* 173.53*
13c	137.91 144.08 147.78 151.85 152.31 156.30	112.36 121.17 122.69 126.47 130.12 130.50	104.70 133.87	76.85 87.66	80.31	30.67 37.02 46.16 48.96 62.29	12.31 26.83 27.72	45.50* 173.50* 197.34*
15	142.52 150.49 151.06 154.44	111.80 121.44 124.21 125.58	130.20	75.90	78.45	45.64 52.64 58.70	12.39	------

*quaternary carbon

Table 3.3.9: ^{1}H NMR data for complexed dyes **17a-d**

δ (ppm) in acetone-d_6					
	Aromatic H	**Comp. ArH & Aromatic H (overlapped)**	**Cp**	**CH_3**	**Others**
17a	6.58 (dd, 1H, J=8.5 ,2.4) 7.51 (d, 2H, J=8.7) 7.76 (d, 1H, J=9.0) 8.02 (d, 2H, J=9.0)	6.38-6.44 (m, 9H) 6.49-6.54 (m, 2H)	5.29 (s, 10H)	------	13.18 (s, 1H)
17b	6.65 (dd, 1H, J=8.8, 2.6) 7.51 (d, 2H, J=8.6) 7.78 (d, 1H, J=9.0) 8.04 (d, 2H, J=8.6)	6.40-6.49 (s, 9H)	5.28 (s, 10H)	2.53 (s, 6H)	9.56 (s, 1H) 12.99 (s, 1H)
17c	6.65 (dd, 1H, J=8.7, 2.6) 7.51 (d, 2H, J=8.6) 7.78 (d, 1H, J=8.5) 8.03 (d, 2H, J=8.2)	6.23-6.31 (m, 2H) 6.39-6.49 (m, 5H) 6.50-6.58 (s, 2H)	5.24 (s, 10H)	2.59 (s, 6H)	9.65 (s, 1H) 13.05 (s, 1H)
17d	6.65 (d, 1H, J=8.9) 7.48 (d, 2H, J=8.3) 7.76 (d, 1H, J=8.3) 8.01 (d, 2H, J=8.3)	6.30-6.50 (m, 7H)	5.18 (s, 10H)	2.51 (s, 6H) 2.59 (s, 6H)	9.53 (s, 1H) 13.01 (s, 1H)

Coupling constants calculated in Hz

Table 3.3.10: ^{13}C NMR data for complexed dyes **17a-d**

δ (ppm) in acetone-d_6						
	quat ArC	**ArCH**	**Comp. quat**	**Comp. ArCH**	**Cp**	**CH_3**
17a	135.45 144.78 156.29 160.73 162.53	103.94 109.31 116.87 124.22 134.60	132.96	79.10 86.03 87.84	78.19	------
17b	133.46 149.45 155.81 156.90 163.88	104.01 110.09 122.31 124.67 135.42	101.93 132.72	77.82 87.97	78.69	19.90
17c	135.44 149.49 155.72 156.87 163.87	104.01 110.07 122.42 124.66 133.45	103.72 133.50	76.78 79.54 86.52 87.04	78.69	20.44
17d	133.43 149.43 155.88 156.92 164.09	104.00 110.17 122.24 124.63 135.42	100.60 102.25 132.35	76.44 79.66 88.06	78.89	18.29 18.95

Table 3.3.11: Yield, IR and TGA data for compounds **11a-b ; 13a-c ; 15 ; 17 a-d**

	%Yield	IR (cm^{-1})	TGA_{onset} (°C)	TGA_{endset} (°C)	$TGA_{midpoint}$ (°C)	% Weight loss
11a	87	3469 (OH) 841 (PF_6^-)	216 568	264 629	249 581	25 37
11b	90	3407 (OH) 841 (PF_6^-)	231 446	286 462	259 459	31 4
13a	92	1729 (C=O) 843 (PF_6^-)	220 410 545	237 456 592	244 432 568	22 22 10
13b	90	1731 (C=O) 843 (PF_6^-)	223 468	238 539	231 497	19 58
13c	87	1736 (C=O) 1677 (C=O) 843 (PF_6^-)	223 363	246 390	236 381	19 14
15	85	3427 (OH) 844 (PF_6^-)	220 404	233 472	230 435	11 25
17a	89	3428 (OH) 843 (PF_6^-)	203 442	224 467	219 468	10 8
17b	92	3435 (OH) 843 (PF_6^-)	217 470	240 481	236 464	16 7
17c	90	3489 (OH) 843 (PF_6^-)	218 485	262 563	244 515	18 14
17d	91	3510 (OH) 843 (PF_6^-)	203 442	224 467	219 468	10 8

3.3.3 Polymerization of complexed dyes 13a-c

The structures of **13a-c**, containing terminal complexed arenes, allowed a metal-mediated nucleophilic aromatic substitution polymerization to occur. Reaction with one of three dinucleophiles (**18a-c**) produced a series of highly coloured polymers that contained the azo chromophore as a side chain pendant to the backbone (**19a-i**). Scheme 3.3.6 illustrates the polymerization reaction.

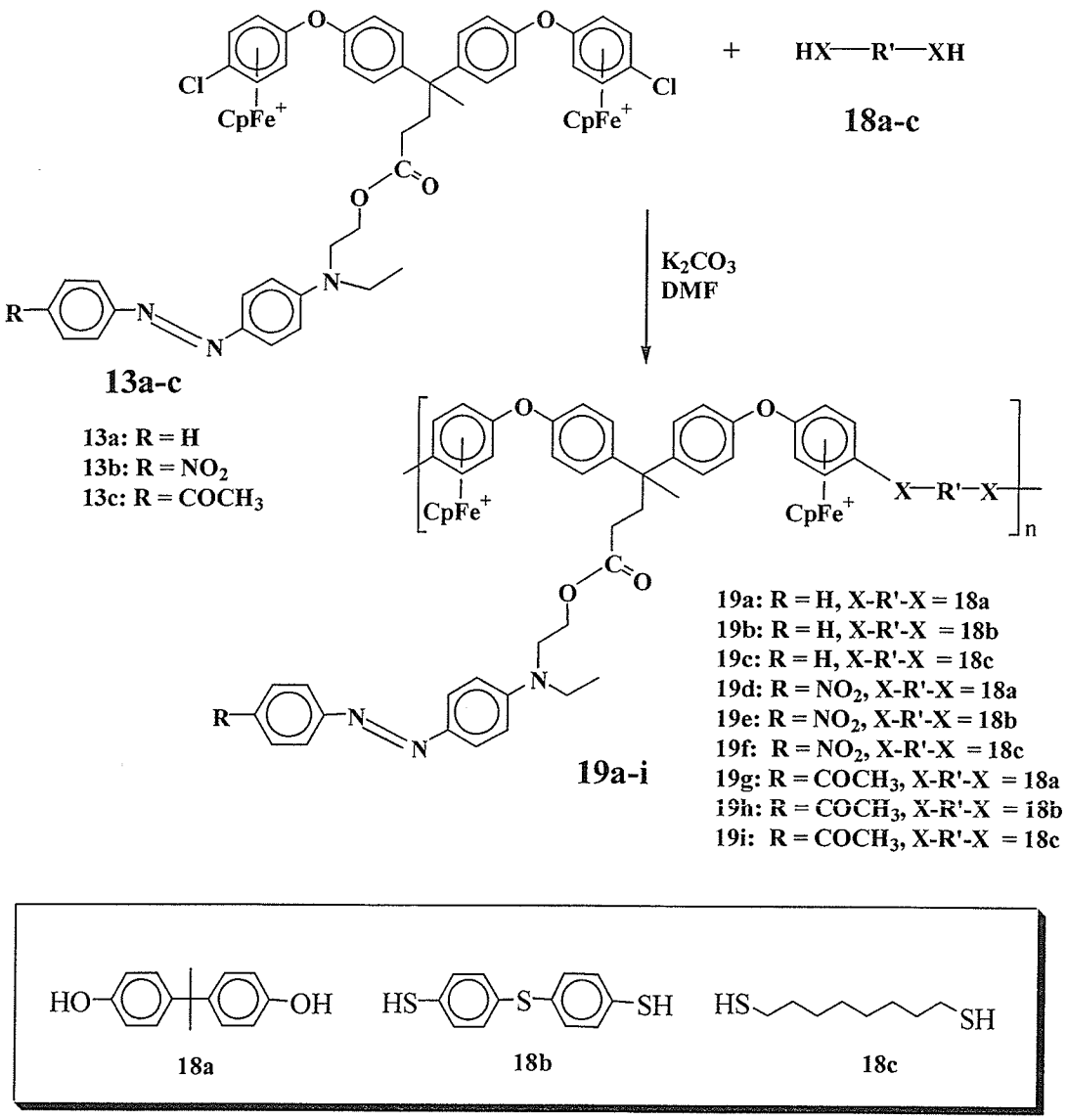

Scheme 3.3.6

Polymerization was confirmed via ^{1}H and ^{13}C NMR spectrometry. Polymers **19c,f,h,i** were highly insoluble in organic solvents, thus it was not possible to record their ^{13}C NMR spectra. The ^{1}H spectra of **13a** and **19a** are compared in Figure 3.3.16. Isolation of the polymeric material can be confirmed by observing the presence of a broad singlet around 6.2 ppm in the polymer spectrum (representing the complexed aromatic protons), instead of the two doublets between 6.0-6.8 ppm (in **13a**). The Cp peak is also shifted upfield, from 5.32 ppm (**13a**) to 5.18 ppm (**19a**), which is indicative of polymerization[16]. Additionally, all the peaks were observed to broaden, due to the increase in molecular weight. Further analyses were performed using UV, IR and TGA techniques (Table 3.3.12 – 3.3.16). The thermal properties of the polymers mirrored those of the starting monomers.

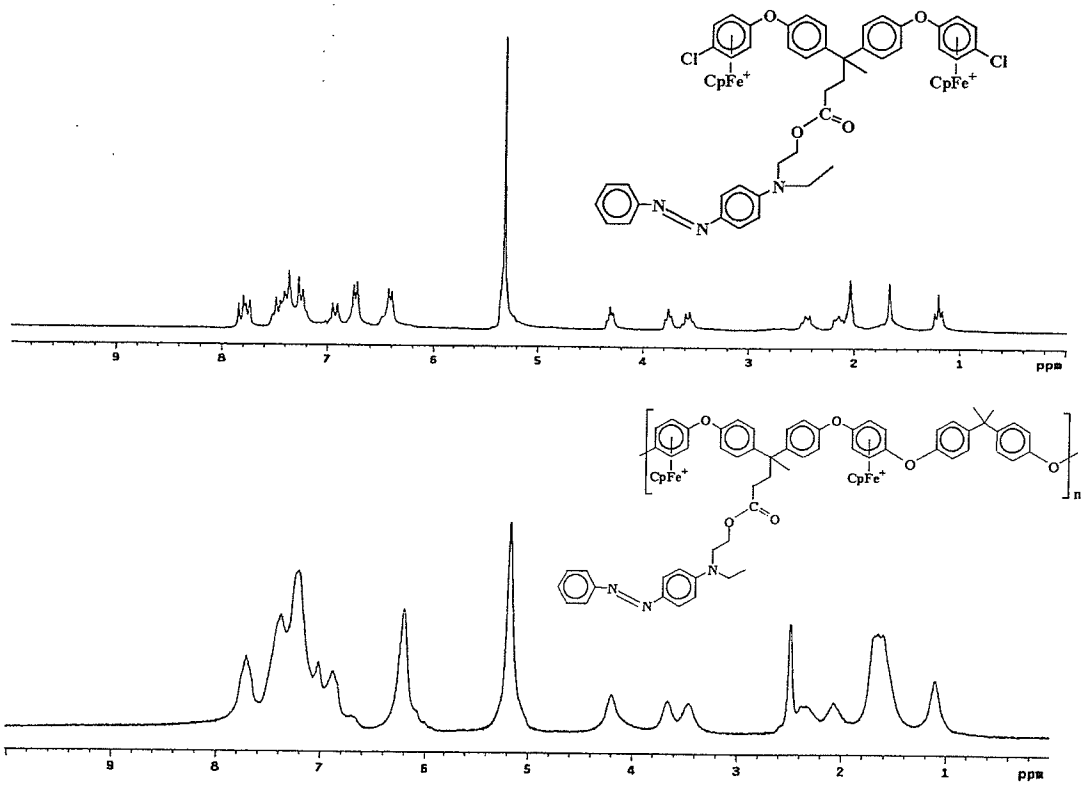

Figure 3.3.16: ^{1}H NMR spectra of **13a** (top) and **19a** (bottom)

The UV-Vis properties of the complexed polymers were not observed to change to any significant extent when compared to the complexed monomers. In DMF, bathochromic or hypsochromic shifts were smallest between the complexed polymers and monomers, while larger changes were observed when the λ_{max} values were compared to the original parent dyes (**9a-c**). For example, the nitro-substituted polymers (**19d-f**) displayed similar hypsochromic shifts (-11nm, –10nm and -10nm, respectively) from the parent dye as the monomer itself (**13b**, -10nm). This indicates that initial complexation of the azo dye, and not polymer formation, was largely responsible for the observed hypsochromic shift. This is further substantiated by the fact that polymers **19a-c** displayed the n-π^* transition, in addition to the π-π^* transition, whereas the NO_2 and $COCH_3$ analogues did not. Table 3.3.12 provides the λ_{max} and $\Delta\lambda_{max}$ shifts between complexed polymer, monomer and parent dyes.

Table 3.3.12: Wavelength maxima for polymers **19a-i**

Parent Dye (9*x*)	λ_{max} (nm)	13*x*	λ_{max} (nm)	$CpFe^+$ Polymer	λ_{max} (nm)	$\Delta\lambda_{max}$ from 9*x*	$\Delta\lambda_{max}$ from 13*x*
DMF							
9a	416	13a	421	19a	420	+4	-1
9a	416	13a	421	19b	418	+2	-3
9a	416	13a	421	19c	419	+3	-2
9b	501	13b	491	19d	490	-11	-1
9b	501	13b	491	19e	491	-10	0
9b	501	13b	491	19f	491	-10	0
9c	463	13c	452	19g	453	-10	+1
9c	463	13c	452	19h	454	-9	+2
9c	463	13c	452	19i	452	-11	0
Ethanol							
9a	413	13a	414	19a	414	+1	0
9a	413	13a	414	19b	418	+5	+4
9a	413	13a	414	19c	415	+2	+1
9b	487	13b	483	19d	479	-8	-4
9b	487	13b	483	19e	482	-5	-1
9b	487	13b	483	19f	482	-5	-1
9c	453	13c	452	19g	452	-1	0
9c	453	13c	452	19h	449	-4	-3
9c	453	13c	452	19i	451	-2	-1
Ethanol /HCl							
9a	521 ; 541	13a	522* ; 544	19a	520*; 545	0	-2
9a	521 ; 541	13a	522* ; 544	19b	527*; 550	+6	+5
9a	521 ; 541	13a	522* ; 544	19c	521*; 547	0	-1
9b	515 ; 534	13b	515* ; 538	19d	515*; 540	0	0
9b	515 ; 534	13b	515* ; 538	19e	517*; 540	+2	+2
9b	515 ; 534	13b	515* ; 538	19f	515* ; 540	0	0
9c	522 ; 540	13c	522* ; 545	19g	521* ; 549	-1	-1
9c	522 ; 540	13c	522* : 545	19h	518* ; 549	-4	-4
9c	522 ; 540	13c	522* ; 545	19i	522* ; 549	0	0

The molecular weights of the polymers were determined by gel permeation chromatography (GPC). Due to the interactions of the cationic organoiron moiety with the stationary phase of GPC columns, the polymers were decomplexed prior to analysis (Section 3.3.4). The corresponding molecular weights of the complexed polymers were

calculated based on the number of repeating units in the decomplexed samples. Table 3.3.13 provides the data.

Table 3.3.13: Molecular Weights and Polydispersity indices of polymers **19a-i** and their decomplexed analogues.

Polymer	Complexed Mw	Decomplexed Mw	PDI
19a	18 200	11 500	1.43
19b	15 100	9 800	1.41
19c	14 100	8 800	1.22
19d	17 400	11 200	2.04
19e	17 400	11 300	2.64
19f	13 400	8 400	1.29
19g	13 400	8 600	1.16
19h	31 600	20 500	1.18
19i	15 300	9 600	1.20

Table 3.3.14: ^{1}H NMR data for polymers **19a-i**

δ (ppm) in dimethylsulphoxide-d_6					
	Aromatic H	**Comp. ArH**	**Cp**	**CH_2**	**Others**
19a	6.80-6.89 (m, 4H) 6.97-7.09 (s, 5H) 7.14-7.25 (m, 8H) 7.36-7.48 (m, 4H) 7.58-7.75 (m, 4H)	6.21 (s, 8H)	5.18 (s, 10H)	1.95-2.07 (s, 2H) 2.25-2.40 (m, 2H) 3.39-3.48 (s, 2H) 3.65-3.82 (m, 2H) 4.21 (s, 2H)	1.12 (s, 3H) CH_3 1.64-1.78 (m, 12H) CH_3
19b	6.88 (d, 2H, J=9.0) 7.21-7.32 (m, 8H) 7.40-7.52 (m, 8H) 7.58-7.68 (m, 7H)	6.26 (s, 8H)	5.14 (s, 10H)	2.07 (s, 2H) 2.29-2.43 (m, 2H) 3.54-3.55 (m, 2H) 3.66 (br s, 2H) 4.22 (br s, 2H)	0.97-1.21 (m, 3H) CH_3 1.59 (s, 3H) CH_3
19c	6.80-6.92 (m, 4H) 7.15-7.25 (m, 4H) 7.38-7.48 (m, 4H) 7.61-7.75 (m, 4H)	6.23 (s, 4H) 6.35 (s, 4H)	5.08 (s, 10H)	1.98-2.13 (m, 2H) 2.38-2.53 (m, 2H) 3.08-3.23 (m, 2H) 3.58-3.69 (m, 2H) 4.05-4.19 (m, 2H)	0.99-1.15 (m, 3H) CH_3 1.25-1.38 (m, 8H) CH_3 and CH_2 1.50-1.65 (m, 11H) CH_3 and CH_2
19d	6.91 (d, 2H, J=9.6) 7.18-7.30 (m, 4H) 7.37-7.45 (m, 12H) 7.83-7.93 (m, 4H) 8.32 (d, 2H, J=9.4)	6.21 (s, 8H)	5.18 (s, 10H)	1.97-2.15 (m, 2H) 2.22-2.36 (m, 2H) 3.48-3.57 (m, 2H) 3.55-3.70 (m, 2H) 4.18-4.29 (m, 2H)	1.01-1.18 (m, 3H) CH_3 1.50 (s, 6H) CH_3 1.65 (s, 3H) CH_3
19e	6.90 (d, 2H, J=9.4) 7.13-7.25 (m, 4H) 7.45 (d, 4H J=7.4) 7.53-7.68 (m, 4H) 7.71-7.85 (m, 4H) 8.30 (d, 2H, J=9.0)	6.28 (s, 8H)	5.15 (s, 10H)	1.97-2.15 (m, 2H) 2.27-2.39 (m, 2H) 3.37-3.53 (m, 2H) 4.13-4.26 (m, 2H)	0.96-1.12 (m,3H) CH_3 1.60 (s, 3H) CH_3
19f	6.84-6.97 (m, 2H) 7.25-7.39 (m, 4H) 7.79-7.86 (m, 4H) 7.91-8.01 (m, 4H) 8.12-8.30 (m, 2H)	6.14-6.26 (m, 4H) 6.26-6.38 (m, 4H)	5.09 (s,10H)	1.27-1.39 (m, 8H) 2.00-2.15 (m, 2H) 2.30-2.45 (m, 2H) 3.45-3.49 (m, 2H) 3.62-3.78 (m, 2H) 4.19-4.27 (m, 2H)	0.96-1.20 (m, 3H) CH_3 1.45-1.63 (m, 11H) CH_3 and CH_2
19g	6.81-7.28 (m, 19H) 7.63-7.69 (m, 4H) 7.90-7.99 (m, 2H)	6.11 (s, 8H)	5.08 (s, 10H)	1.95-2.03 (m, 2H) 2.30 (br s, 2H) 3.28-3.45 (m, 2H) 3.51-3.60 (m, 2H) 4.10-4.19 (m, 2H)	0.98-1.11 (m, 3H) CH_3 1.41-1.82 (m, 9H) CH_3 2.40 (s, 3H) CH_3

Coupling constants calculated in Hz

Table 3.3.14: ^{1}H NMR data for polymers **19a-i** continued

19h	6.80-6.90 (m, 2H) 7.13-7.80 (m, 18H) 7.95-8.05 (m, 4H)	6.26 (s, 8H)	5.15 (s, 10H)	1.57-1.68 (m, 2H) 2.01-2.17 (m, 2H) 3.28-3.36 (m, 2H) 3.69-3.75 (m, 2H) 4.15-4.21 (m, 2H)	1.08-1.12 (m, 3H) CH_3 1.65 (s, 3H) CH_3 2.72 (s, 3H) CH_3
19i	6.73-6.85 (m, 2H) 7.04-7.22 (m, 8H) 7.60-7.68 (m, 4H) 7.90-7.99 (m, 2H)	6.09-6.37 (m 8H)	4.97 (s, 10H)	1.18-1.35 (m, 8H) 1.40-1.53 (m, 8H) 1.94-2.09 (m, 8H) 3.31-3.45 (m, 2H) 4.03-4.21 (m, 2H)	0.97-1.15 (m, 3H) CH_3 2.19-3.10 (br m, 8H) CH_3 and CH_2

Coupling constants calculated in Hz

Table 3.3.15: ^{13}C NMR data for soluble polymers **19a,b,d,e,g**

δ (ppm) in dimethylsulphoxide-d_6								
	quat ArC	**ArCH**	**Comp. quat**	**Comp. ArCH**	**Cp**	**CH_2**	**CH_3**	**Others**
19a	142.54 146.04 147.94 151.47 151.67 152.48 155.36	111.61 114.98 117.73 120.13 121.90 125.18 127.58 128.94 129.40	130.12 130.34	77.27 75.09	78.05	30.11 44.85 48.13 61.74	12.17 27.19 30.78	42.39* 45.12* 172.89*
19b	136.70 142.69 146.42 150.91 151.30 152.59	111.79 120.51 122.51 125.39 129.54 129.89 132.39 135.16	103.59 132.10	76.52 78.15 85.42	79.00	30.22 44.81 48.28 61.95	12.32 27.29	45.33* 173.06*
19d	143.05 146.20 147.15 148.09 151.63 151.83 152.16 156.41	112.03 115.13 120.29 122.31 125.31 126.45 127.72 129.50	130.49 130.27	77.41 75.34	78.22	30.15 44.96 48.36 61.90	12.342 27.20 30.94	42.56* 45.29* 173.05*
19e	136.66 143.08 146.36 147.10 151.29 152.13 156.34	111.99 120.54 122.72 125.23 126.49 129.52 135.17	103.61 132.03	76.50 78.12 85.37	79.00	30.23 44.94 48.35 61.89	12.32 27.2	45.29* 173.01*
19g	136.40 142.37 145.67 147.55 151.05 151.26 154.72	111.32 117.32 119.73 121.54 125.40 128.55 128.96 129.26	129.74 129.95	74.63 76.84	77.62	29.59 44.38 47.38 61.28	11.73 26.62 30.35	41.92* 44.67* 172.51* 196.92*

* quaternary carbon

Table 3.3.16: Yield, IR and TGA data for compounds **19a-i**

	Yield	IR (cm^{-1})	TGA_{onset} (°C)	TGA_{endset} (°C)	$TGA_{midpoint}$ (°C)	% Weight loss
19a	95	1727 (C=O) 842 (PF_6^-)	225 510	248 526	242 516	9 28
19b	93	1729 (C=O) 843 (PF_6^-)	212 398	233 470	225 428	8 33
19c	92	1731 (C=O) 842 (PF_6^-)	208 402	229 442	223 423	3 24
19d	97	1730 (C=O) 844 (PF_6^-)	227 397 572	243 454 613	237 421 590	7 29 27
19e	97	1729 (C=O) 843 (PF_6^-)	225 469	245 500	236 485	13 13
19f	94	1733 (C=O) 844 (PF_6^-)	211 405 489	237 435 502	225 494 469	13 14 13
19g	89	1736 (C=O) 1677 (C=O) 843 (PF_6^-)	223 501	244 555	241 530	4 26
19h	90	1731 (C=O) 1674 (C=O) 844 (PF_6^-)	221 425	253 472	238 466	16 16
19i	95	1736 (C=O) 1676 (C=O) 842 (PF_6^-)	209 413	248 491	232 452	16 29

3.3.4 Decomplexation of azo dyes

*i) Decomplexation of dyes **11a-b, 13a-c, 15, 17a-d***

Photolytic demetallation of the complexed azo dyes in a mixture of acetonitrile/dichloromethane liberated the organic analogues. The demetallation reactions are presented in Schemes 3.3.7-3.3.10. The pure organic dyes were characterized in the same manner as the complexed versions. The ^{1}H and ^{13}C NMR data for compounds **20a-b**, **21a-c**, **22**, and **23a-d** are presented in Tables 3.3.19-3.3.22.

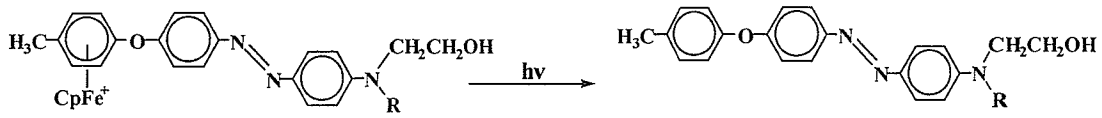

11a-b

11a: R = CH_2CH_3
11b: R = CH_3

20a-b

20a: R = CH_2CH_3
20b: R = CH_3

Scheme 3.3.7

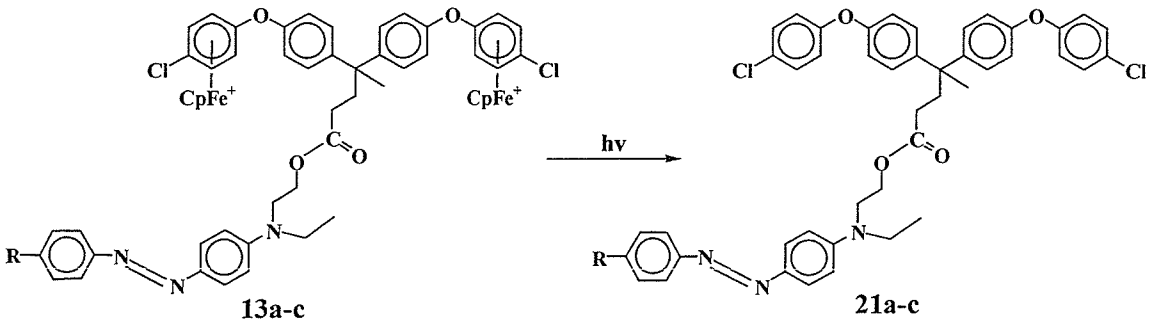

13a-c

13a: R = H
13b: R = NO_2
13c: R = $COCH_3$

21a-c

21a: R = H
21b: R = NO_2
21c: R = $COCH_3$

Scheme 3.3.8

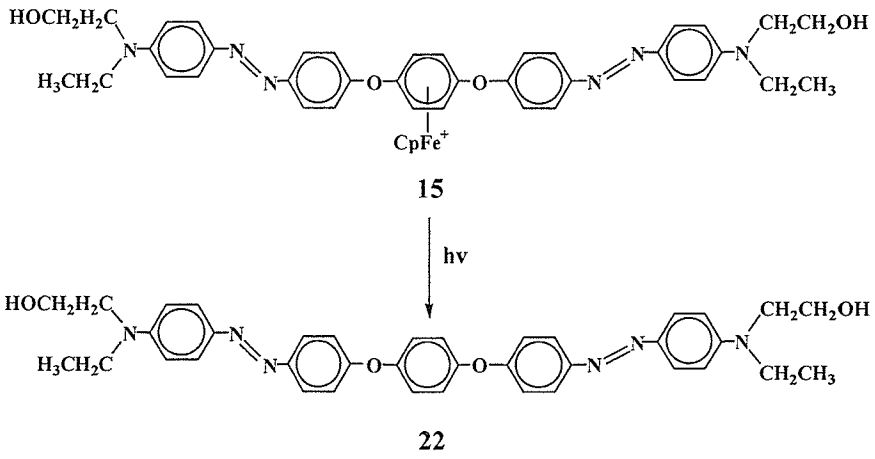

Scheme 3.3.9

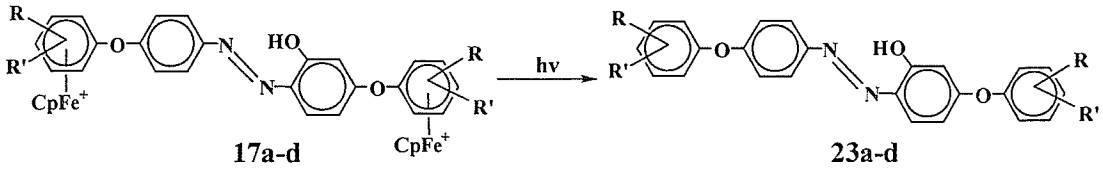

17a: R = R' = H
17b: R = *p*-CH_3, R' = H
17c: R = *m*-CH_3, R' = H
17d: R = *p*-CH_3 R'= *m*-CH_3

23a: R = R' = H
23b: R = *p*-CH_3, R' = H
23c: R = *m*-CH_3, R' = H
23d: R = *p*-CH_3 R'= *m*-CH_3

Scheme 3.3.10

Upon decomplexation, the dyes were observed to lose the Cp resonance from the NMR spectra, with a concomitant downfield shift of the complexed aromatic protons. Figure 3.3.17 and 3.3.18 presents the ^{1}H and ^{13}C NMR spectra of **23d**. Similar to its complexed analogue, there exist two peaks due to the possible tautomers. The peak at 13.10 ppm implied a H bonded to nitrogen, while the 9.37 ppm peak implied a H bonded to oxygen. The aromatic region shows a series of doublets indicative of the structure, and the aromatic protons on the coupling component are clearly visible with the removal of the complexed aromatic protons. The ^{13}C NMR spectrum displays eight quaternary

aromatic carbons, with the 162.91 ppm and 160.81 ppm signals representing the carbons bonded to the ether oxygens on the coupling component and azo component, respectively.

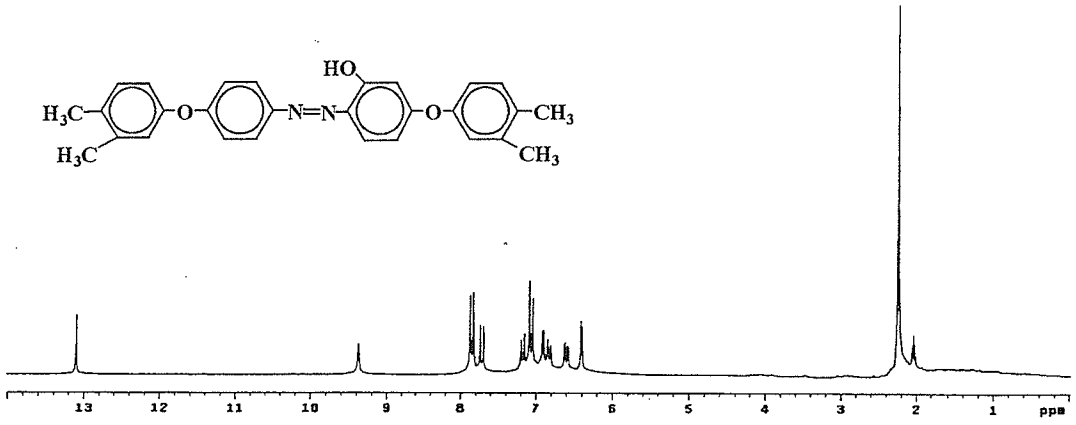

Figure 3.3.17: ^{1}H NMR spectrum of **23d**

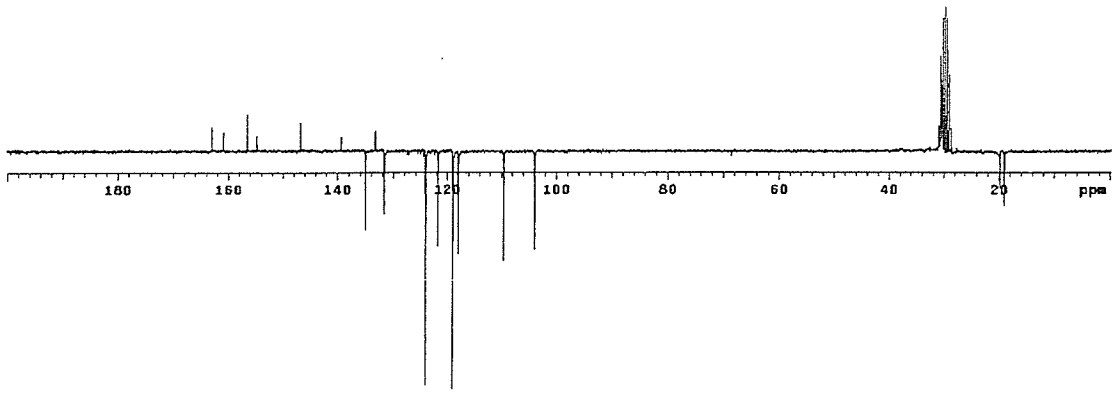

Figure 3.3.18: ^{13}C NMR spectrum of **23d**

Decomplexation of the dyes reduced the degree of shift of λ_{max} from the parent dye. Table 3.3.17 provides the λ_{max} values for the dyes and the degree of shift from the complexed analogue and parent. On examination of the shifts in wavelength, it is evident that a general shift towards the parent occurs. This can be attributed to the removal of the electron-withdrawing cyclopentadienyliron moiety. One of the greatest effects of removal of the iron moiety is observed with compound **22**, which displays a 13 nm shift away from the complexed form. Being a disazo compound, this result is not surprising, as the electron-withdrawing power of the $CpFe^+$ moiety was affecting two azo groups.

In addition, the removal of the iron centers returned the absorption profile in acidified ethanol of **20a-b** and **22** closer to the original dye. Examination of the spectra of **20a** in acidified ethanol reveals the presence of a significant ammonium band (Figure 3.3.19). As previously explained, the presence of the $CpFe^+$ complexed arene increased the basicity of the azo group. Removing the iron moiety lowered the electron density on the azo group and therefore increased the degree of protonation at the amino group. Figure 3.3.20 provides the UV-Vis spectra of **9f**, **11b** and **20b** (parent, complexed and decomplexed, respectively). As can be seen, the complexed form displays the lowest ammonium band, while the decomplexed form returns the band closer to the original value.

Table 3.3.17: Wavelength maxima of decomplexed dyes **20a-b**, **21a-c**, **22**, **23a-d**, and degree of shift from the parent and complexed analogues.

Parent Dye	Comp. Dye:	Decomplexed Dye	λ_{max} (nm)	$\Delta\lambda_{max}$ from complexed	$\Delta\lambda_{max}$ from 9x
DMF					
9e	11a	20a	425	-11	+7
9f	11b	20b	421	-13	+7
9a	13a	21a	419	+2	+3
9b	13b	21b	490	-1	-11
9c	13c	21c	454	+2	-9
9e	15	22	428	-13	+10
9g	17a	23a	387	-4	-1
9g	17b	23b	393	-4	+5
9g	17c	23c	388	-10	0
9g	17d	23d	392	-5	+4
Ethanol					
9e	11a	20a	415	-8	+6
9f	11b	20b	412	-8	+9
9a	13a	21a	410	-4	-3
9b	13b	21b	479	-4	-8
9c	13c	21c	447	-5	-6
9e	15	22	415	-8	+6
9g	17a	23a	385	0	0
9g	17b	23b	387	0	+2
9g	17c	23c	387	0	+2
9g	17d	23d	387	0	+2
EtOH /HCl					
9e	11a	20a	351 ; 551*	+11	-13
9f	11b	20b	351 ; 547*	+8	-20
9a	13a	21a	524* ; 544	+2	+3
9b	13b	21b	515* ; 537	0	0
9c	13c	21c	521* ; 545	-1	-1
9e	15	22	348 ; 548*	+3	-16
9g	17a	23a	385 ; 498*	+3	0
9g	17b	23b	387 ; 498*	+2	0
9g	17c	23c	387 ; 498*	-2	0
9g	17d	23d	387 ; 498*	+2	0

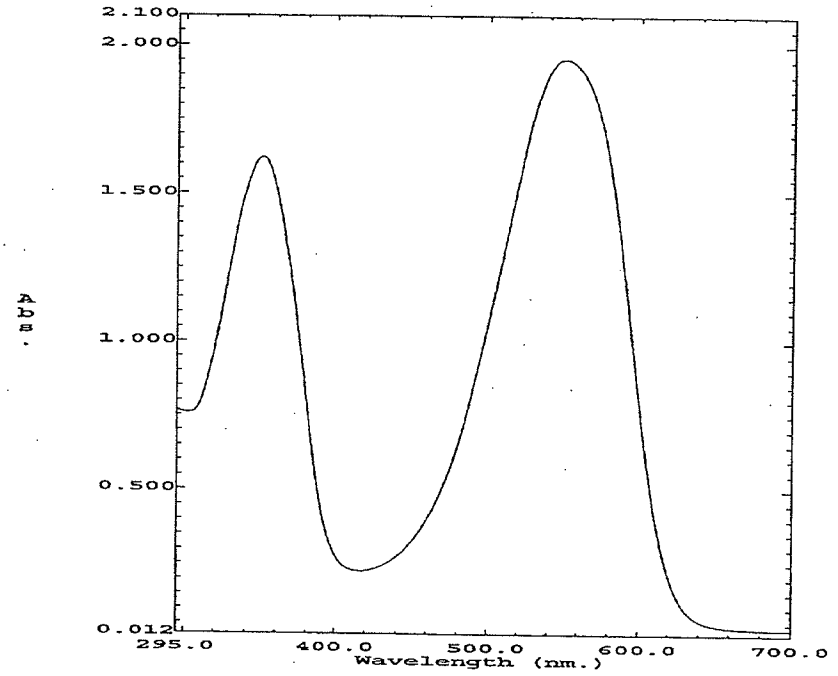

Figure 3.3.19: Absorption spectrum of **20a** in ethanol/HCl

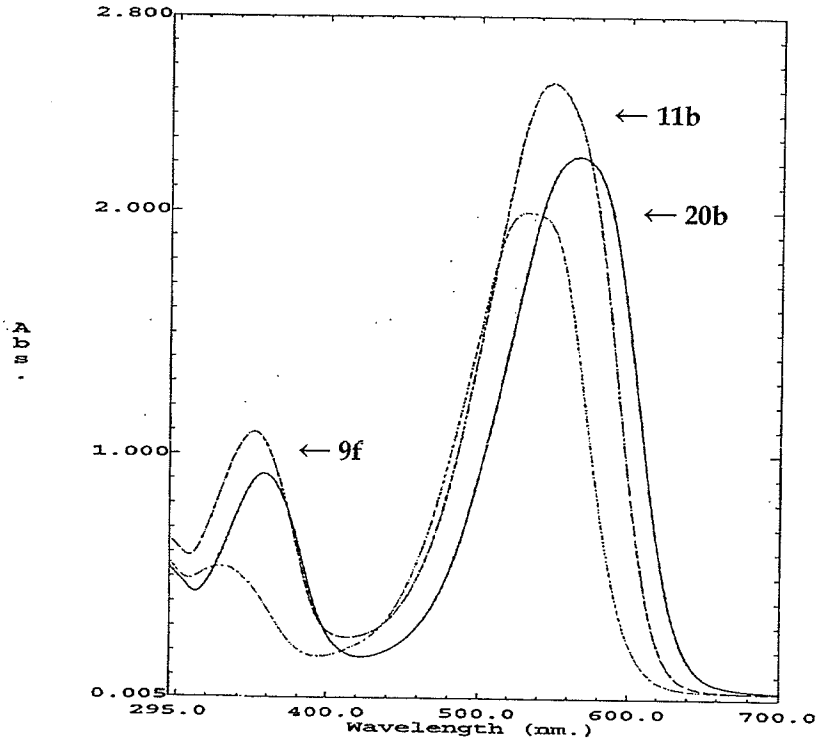

Figure 3.3.20: Absorption spectrum of compounds **9f**, **11b**, **20b** in ethanol/HCl

Thermogravimetric analysis of the dyes displayed a two step degradation process. The first step, occurring between 200-280°C, may be attributed to the release of the azo bond as molecular nitrogen (Section 1.2.4), since it occurs regardless of the structure of the azo dye. This correlates with previous reports that indicate cleavage of the azo bond is a common first weight loss step[45]. The remaining weight loss is therefore attributed to the destruction of the aromatic units remaining after removal of the nitrogen double bond. Figure 3.3.21 provides the TGA curve for **20b** as an example. Table 3.3.23 presents the TGA data.

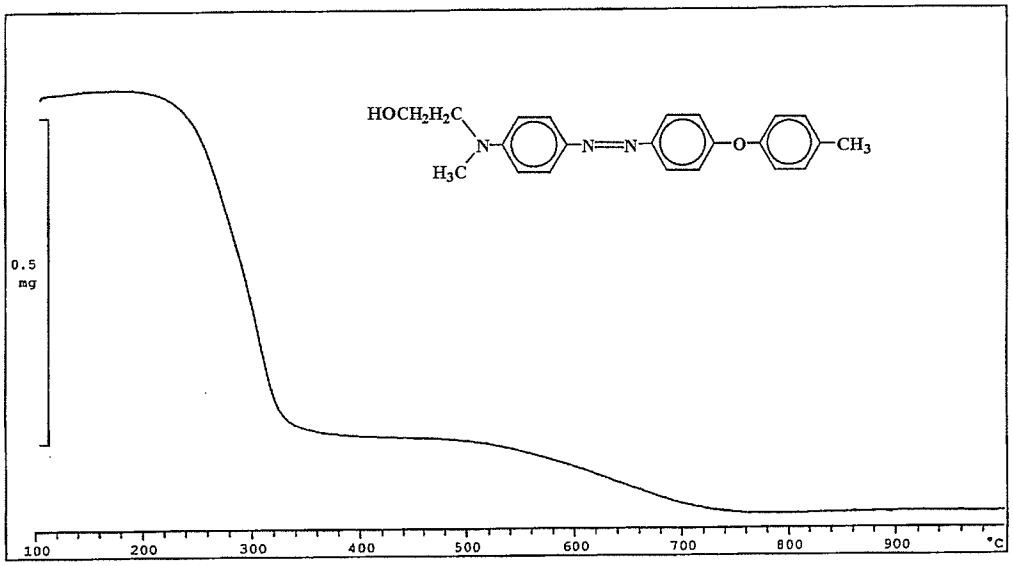

Figure 3.3.21: TGA curve for **20b**

*ii) Decomplexation of polymers **19a-i***

The organic polymers **24a-i** were isolated when **19a-i** were photolyzed using 300 nm light in an acetonitrile/dichloromethane mixture, as shown in Scheme 3.3.11. The organic polymers were fairly insoluble, and while ^{1}H NMR spectra were recorded for

all, only polymers **24a,b,d,e,g** were soluble enough to record ^{13}C NMR spectra. The ^{1}H NMR spectrum of **24d** is provided in Figure 3.3.22. As is expected, no Cp or complexed aromatic resonances are observed, while the remaining peaks still display the characteristic broad peak shape associated with macromolecular samples.

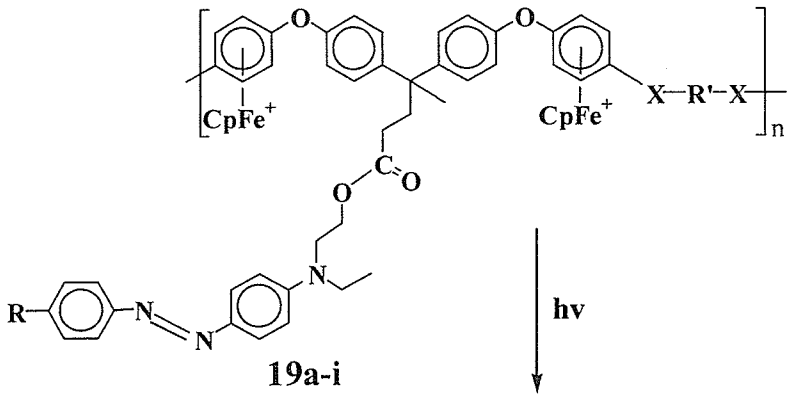

19a-i

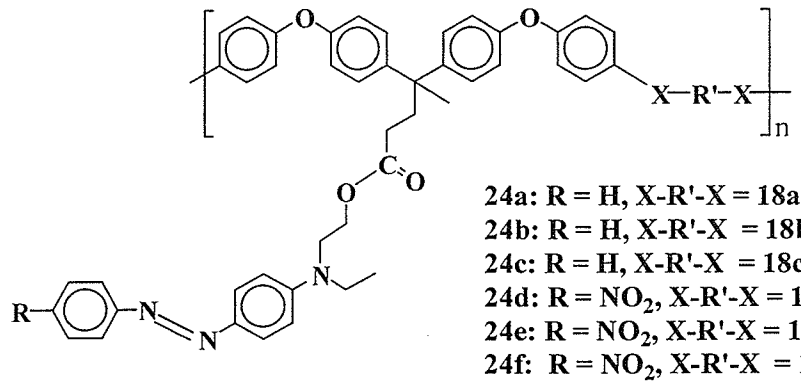

24a-i

24a: R = H, X-R'-X = 18a
24b: R = H, X-R'-X = 18b
24c: R = H, X-R'-X = 18c
24d: R = NO_2, X-R'-X = 18a
24e: R = NO_2, X-R'-X = 18b
24f: R = NO_2, X-R'-X = 18c
24g: R = $COCH_3$, X-R'-X = 18a
24h: R = $COCH_3$, X-R'-X = 18b
24i: R = $COCH_3$, X-R'-X = 18c

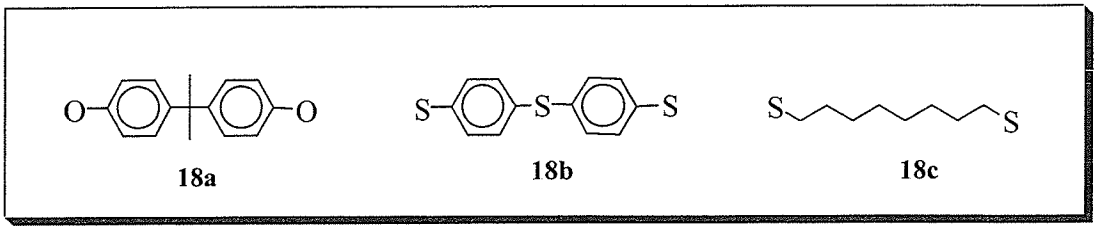

18a **18b** **18c**

Scheme 3.3.11

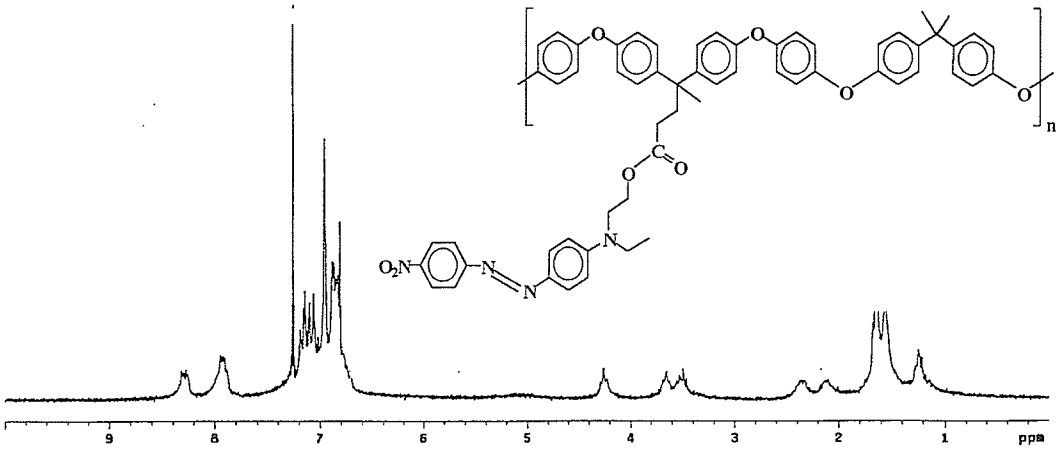

Figure 3.3.22: ^{1}H NMR spectrum of **24d**

The molecular weights of the polymers were determined as previously discussed and presented in Section 3.3.3. The TGA curves of the decomplexed polymeric materials displayed similar weight losses as the other decomplexed dyes.

The visible absorption of the organic polymers were almost identical to those of the complexed polymers, further substantiating that original complexation, which formed the organometallic monomers (Section 3.3.2), caused the changes in λ_{max}. Table 3.3.18 provides the absorption maxima for the decomplexed polymers and the degree of shift from the complexed polymers. Figure 3.3.23 illustrates the absorption profiles for the polymers incorporating bisphenol-A (**18a**). As can be seen, the presence of the electron-withdrawing NO_2 (**24d**) and $COCH_3$ (**24g**) groups shift the maxima to higher wavelengths when compared to the unsubstituted analogue (**24a**).

Table 3.3.18: Wavelength maxima for **24a-i**

Polymer	λ_{max} (nm)	$\Delta\lambda_{max}$ from $CpFe^+$ Polymer	λ_{max} (nm)	$\Delta\lambda_{max}$ from $CpFe^+$ Polymer	λ_{max} (nm)	$\Delta\lambda_{max}$ from $CpFe^+$ Polymer
DMF			**Ethanol**		**Ethanol /HCl**	
24a	417	-3	419	+5	427; 524	+3
24b	419	+1	415	-3	420; 523	-4
24c	419	0	414	-1	427; 521	0
24d	489	-1	478	-1	507; 540	-8
24e	490	-1	484	+2	513; 540	-4
24f	489	-2	482	0	512 ; 540	-3
24g	452	-1	448	-4	517 ; 549	-4
24h	454	0	453	+4	500 ; 549	-18
24i	452	0	462	+11	514 ; 549	-8

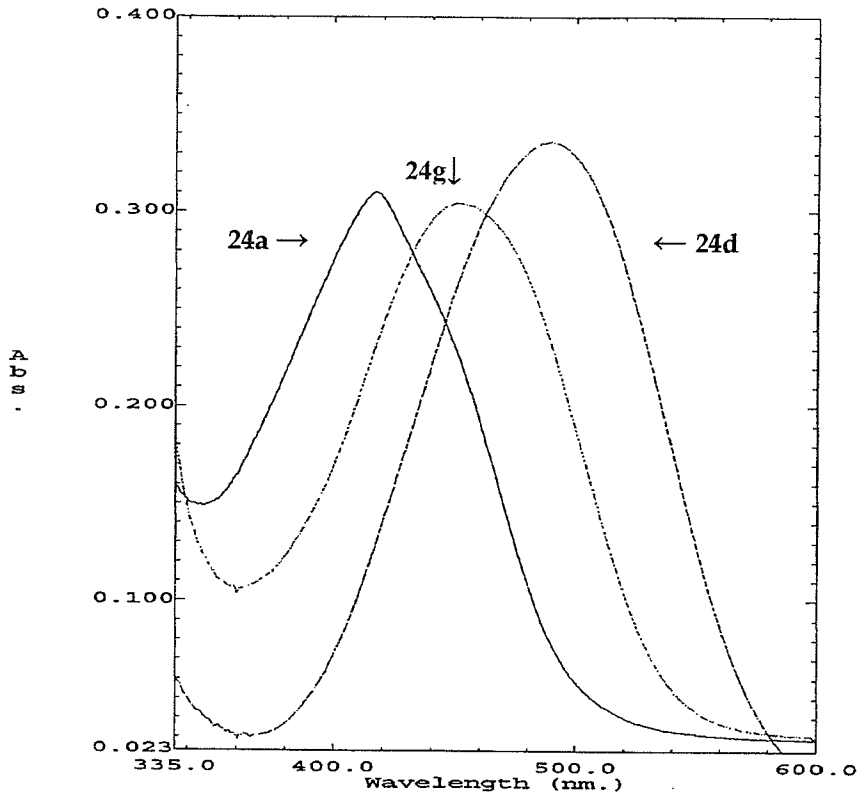

Figure 3.3.23: Wavelength maxima of **24a,d,g** in ethanol

Table 3.3.19: ^{1}H NMR data for compounds **20a-b ; 21a-c ; 22**

δ (ppm) in chloroform-d				
	Aromatic H	**CH_2**	**CH_3**	**Other**
20a	6.86 (d, 2H, J=9.4) 7.00 (d, 2H, J=8.4) 7.05 (d, 2H, J=9.0) 7.24 (d, 2H, J=8.7) 7.78 (d, 2H, J=9.4) 7.82 (d, 2H, J=9.2)	3.52-3.64 (m, 4H)	1.21 (t, 3H, J=7.0) 3.77 (t, 2H, J=6.1) 2.33 (s, 3H)	4.15 (s, 1H) OH
20b	6.85 (d, 2H, J=9.0) 6.99 (d, 2H, J=8.6) 7.05 (d, 2H, J=9.0) 7.24 (d, 2H, J=8.2) 7.79 (d, 2H, J=9.4) 7.82 (d, 2H, J=9.0)	3.61 (t, 2H, J=5.7) 3.78 (t, 2H, J=5.7)	2.33 (s, 3H) 3.12 (s, 3H)	10.81 (s, 1H) OH
21a	6.91-7.01 (m, 9H) 7.20 (d, 4H, J=8.6) 7.36 (d, 2H, J=9.0) 7.42-7.52 (m, 6H) 7.78 (d, 2H, J=8.4) 7.89 (d, 2H, J=9.0)	2.10-2.15 (m, 2H) 2.35-2.45 (m, 2H) 3.58 (q, 2H, J=7.0) 3.76 (t, 2H, J=5.9) 4.29 (t, 2H, J=5.9)	1.21 (t, 3H, J=6.6) 1.60 (s, 3H)	------
21b	6.90-7.10 (m, 10H) 7.19 (d, 4H, J=9.0) 7.36 (d, 4H, J=9.0) 7.89 (d, 2H, J=9.4) 7.92 (d, 2H, J=9.4) 8.33 (d, 2H, J=9.0)	2.09-2.14 (m, 2H) 2.33-2.45 (m, 2H) 3.61 (q, 2H, J=7.0) 3.79 (t, 2H, J=5.9) 4.31 (t, 2H, J=5.9)	1.23 (t, 3H, J=7.0) 1.59 (s, 3H)	------
21c	6.79 (d, 2H, J=8.9) 6.85-6.97 (m, 8H) 7.11 (d, 4H, J=8.9) 7.18-7.29 (m, 4H) 7.81-7.88 (m, 4H) 8.04 (d, 2H, J=8.2)	2.01-2.15 (m, 2H) 2.30-2.49 (m, 2H) 3.49 (q, 2H, J=7.0) 3.65 (t, 2H, J=6.3) 4.26 (t, 2H, J=6.6)	1.23 (t, 3H, J=7.4) 1.58 (s, 3H) 2.64 (s, 3H)	------
22	6.86 (d, 4H, J=9.4) 7.14 (d, 4H, J=9.0) 7.19 (s, 4H) 7.79 (d, 4H, J=9.4) 7.85 (d, 4H, J=9.0)	3.52-3.54 (m, 4H) 3.74-3.83 (m, 4H) 3.87-3.95 (m, 4H)	1.18-1.29 (m, 6H)	------

Coupling constants calculated in Hz

Table 3.3.20: ^{13}C NMR data for compounds **20a-b ; 21a-c ; 22**

δ (ppm) in chloroform-d					
	quat ArC	**ArCH**	**CH_2**	**CH_3**	**Others**
20a	134.32 143.88 149.46 151.41 155.08 159.90	112.17 118.87 120.30 124.43 125.67 131.29	46.31 53.38 59.99	12.32 20.67	------
20b	134.41 144.06 149.56 152.74 155.15 160.03	112.26 118.90 120.36 124.49 125.46 131.32	55.29 59.96	20.66 39.45	------
21a	128.53 143.93 145.03 151.81 153.44 155.62 157.17	112.59 119.29 120.88 122.67 126.19 129.57 129.86 130.19 130.56	30.80 37.18 45.79 49.25 62.24	12.41 27.74	45.64* 173.63*
21b	128.43 144.33 145.08 148.34 152.96 155.62 157.13 157.68	112.53 119.36 120.82 123.33 125.49 126.98 129.61 130.59	30.83 37.18 45.67 49.13 62.24	12.35 27.74	45.59* 173.65*
21c	128.12 136.91 143.50 143.76 150.69 154.83 155.74	111.33 118.31 119.96 122.13 125.71 128.50 129.26 129.60	30.21 36.41 44.87 48.55 61.38	12.22 26.74 27.62	------
22	142.46 148.61 150.69 152.36 158.58	111.46 118.59 121.48 123.95 125.15	45.44 52.51 58.72	12.42	------

* quaternary carbon

Table 3.3.21: ^{1}H NMR data for compounds **23a-d**

δ (ppm) in acetone-d6			
	Aromatic H	**CH_3**	**Other**
23a	6.38 (d, 1H, J=2.3) 6.58 (dd, 1H, J=8.6, 2.3) 6.99 (d, 4H, J=9.0) 7.12 (d, 4H, J=7.8) 7.23 (d, 2H, J=7.6) 7.44 (t, 1H, J=7.8) 7.69 (d, 1H, J=8.6) 7.76 (d, 2H, J=9.0)	------	------
23b	6.40 (d, 1H, J=2.7) 6.60 (dd, 1H, J=8.9, 2.5) 7.00 (d, 4H, J=8.6) 7.08 (d, 4H, J=9.0) 7.25 (d, 2H, J=8.2) 7.72 (d, 1H, J=8.6) 7.87 (d, 2H, J=9.0)	2.34 (s, 6H)	9.39 (s, 1H) 13.09 (s, 1H)
23c	6.40 (d, 1H, J=2.3Hz) 6.61 (dd, 1H, J=8.8, 2.3) 6.86-6.96 (m, 4H) 7.02-7.06 (m, 2H) 7.11 (d, 2H, J=8.6) 7.31 (d, 2H, J=8.6) 7.73 (d, 1H, J=9.0) 7.88 (d, 2H, J=8.6)	2.34 (s, 6H)	9.3 (s, 1H) 13.10 (s, 1H)
23d	6.82 (dd, 2H, J=8.2, 2.3) 6.91 (d, 1H, J=2.3) 7.07 (d, 2H, J=9.0) 7.18 (d, 2H, J=8.2) 7.72 (d, 2H, J=8.2) 7.85 (d, 2H, J=9.0)	2.24 (s, 12H)	9.37 (s, 1H) 13.10 (s, 1H)

Coupling constants calculated in Hz

Table 3.3.22: ^{13}C NMR data for compounds **23a-d**

δ (ppm) in chloroform-d			
	quat ArCH	**ArCH**	**CH_3**
23a	133.02 144.82 156.32 156.60 160.72 162.45 163.18	103.94 109.28 116.87 119.48 124.25 130.92 134.62 135.05	------
23b	133.29 134.75 146.98 154.75 156.60 160.85 163.09	104.00 109.65 119.03 120.60 124.18 131.41 135.05	20.70
23c	133.05 140.92 146.92 156.42 156.93 160.22 162.92	103.75 109.43 117.22 119.25 120.81 123.99 125.61 130.46 134.88	21.10
23d	133.13 133.22 139.23 146.70 154.71 156.44 160.81 162.91	103.85 109.46 117.78 118.81 121.66 124.00 131.56 134.92	18.93 19.72

* quaternary carbon

Table 3.3.23: Yield, IR and TGA data for compounds **20a-b ; 21a-c ; 22 ; 23a-d**

	%Yield	IR (cm^{-1})	TGA_{onset} (°C)	TGA_{endset} (°C)	$TGA_{midpoint}$ (°C)	%loss
20a	75	3472 (OH)	249 672	299 763	271 696	47 20
20b	73	3427 (OH)	258 579	325 691	290 624	57 13
21a	90	1732 (C=O)	387	467	413	52
21b	88	1735 (C=O)	322 604	362 690	337 650	20 11
21c	86	1736 (C=O) 1679 (C=O)	243 415	283 485	254 441	8 30
22	85	3382 (OH)	287 669	341 719	319 696	34 19
23a	90	3190 (OH)	210 657	224 742	217 699	14 17
23b	70	3407 (OH)	203 542	245 644	228 575	25 14
23c	95	3448 (OH)	205 580	245 648	229 583	30 15
23d	87	3427 (OH)	211 469	266 485	242 479	35 10

Table 3.3.24: ^{1}H NMR data for polymers **24a-i**. (Coupling constants calculated in Hz)

δ (ppm) in chloroform-d			
	Aromatic H	**CH_2**	**Others**
24a	6.87-6.98 (m, 20H) 7.03-7.25 (m, 7H) 7.32-7.45 (m, 4H) 7.80-7.89 (m, 2H)	2.01-2.23 (m, 2H) 2.35-2.51 (m, 2H) 3.35-3.42 (m, 2H) 3.63-3.71 (m, 2H) 4.15-4.31 (m, 2H)	1.15-1.30 (m, 3H) CH_3 1.45-1.78 (m, 9H) CH_3
24b	6.83-6.99 (m, 20H) 7.01-7.25 (m, 7H) 7.25-7.42 (m, 4H) 7.72-7.89 (m, 2H)	2.01-2.23 (m, 2H) 2.36-2.51 (m, 2H) 3.43-3.59 (m, 2H) 3.65-3.73 (m, 2H) 4.16-4.34 (m, 2H)	1.15-1.30 (m, 3H) CH_3 1.45-1.78 (s, 3H) CH_3
24c	6.70-6.81 (m, 8H) 6.84-6.99 (m, 8H) 7.05-7.20 (m, 4H) 7.68-7.75 (m, 4H)	2.02-2.24 (m, 2H) 2.21-2.45 (m, 2H) 3.40-3.51 (m, 2H) 3.61-3.78 (m, 2H) 4.01-4.24 (m, 2H)	1.01-1.25 (m, 16H) CH_3 and CH_2 1.43-1.65 (m, 6H) CH_3 and CH_2
24d	6.81-6.99 (m, 16H) 7.05-7.23 (m, 10H) 7.25-7.42 (m, 4H) 8.10-8.37 (m, 2H)	2.05-2.30 (m, 2H) 2.31-2.46 (m, 2H) 3.41-3.51 (m, 2H) 3.55-3.69 (m, 2H) 4.15-4.35 (m, 2H)	1.05-1.29 (m, 3H) CH_3 1.45-1.65 (m, 9H) CH_3
24e	6.76-6.89 (m, 12H) 7.01-7.18 (m, 10H) 7.25-7.37 (m, 4H) 7.85-7.94 (m, 4H) 8.15-8.36 (m, 2H)	2.09-2.25 (m, 2H) 2.25-2.45 (m, 2H) 3.42-3.58 (m, 2H) 3.55-3.76 (m, 2H) 4.18-4.31 (m, 2H)	1.05-1.30 (m, 3H) CH_3 1.61 (s, 3H) CH_3
24f	6.85-7.01 (m, 2H) 7.08-7.19 (m, 2H) 7.15-7.35 (m, 2H) 7.85-8.05 (m, 2H) 8.21-8.39 (m, 2H)	2.05-2.20 (m, 2H) 2.20-2.35 (m, 2H) 3.41-3.52 (m, 2H) 3.59-3.69 (m, 2H) 4.20-4.35 (m, 2H)	0.97-1.19 (m, 3H) CH_3 1.20-1.39 (m, 19H) CH_3 and CH_2
24g	6.80-6.92 (m, 14H) 6.95-7.20 (m, 12H) 7.77-7.89 (m, 4H) 7.95-8.09 (m, 2H)	2.01-2.26 (m, 2H) 2.29-2.45 (m, 2H) 3.39-3.50 (m, 2H) 3.55-3.69 (m, 2H) 4.18-4.32 (m, 2H)	0.99-1.29 (m, 3H) CH_3 1.65 (br s, 9H) CH_3 2.63 (s, 3H) CH_3
24h	6.85-6.97 (m, 12H) 7.01-7.19 (m, 10H) 7.25-7.45 (m, 4H) 7.78-7.89 (m, 4H) 7.95-8.07 (m, 2H)	2.06-2.19 (m, 2H) 2.22-2.41 (m, 2H) 3.40-3.50 (m, 2H) 3.50-3.65 (m, 2H) 4.18-4.32 (m, 2H)	0.97-1.29 (m, 3H) CH_3 1.56 (s, 3H) CH_3 2.61 (s, 3H) CH_3
24i	6.78-6.92 (m, 12H) 7.00-7.65 (br m, 8H) 7.80-7.92 (m, 4H)	2.08-2.25 (m, 8H) 3.32-3.52 (m, 4H) 4.16-4.31 (m, 2H)	0.96-1.31 (m, 3H) CH_3 1.39-1.56 (m, 5H) CH_3 and CH_2 2.45-2.71 (m, 13H) CH_3 and CH_2

Table 3.3.25: ^{13}C NMR data for soluble polymers **24a,b,d,e,g**

δ (ppm) in chloroform-d					
	quat ArC	**ArCH**	**CH_2**	**CH_3**	**Others**
24a	142.91 143.58 145.21 150.02 152.34 152.70 155.43 155.76	111.33 117.58 120.29 120.41 122.12 125.19 127.93 128.39 128.86 129.40	30.23 36.49 44.77 48.58 61.45	12.25 27.69 31.00	42.01* 45.33* 173.69*
24b	127.11 133.31 136.81 143.79 150.05 152.65 154.33 157.44	111.37 118.79 119.24 122.08 125.26 128.52 128.83 129.47 131.42 134.58	28.77 36.42 44.94 48.35 61.45	12.32 27.64 29.35	45.24* 173.45*
24d	142.86 143.69 145.22 147.27 151.22 152.72 155.39 155.75 156.57	111.39 117.59 120.26 120.35 122.55 124.56 126.18 127.92 128.36	30.23 36.44 44.75 48.57 61.29	12.22 27.64 30.98	42.00* 45.40* 173.59*
24e	127.28 133.39 136.82 143.78 147.32 151.27 154.40 156.55 157.47	111.43 118.83 119.28 122.56 124.59 126.21 128.56 129.57 131.48 134.56	30.21 36.43 44.94 48.62 61.34	12.24 27.66	45.42* 173.47*

* quaternary carbon

Table 3.3.25: continued

24g	136.91 142.86 143.71 145.22 146.10 150.69 152.70 155.42 155.71	111.35 117.59 119.18 120.37 122.12 125.77 127.92 128.38 129.28	30.18 36.43 44.80 48.59 61.34	12.23 26.73 30.99	42.00* 45.37* 173.56* 197.49*

Table 3.3.26: Yield, IR and TGA data for polymers **24a-i**

	%Yield	**IR (cm^{-1})**	**TGA_{onset} (°C)**	**TGA_{endset} (°C)**	**$TGA_{midpoint}$ (°C)**	**%loss**
24a	58	1734 (C=O)	246 404 507	308 456 548	263 432 525	14 21 19
24b	40	1733 (C=O)	260 475	297 496	277 486	10 10
24c	50	1734 (C=O)	267 517 620	289 560 669	269 531 643	9 16 22
24d	70	1734 (C=O)	269 502	316 539	297 522	7 24
24e	35	1731 (C=O)	242 440 605	274 456 680	275 450 640	7 22 53
24f	40	1734 (C=O)	206 585	303 686	255 647	70 9
24g	70	1734 (C=O) 1679 (C=O)	269 519	307 615	285 552	8 72
24h	30	1737 (C=O) 1686 (C=O)	279 481	307 512	295 493	4 14
24i	45	1735 (C=O) 1679 (C=O)	217 416	245 446	231 432	6 28

3.3.5 Photochemical/Thermal stability of azo dyes

3.3.5.a) Photooxidation of azo dyes

As outlined in Section 1.2.4, oxidative techniques have proven successful in bleaching azo compounds. A preliminary study was therefore performed to determine whether the azo dyes synthesized could be efficiently degraded using hydrogen peroxide and 300 nm light. Five dyes (**9d**, **9g**, **11b**, **17d**, **24d**) were chosen as representative examples for hydrogen peroxide trials. An excess of hydrogen peroxide (mol dye:mol H_2O_2 approximately $0.02x10^{-3}$:1) was utilized in the trials to ensure that the amount of H_2O_2 present could be taken as constant throughout the photolysis (with the assumption that the photolysis period was not sufficiently long enough to remove the excess peroxide). Irradiated trials without H_2O_2 were performed for comparison.

3.3.5.a.i) Compound **9d** was exposed to 300 nm irradiation in the presence of H_2O_2, and was observed to bleach rapidly within 20-30 minutes, whereas the trial without H_2O_2 showed negligible change over the same time period. After 30 minutes the absorbance of the dye in the oxidative medium was not observed to change significantly, and thus the degradation was essentially complete within 30 minutes. This correlates well to other reports that indicate rapid colour loss within the first 10-30 minutes of photolysis[110]. Figure 3.3.24 presents the absorbance changes over time for **9d**, while Figure 3.3.25 compares the trial with and without peroxide.

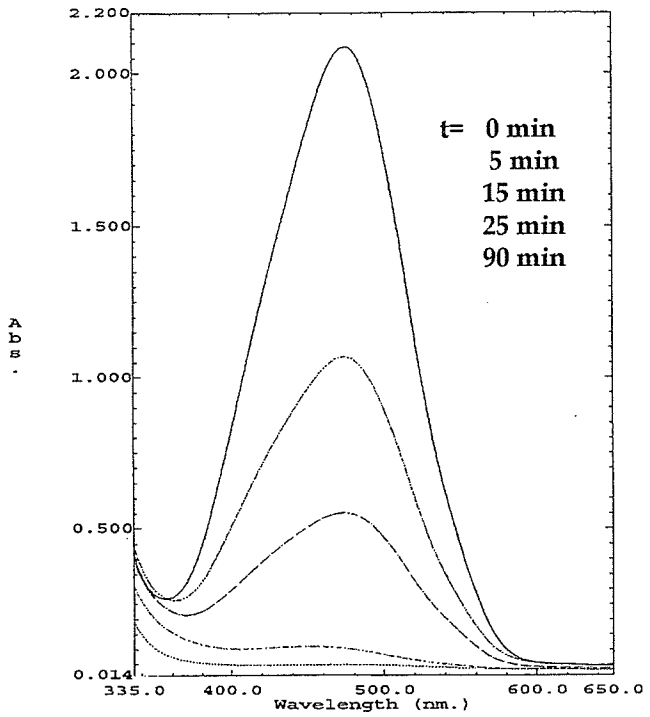

Figure 3.3.24: Absorption spectra at time: 0, 5, 15, 25 and 90 minutes for photolysis of **9d** with H_2O_2

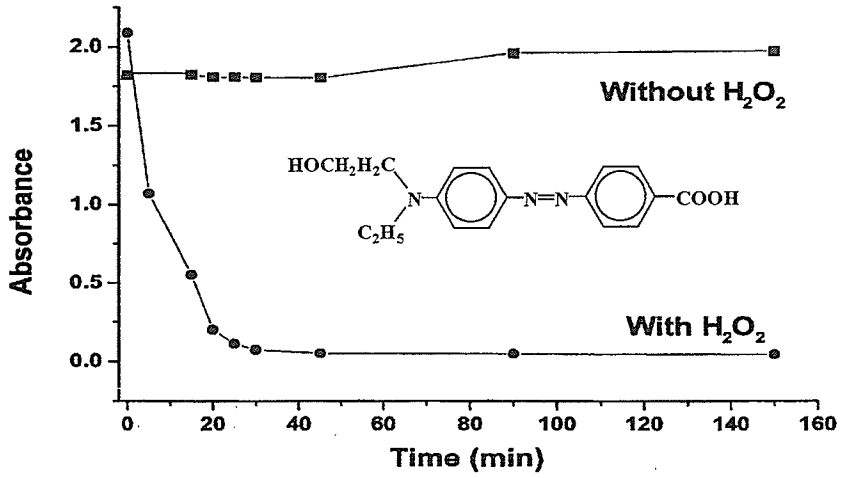

Figure 3.3.25: Comparison of 300 nm irradiation of **9d** with and without H_2O_2 present

In addition to examining the wavelength changes, an attempt was made to isolate the products of the photocatalytic oxidation. Previous reports have illustrated the presence of low molecular weight polar compounds[110-114], thus $CHCl_3$ was used as an extraction solvent in an attempt to recover any of these products. Due to the low concentration of the original starting dye, isolation of any products was met with limited success. However, the GC-MS of the extracted residue remaining from the H_2O_2 trial did show a small amount of benzoic acid present. This is not unexpected, as the formation of low molecular weight acids has previously been reported in the aqueous oxidation of azo compounds[108,117]. The identity of the peak in the GC-MS chromatogram was determined by comparison of EI spectra of standard compounds available from the National Institute of Standards and Technology (NIST). Figure 3.3.26 provides the experimental mass spectrum from **9d** and of benzoic acid (available from NIST). Table 3.3.27 presents the m/z values and the relative abundances for the experimental GC-MS peak.

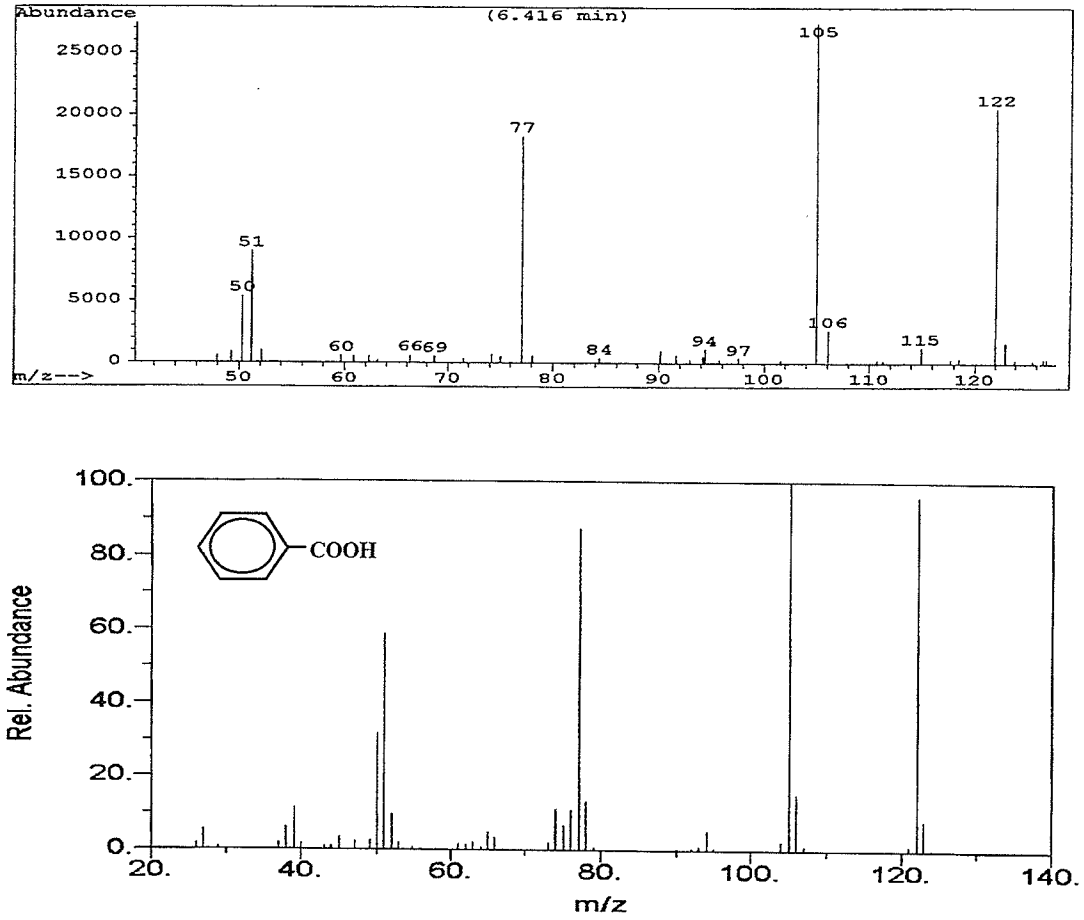

Figure 3.3.26: Mass spectrum of extracted **9d** product (top) and benzoic acid (bottom)

Table 3.3.27: Relative abundances of m/z peaks from **9d** photooxidation product

m/z	Rel. abundance
50.30	24
51.25	32
52.20	5
74.15	7
77.05	79
78.15	7
105.05	100
105.95	9
121.95	87
122.95	6

3.3.5.a.ii) The decomplexed polymer **24d** was examined to see whether any change would be observed on moving from a low molecular weight dye to a macromolecular dye. As is evident in Figure 3.3.27 and 3.3.28, the compound required a slightly longer period to degrade, which may be attributed to either the greater number of chromophore units per molecule, or the conformation of the polymer that may inhibit the ability of H_2O_2 to actively interact with the azo chromophore. Regardless, within 90 minutes of photolysis the solution became clear, with absorbance values approaching zero. Attempts to isolate products of the degradation through extraction of the aqueous sample with chloroform, and concentration of the solvent followed by injection into a GC-MS, were unsuccessful.

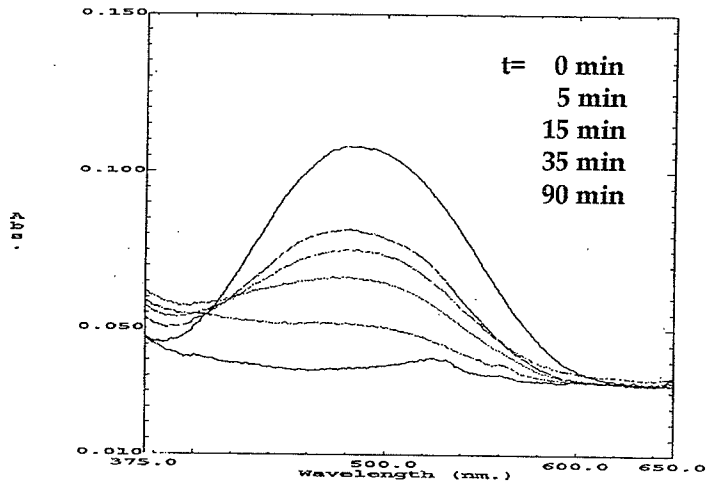

Figure 3.3.27: Absorption spectra at time: 0, 5, 10, 15, 35, 90 minutes for photolysis of **24d** with H_2O_2 with 300 nm irradiation

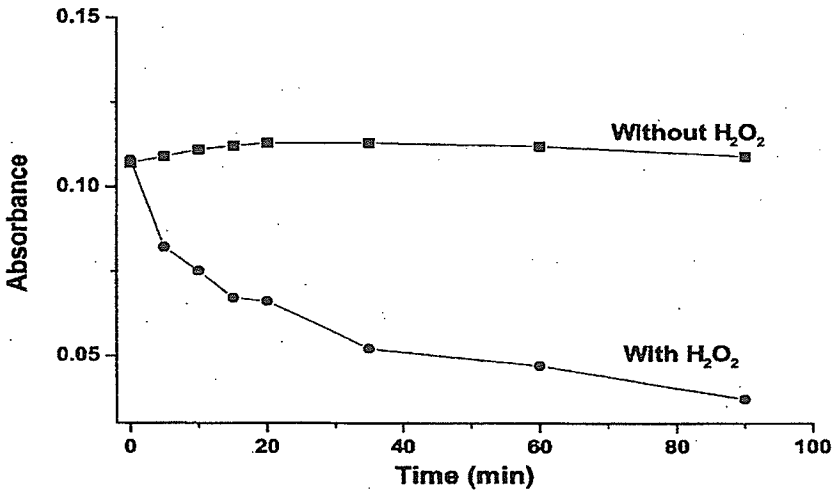

Figure 3.3.28: Comparison of 300 nm irradiation of **24d** with and without H_2O_2

3.3.5.a.iii) The complexed compound **11b** posed an interesting problem, in that the photolysis without H_2O_2 would be expected to change with irradiation, given that the complex would undergo photolytic decomplexation. However, the successful isolation of the decomplexed dyes proved that photolysis in hydrocarbon solvents does not adversely affect the dye structure, thus a comparison of the effect of H_2O_2 could be made if one examined the time required to cause absorbance changes in the trial with and without H_2O_2. Understandably, one would expect the trial with H_2O_2 to undergo a faster change than the trial without. As can be observed in Table 3.3.28, the sample photolyzed with H_2O_2 displayed a faster rate of change. The absorbance of the trial without H_2O_2 was seen to change (Figure 3.3.29), as the solution became slightly opaque but remained coloured (resulting from the decomplexation reaction), while the trial containing H_2O_2 was observed to become clear (resulting from the degradation of the dye molecule). In fact, the rate of colour removal was more rapid than with **9d** or **24d**, as the absorbance became insignificant in approximately 10 minutes. The exact reason

for this is unclear, however it is plausible that the liberated iron from **11b** may initiate a type of photo-Fenton reaction that may increase the rate of oxidation.

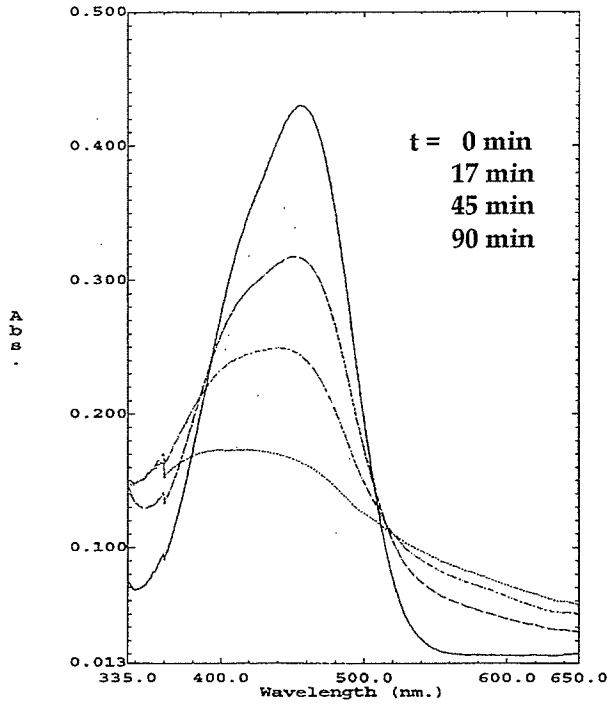

Figure 3.3.29: Change in absorbance of **11b** with 300 nm irradiation without H_2O_2

Table 3.3.28: Absorbance of **11b** with increasing irradiation time with and without H_2O_2

Time (min)	Absorbance with H_2O_2	Absorbance without H_2O_2
0	0.3880	0.4300
2	0.0914	0.3506
7	0.0297	0.3355
17	0.0332	0.3175
45	----	0.2494
90	----	0.1635
150	----	0.1777

3.3.5.a.iv) The azo dye (**9g**) showed a relatively slow degradation with H_2O_2 when irradiated with 300 nm light. Table 3.3.29 provides the λ_{max} values with time for the trials with and without H_2O_2. It was surmised that given the possibility that this compound may exist as the hydrazone tautomer, the presence of a N-H bond could be impeding the hydroxyl radicals from approaching the azo bond. Thus the time required for destruction of the dye would be longer when compared to the previous examples.

Table 3.3.29: Absorbance of 300 nm irradiated samples of **9g** with and without H_2O_2

Time (min)	Absorbance with H_2O_2	Absorbance w/o H_2O_2
0	0.5959	0.7311
15	0.5072	0.6043
20	0.4284	0.6937
25	0.3794	0.6603
30	0.3621	0.6325
45	0.3042	0.6476
90	0.1345	0.7307
150	0.0705	0.7283

In order to test the hypothesis regarding whether the tautomers could be affecting the rate, a trial was attempted at pH 10 by adding a couple of drops of concentrated ammonia solution. In the presence of base, the absorbance band of the dye was observed to change from 381 nm to 470 nm, due to the creation of phenoxide groups. The appearance of the phenoxide functionality causes two strong electron-donating (σ_p = -0.81, σ_m = -0.47) groups to be present on the coupling component, whereas the protonated form exhibits much less electron-donating ability (OH: σ_p = -0.38, σ_m = +0.13). However, upon sitting in the dark, the absorbance band is observed to shift hypsochromically to approximately 320 nm. This effect has not been readily explained

in the literature, but is most likely attributed to an equilibrium established between the n-π^* and the π-π^* states. Figure 3.3.30 illustrates the absorbance of **9g** at pH 10 at time 0, 30, 60 and 120 minutes.

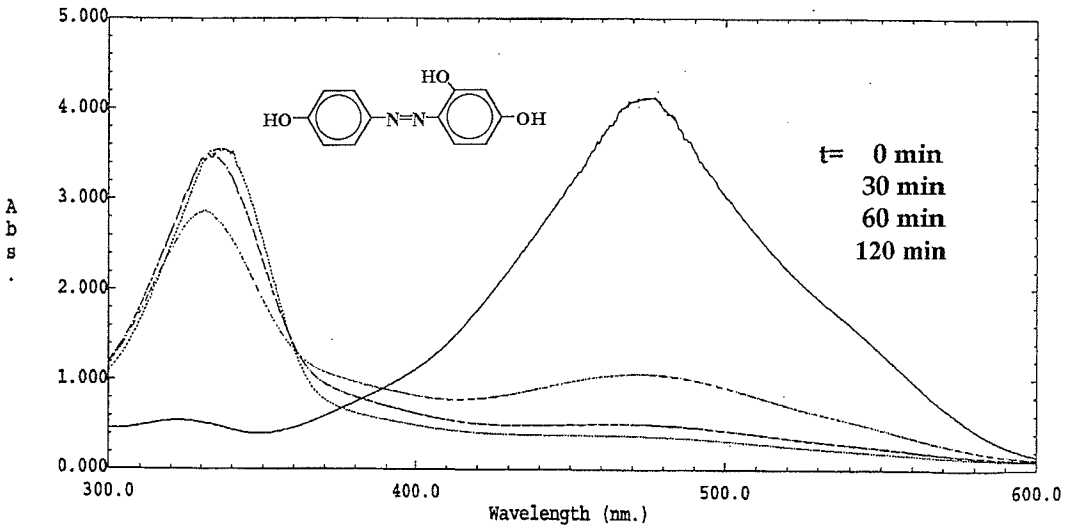

Figure 3.3.30: Change in wavelength maxima of **9g** upon sitting in the dark at pH 10

It was discovered that at pH 10 the degradation occurred extremely rapidly in the presence of hydrogen peroxide and UV light. Indeed, the first attempt to monitor the reaction met with failure due to the solution turning clear in mere seconds. Thus another attempt was made, one in which the solution was not irradiated with 300 nm light, but was placed in a spectrophotometer to monitor the 320 nm absorbance band over time. The hydrogen peroxide was not added until the 320 nm band was observed to dominate the absorption spectrum. Upon placing the hydrogen peroxide in the solution, an immediate release of gas was observed, and the solution became essentially clear within 20 minutes. Figure 3.3.31 compares the trial with H_2O_2 and 300 nm irradiation (at lower pH) to that of the H_2O_2 degradation without 300 nm irradiation at pH 10. The data

is presented as percent absorbance remaining, which sets the absorbance at time 0 to 100%, with all subsequent readings relative to this initial value. It should be noted that while the spectrometer itself may be considered a source of irradiation, the relative intensity is much smaller than the photoreactor (which is equipped with sixteen 300 nm lamps). The pH of the solution without addition of ammonia was found to be 5.5. The increase in rate suggests that the tautomers may have been hindering the degradation, however, this would not explain why irradiation with 300 nm light is no longer required.

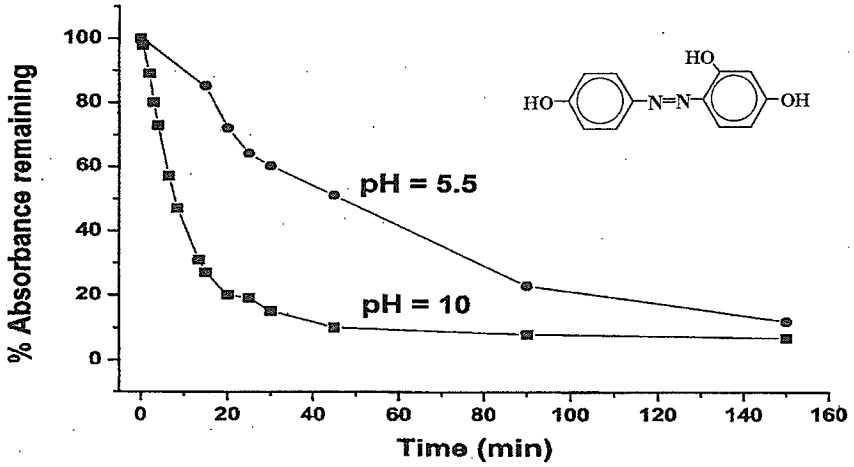

Figure 3.3.31: Comparison of degradation of **9g** at pH 5.5 with 300 nm irradiation, and pH 10 without 300 nm irradiation

3.3.5.a.v) Given the success observed with **9g** in the presence of hydrogen peroxide at high pH, complexed dye **17d** was placed in the spectrophotometer to measure its absorbance without any exposure to 300 nm light. **17d** displayed the same change in absorbance upon addition of ammonia, however was not observed to form a 320 nm band. Thus, the trial was performed on the 445 nm band of **17d**. Figure 3.3.32 presents the change in absorbance of the 445 nm band over time, with H_2O_2 present.

The solution was observed to become clear rapidly, even with a reduced amount of hydrogen peroxide. Again, this may be due to the presence of the ferrous ion that, once released via photolytic decomplexation, may catalyze the reaction. The control again displayed a change in absorbance similar to **11b**.

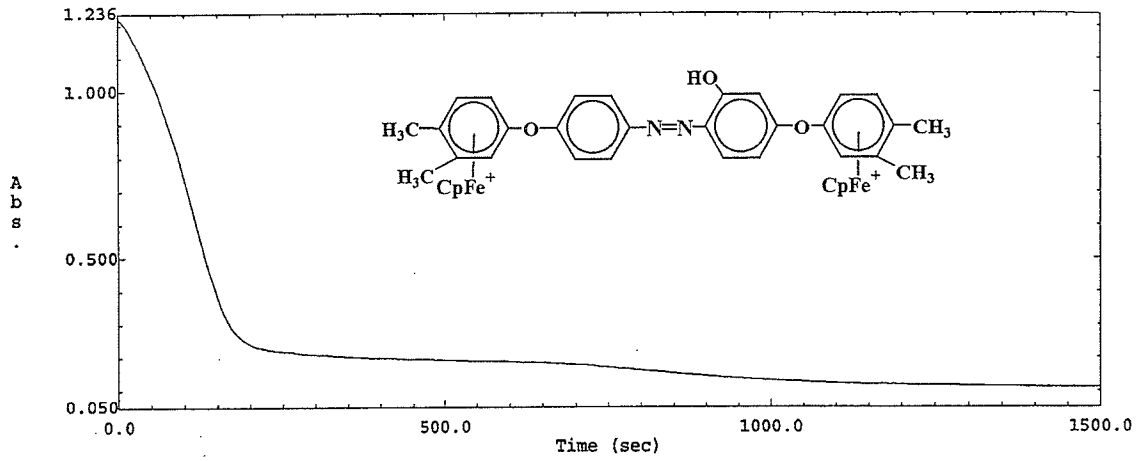

Figure 3.3.32: Absorbance of the 445 nm band of **17d** with H_2O_2 at pH 10 without 300 nm irradiation

3.3.5.b) Thermolytic degradation of azo dyes

Given that the thermogravimetric analysis curves displayed two weight losses for most of the dyes created, and thus indicated the formation of stable thermolysis products, an attempt was made to isolate the products of thermolysis. Three compounds were examined, **9g**, **11b** and **24d**. Heating of **11b** and **24d** to temperatures that indicated a weight loss on the TGA curve resulted in the formation of a black char from which no products could be identified. However, compound **9g** did produce detectable products. Two sets of broad peaks were observed in the GC-MS chromatogram (Figure 3.3.33). The first set of co-eluting peaks are attributed to low molecular weight products, two of which were identified as 4-aminophenol (8.57 min) and resorcinol (8.99 min). Identities

were established by comparison to spectra provided by NIST. The mass spectra of these two identified peaks and the corresponding NIST spectra are provided in Figure 3.3.34 and 3.3.35. Tables 3.3.30 and 3.3.31 provide the m/z values and the relative abundances of the two peaks.

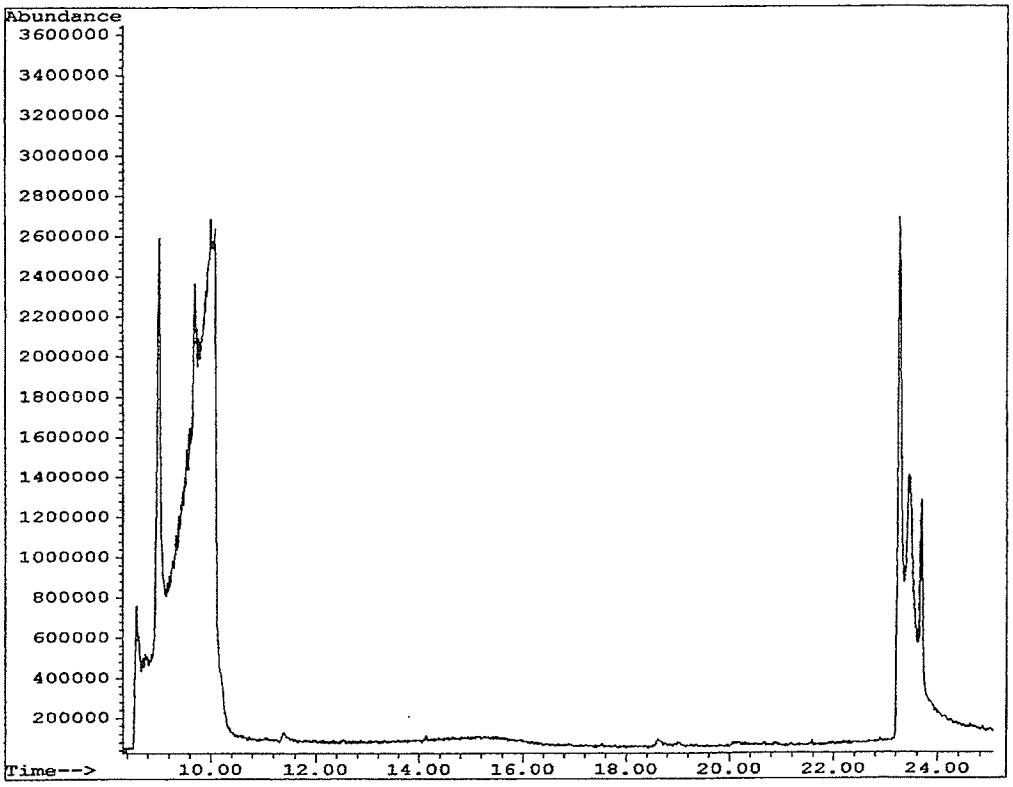

Figure 3.3.33: GC/MS Chromatogram of **9g** thermolysis product

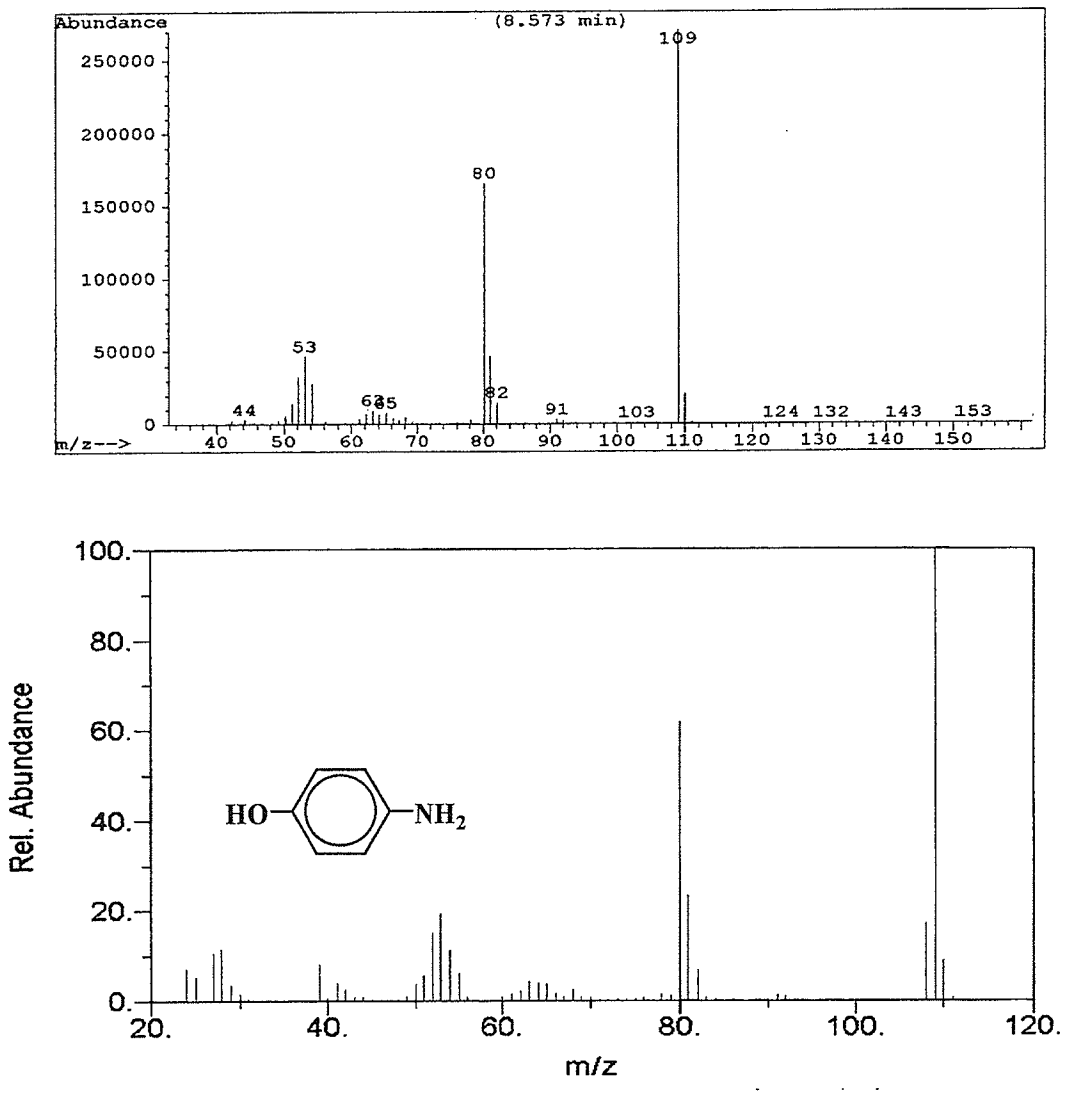

Figure 3.3.34: Mass spectrum of 8.57 minute thermolysis product of **9g** (top) and the corresponding NIST spectrum (bottom)

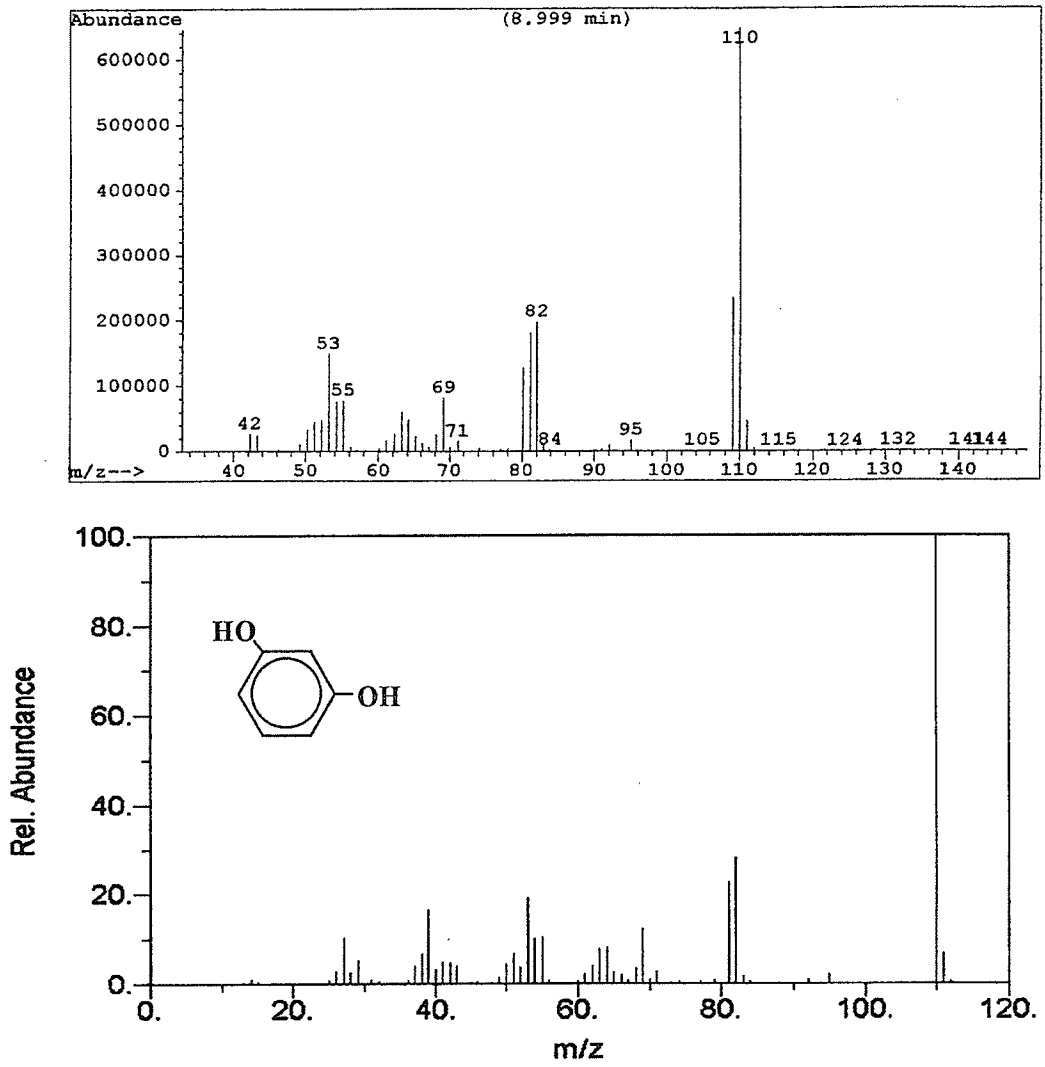

Figure 3.3.35: Mass spectrum of 8.99 minute thermolysis product of **9g** and the corresponding NIST spectrum

Table 3.3.30: m/z values and relative abundances of 8.57 minute peak in GC-MS chromatogram

m/z	Rel. Abundance
51.25	5
52.15	12
53.15	17
54.25	10
80.15	61
81.05	17
82.05	5
109.05	100
110.00	8

Table 3.3.31: m/z values and relative abundances of 8.99 minute peak in GC-MS chromatogram

m/z	Rel. Abundance	m/z	Rel. Abundance
50.20	5	69.15	13
51.15	7	80.15	20
52.15	7	81.15	28
53.15	23	82.05	31
54.25	12	109.05	36
55.15	12	110.00	100
63.20	9	111.00	7

The second set of peaks in the GC-MS chromatogram belong to the undegraded dye **9g**, and a set of unidentified higher molecular weight products, which may result from a high temperature reaction or polymerization. The mass spectrum of the first peak in the chromatogram (23.28 min) is presented in Figure 3.3.36. The base peak in the mass spectrum is 230 amu, which coincides with the molecular weight of dye **9g**. The fragment ions correspond to logical losses as shown in Figure 3.3.37. Table 3.3.32 presents the m/z values and relative abundances of the 23.28 minute peak.

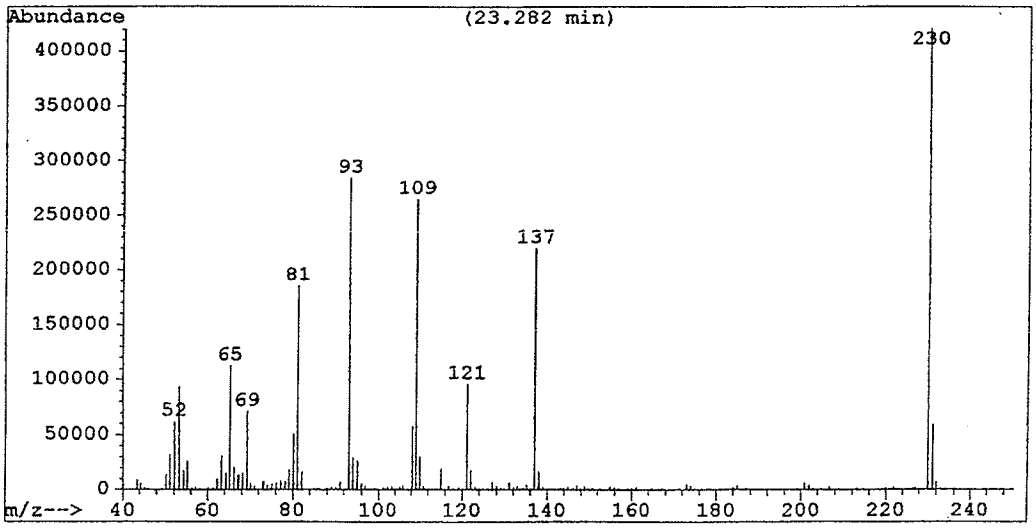

Figure 3.3.36: Mass spectrum of 23.28 minute chromatogram peak of **9g** thermolysis

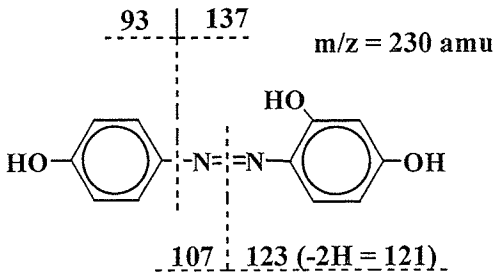

Figure 3.3.37: Fragmentation of dye **9g**

Table 3.3.32: m/z values and relative abundances of the 23.28 minute peak of **9g**

m/z	Rel. Abundance	m/z	Rel. Abundance
51.15	8	93.05	67
52.15	15	95.05	6
53.15	22	108.15	14
55.15	6	109.05	63
63.20	7	110.00	7
65.15	27	121.05	23
69.15	17	137.00	52
80.05	12	230.00	100
81.05	44	231.00	14

The two peaks following the undegraded **9g** have similar mass spectra, but differ markedly in the peak of highest mass. The middle chromatogram peak (23.47 min) shows a 302 amu peak, while the third peak in the chromatogram (23.67 min) displays a 374 amu peak. Assuming that the peak of highest mass is the molecular ion, and given that fragments of **9g** occur in both of these mass spectra, it is conceivable that a high temperature reaction occurred which produced a higher molecular weight compound similar in structure to **9g**. However, since both spectra do not show a peak of approximately 460 amu (which would correspond to two **9g** molecules linked together), or multiples thereof, the identity of the higher molecular weight compounds are unclear, although it is possible that they may be derivatized phenolic compounds. The one similarity between the spectra is that the base peaks in both mass spectra (displayed in

Figure 3.3.38 and 3.3.39) occur at 73 amu. The difference between the mass of **9g** (230 amu) and the 302 amu peak is 72 amu. Coincidentally, the difference between 230 amu and 374 amu is 144 (which can result from two 72 units put together). Therefore, given that there are peaks attributable to **9g**, and peaks of multiples of 72 in both spectra, it is plausible that approximately 72 mass units have been added to **9g**. Unfortunately, the isotopic abundances did not shed any light on the identity of the compounds, as the percentages of the isotope peaks did not correlate to any logical molecular formula. Tables 3.3.33 and 3.3.34 present the data for the two mass spectra.

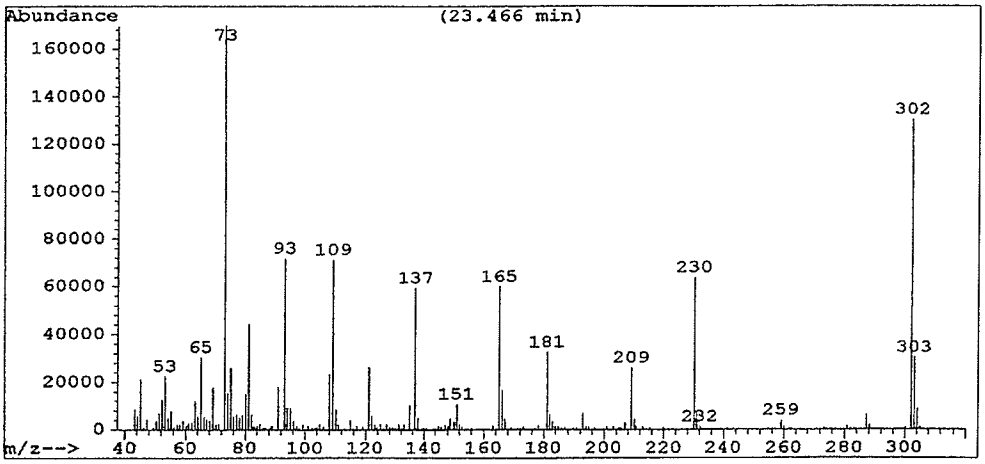

Figure 3.3.38: Mass spectra of the 23.47 minute chromatogram peak of **9g** thermolysis

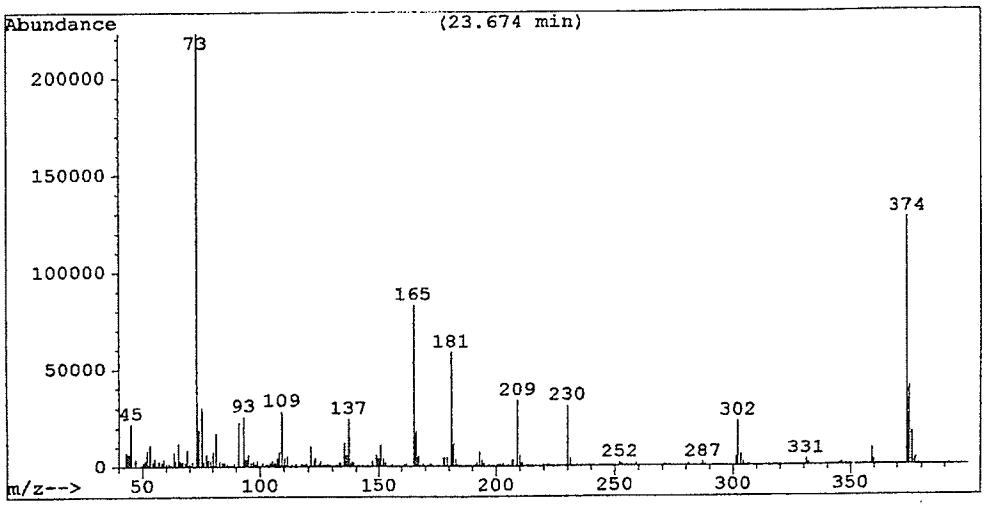

Figure 3.3.39: Mass spectra of the 23.67 minute chromatogram peak of **9g** thermolysis

Table 3.3.33: m/z values and relative abundances for 23.47 minute peak of **9g** thermolysis

m/z	Rel. Abundance	m/z	Rel. Abundance
43.25	5	95.05	5
45.20	13	107.95	14
52.25	8	109.05	42
53.15	13	110.00	5
55.15	5	120.95	15
63.20	7	134.95	6
65.15	18	137.00	35
69.15	10	151.00	6
73.10	100	165.00	35
74.10	9	166.00	10
75.10	15	180.95	19
80.05	9	208.95	15
81.05	26	230.00	38
91.05	11	231.00	5
93.05	42	302.05	77
94.05	6	303.05	18

Table 3.3.34: m/z values and relative abundances for 23.67 minute peak of **9g** thermolysis

m/z	Rel. Abundance	m/z	Rel. Abundance
45.20	10	150.90	5
53.15	5	165.00	37
73.10	100	166.00	8
75.10	14	180.95	26
81.15	8	181.85	5
91.05	10	208.95	15
93.05	12	230.05	14
109.05	13	302.05	10
120.95	5	374.20	57
134.95	5	375.20	18
136.90	11	376.20	8

4.0 Future goals of the project

The future research regarding organoiron complexed azo dyes encompasses many areas. Of particular note is the potential to synthezise tailor made coloured thermoplastic materials. The organoiron methodology, employed in the synthesis of the complexed dyes, has already proven to be successful in the synthesis of many different types of engineering thermoplastics. With the ability to bond azo chromophores as pendant side chains, or even in an organometallic backbone, there exists the possibility of creating highly coloured engineering thermoplastics, a goal which was not readily achievable before. This work is in addition to the vast area of non-linear optical applications that would also make use of organometallic azo polymers. Both applications benefit greatly from the versatility of the metal-mediated nucleophilic aromatic substitution methodology, which allows compounds to be tailored for a specific application.

With regards to the oxidative remediation of contaminants, the potential of organoiron complexes to catalyze oxidation techniques utilizing hydrogen peroxide (via a photo-Fenton reaction), creates the possibility of producing polymers that could enhance degradation processes. An organometallic thermoplastic polymer (for example, a complexed polyether), placed in an irradiated aqueous system containing contaminant and hydrogen peroxide, would photolytically decomplex releasing ferrous ions into solution which would potentially catalyze the oxidative removal of the contaminant. The polymer itself would show little to no change due to the stability of the polymer backbone.

5.0 Conclusion

A series of azo dyes containing cyclopentadienyliron moieties have been synthesized and characterized. The inclusion of complexed arenes into an azo dye structure altered the visible absorption properties of the dyes. If the complexed arene was associated with the coupling component of the azo dye, a hypsochromic shift was observed, conversely, association with the azo component resulted in a bathochromic shift. A number of complexed dyes were polymerized via reaction with dinucleophiles, thus producing coloured polymers that incorporated cyclopentadienyliron moieties. The UV-Vis properties of the polymers were not observed to change significantly when compared to the monomers.

Photolytic decomplexation using 300 nm light, which has been shown as a versatile technique for demetallation, liberated the organic azo dyes and polymers. The decomplexed coloured polymers showed little change in their absorption bands when compared with the complexed polymers, however, the lower molecular weight decomplexed dyes displayed shifts in their absorption bands which brought their λ_{max} values closer to that of their original parent dyes. This was attributed to the loss of the electron-withdrawing $CpFe^+$ moiety.

The azo dyes have been shown to degrade in irradiated solutions of H_2O_2 and with the addition of heat. Solutions irradiated with 300 nm light in the presence of H_2O_2 rapidly bleached the azo dyes studied. The rate of degradation has been shown to be pH dependent for certain dyes, with increases in rate observed in basic solution. Thermolysis trials have shown products that indicate breakage of the azo bond.

6.0 References

1. Abd-El-Aziz, A. S., Todd, E. K. *Polymer News* 2001, 26, 5-13.

2. Brown, R., Fernando, S., Roberts, M. *J. Chem. Soc. Perkin Trans.* 1994, 1, 197-201.

3. Abd-El-Aziz, A. S., Schriemer, D., C. de Denus, C., R. *Organometallics* 1994, 13, 374-384.

4. Abd-El-Aziz, A. S., de Denus, C., R. Zaworotko, M., MacGillivray, L. *J. Chem. Soc. Dalton Trans.* 1995, 3375-3393.

5. Nesmeyanov, A., Vol'Kenau, N., Bolesova, I. *Tetrahedron Letters* 1963, 25, 1725-1729.

6. Sutherland, R. *Journal of Organometallic Chemistry Library* 1977, 3, 311-342.

7. Abd-El-Aziz, A. S., Bernardin, S. *Coordination Chemistry Reviews* 2000, 203, 219-267.

8. Piorko, A., Abd-El-Aziz, A. S., Lee, C. C., Sutherland, R. *J. Chem. Soc. Perkin Trans I.* 1989, 469-475.

9. Abd-El-Aziz, A. S., Epp, K., Lei, Y., Kotowich, S. *J. Chem. Research (S)* 1995, 182-183.

10. Abd-El-Aziz, A. S., Armstrong, D., Bernardin S., Hutton, M. *Can. J. Chem.* 1996, 74, 2073-2082.

11. Abd-El-Aziz, A. S., de Denus, C., Epp, K. *Proc. Indian Acad. Sci. (Chem. Sci.),* 1995, 107, 877-888.

12. Cotter, R. *Engineering Plastics: A Handbook of Polyarylethers* Gordon and Breach Publishers: Basel, 1995.

13. Moroz, A., Shvartsberg, M. *Russ. Chem. Rev.* 1974, 43, 679.

14. Abd-El-Aziz, A. S., Todd, E., K., Ma, G. *J. Polym. Sci. Part A: Polym. Chem.* 2001, 39, 1216-1231.

15. Abd-El-Aziz, A. S., de Denus, C., Todd, E., K., Bernardin, S. *Macromolecules* 2000, 33, 5000-5005.

16. Abd-El-Aziz, A. S., May, L, J., Edel, A, L. *Polym. Prep. Am. Chem. Soc. Div. Polym. Chem.* 1999, 40, 924-925.

17. Abd-El-Aziz, A. S., Todd, E., K., Epp, K., M. *Journal of Inorganic and Organometallic Polymers* 1998, 8, 127-133.

18. Abd-El-Aziz, A. S., May, L., J., Hurd, J., A., Okasha, R., M. *Journal of Polymer Science: Part A: Polymer Chemistry* 2001, 39, 2716-2722.

19. Abd-El-Aziz, A. S., Todd, E. K., Ma, G., DiMartino, J. *Journal of Inorganic and Organometallic Polymers* 2000, 10, 265-272.

20. Segal, J. *J. Chem. Soc., Chem. Commun.* 1985, 19, 1338-1339.

21. Lee, C., Abd-El-Aziz, A. S., Chowdhury, R., Piorko, A., Sutherland, R. *Synth. React. Inorg. Met.-org. Chem.* 1986, 16, 541-552.

22. Sutherland, R., Abd-El-Aziz, A. S., Piorko, A., Baranski, A., Lee, C. *Synthetic Communications* 1989, 19, 189-195.

23. Abd-El-Aziz, A. S., Piorko, A., Baranski, A., Sutherland, R. *Synthetic Communications* 1989, 19, 1865-1870.

24. Chrisope, D., Park, K., Schuster, G. *J. Am. Chem. Soc.* 1989, 111, 6195-6201.

25. Sutherland, R., Chen, S., Pannekoek, J., Lee, C. *Journal of Organometallic Chemistry* 1975, 101, 221-229.

26. Traverso, O., Scandola, F. *Inorg. Chim. Acta.* 1970, 4, 493-498.

27. Gill, T., Mann, K. *Inorg. Chem.* 1980, 19, 3007-3010.

28. Gill, T., Mann, K. *Inorg. Chem.* 1983, 22, 1986-1991.

29. McNair, A., Schrenk, J., Mann, K. *Inorg. Chem.* 1984, 23, 2633-2640.

30. Schrenk, J., Palazzotto, M., Mann, K. *Inorg. Chem.* 1983, 22, 4047-4049.

31. Gill, T., Mann, K. *Journal of Organometallic Chemistry* 1981, 216, 65-71.

32. Park, K., Schuster, G. *Journal of Organometallic Chemistry* 1991, 402, 355-362.

33. Griffiths, J. *J.S.D.C.* **1988**, 104, 416-423.

34. Hallas, G., Towns, A. *Dyes and Pigments* **1996**, 32, 135-149.

35. Zollinger, H. *Azo and Diazo Chemistry: Aliphatic and Aromatic Compounds* Interscience Publishers: London, **1961**.

36. Mehta, H., Peters, A. *Dyes and Pigments* **1981**, 2, 259-269.

37. Peters, A. *Journal of the Society of Dyers and Colourists* **1985**, 101, 361-367.

38. Sabnis, R., Rangnekar, D. *J. Chem. Tech. Biotechnol.* **1990**, 47, 39-46.

39. Sabnis, R., Rangnekar, D. *Indian Journal of Fibre and Textile Research* **1992,** 17, 58-61.

40. Hallas, G., Towns, A. *Dyes and Pigments* **1997**, 4, 319-336.

41. Hallas, G. Towns, A. *Dyes and Pigments* **1997,** 35, 219-237.

42. Freeman, H., McIntosh, S. *Textile Research Journal* **1989**, 59, 343-349.

43. Al-Kassim, S., Peters, A. *J.S.D.C.* **1973**, 89, 359-363.

44. Kumar, G. *Azo Functional Polymers: Functional Group Approach in Macromolecular Design* Technomic Publishing: Lancaster, **1992**.

45. Bridgeman, I., Peters, A. *J.S.D.C.* **1970**, 86, 519-524.

46. Gewald, K. *Chemistry of heterocyclic compounds* **1976**, 12, 1077-1090.

47. Shvedov, V., Grinev, A. *Journal of Organic Chemistry of the USSR* **1965**, 1, 2269-2271.

48. Jackson, F., Peters, A. *J. Chem. Soc. (C)* **1969**, 268-272.

49. March, J., Smith, M. *March's Advanced Organic Chemistry*, 5th Ed. Wiley-Interscience: Toronto, **2001**.

50. Hallas, G., Towns, A. *Dyes and Pigments* **1996**, 31, 273-289.

51. Savarino, P., Viscardi, G., Barri, E., Carpignano, R., Fedorov, L. *Dyes and Pigments* **1990**, 13, 71-80.

52. Lycka, A., Jirman, J. *Two-Dimensional NMR Spectroscopy in the Analysis of Organic Dyes*, in *Colour Chemistry: The Design and Synthesis of Organic Dyes and Pigments*. Peters, A., Freeman, H. Eds. Elsevier: London, **1991**.

53. Fedorov, L. Dvoskin, S., Sokolovskii, S. *Bulletin of the Academy of Sciences of the USSR, Division of Chemical Science* **1988**, 38, 2490-2496.

54. Silberberg, M. *Chemistry: The Molecular Nature of Matter and Change* Mosby: Boston, **1996**.

55. Coyle, J. *Introduction to Organic Photochemistry* John Wiley and Sons: Toronto, **1986**.

56. Rau, H. *Angewandte Chemie-International Edition* **1973**, 12, 224-235.

57. Griffiths, J. *Developments in the Chemistry and Technology of Organic dyes.* Griffiths Ed. Blackwell Scientific Publications: Oxford, **1984**.

58. Mehta, H., Peters, A. *Dyes and Pigments* **1982**, 3, 71-78.

59. Peters, A. *J.S.D.C.* **1988**, 104, 344-348.

60. Hallas, G., Towns, A. *Dyes and Pigments* **1997**, 33, 205-213.

61. Hallas, G., Choi, J-H. *Dyes and Pigments* **1999**, 42, 249-265.

62. Peters, A., Gbadamosi, A. *J. Chem. Tech. Biotechnol.* **1992**, 53, 301-308.

63. Hallas, G. *J.S.D.C.* **1979**, 95, 285-294.

64. Cattaneo, P., Persico, M. *Phys. Chem. Chem. Phys.* **1999**, 1, 4739-4743.

65. Peters, A. *Textile Research Journal* **1974**, 44, 719-723.

66. Ruslin, C., Ichimura, K. *Journal of Materials Chemistry* **2000**, 10, 2704-2707.

67. Gordon, P., Gregory, P. *Non-Textile Uses of Dyes* in *Developments in the Chemistry and Technology of Organic Dyes* Griffiths, J., Ed. Blackwell Scientific Publications: Oxford, **1984**.

68. Hallas, G., Towns, A. *Dyes and Pigments* **1997**, 34, 133-146.

69. Freeman, H., McIntosh, S. *Textile Research Journal* **1989**, 59, 389-395.

70. Sabnis, R., Rangnekar, D. *Indian Journal of Technology* **1990**, 28, 54-58.

71. Hallas, G., Towns, A. *Dyes and Pigments* **1997**, 33, 215-228.

72. Dickey, J., Towne, E., Bloom, M., Moore, W., Smith Jr., R., Hedberg, D. *Journal of the Society of Dyers and Colourists* **1958**, 74, 123-132.

73. Hallas, G., Towns, A. *Dyes and Pigments* **1997**, 35, 45-55.

74. Sabnis, R., Rangnekar, D. *Dyes and Pigments* **1989**, 10, 285-302.

75. Matsuoka, M. *Molecular Orbital Design, Synthesis and Characteristics of Functional Dyes for Electrooptical Applications*, in *Colour Chemistry: The Design and Synthesis of Organic Dyes and Pigments* Elsevier: London, **1991**.

76. Prasad, P., Williams, D. *Introduction to Nonlinear Optical Effects in Molecules and Polymers* Wiley Interscience: Toronto, **1991**.

77. Shelton, D., Rice, J. *Chem. Rev.* **1994**, 94, 3-29.

78. Burland, D., Miller, R., Walsh, C. *Chem. Rev.* **1994**, 94, 31-75.

79. Morely, J., Hutchings, M., Zyss, J., Ledoux, I. *J. Chem. Soc. Perkin Trans.* **1997**, 2, 1139-1141.

80. Dirk, C., Katz, H., Schilling, M. *Chem. Mater.* **1990**, 2, 700-705.

81. Barlow, S., Bunting, H., Ringham, C., Green, J., Bublitz, G., Boxer, S., Perry, J., Marder, S. *J. Am. Chem. Soc.* **1999**, 121, 3715-3723.

82. Morley, J. *J. Chem. Soc. Perkin Trans.* **1995**, 2, 177-180.

83. Hutchings, M., Ferguson, I., McGreein, D., Morley, J., Zyss, J., Ledoux, I. *J. Chem. Soc. Perkin Trans.* **1995**, 2, 171-176.

84. Moerner, W., Silence, S. *Chem. Rev.* **1994**, 94, 127-155.

85. Seki, T. Ichimura, K. *Polymer Communications* **1989**, 30, 108-110.

86. Kumar, G., Neckers, D. *Chem. Rev.* **1989**, 89, 1915-1925.

87. Wu, L., Tuo, X., Cheng, H., Chen, Z., Wang, X. *Macromolecules* **2001**, 34, 8005-8013.

88. Lee, S-H., Balasubramanian, S., Kim, D. Viswarathan, N. Bian, S., Kumar, J., Tripathy, S. *Macromolecules* **2000**, 33, 6534-6540.

89. Junge, D., McGrath, D. *Chem. Commum.* **1997**, 9, 857-858.

90. Iftime, G., Labarthet, F., Natansohn, A., Rochon, P., Murti, K. *Chem. Mater.* **2002**, 14, 168-174.

91. Zagorska, M., Rulszewicz-Bajer, I., Pron, A., Sukiennik, J., Raimond, P. *Macromolecules* **1998**, 31, 9146-9153.

92. Bergbreiter, D., Osburn, P., Li, C. *Organic Letters* **2002**, 4, 737-740.

93. Liu, X., Bruce, D., Manners, I. *Chem. Commun.* **1997**, 289-290.

94. Wang, Z., Chen, K., Tian, H. *Chemistry Letters*. **1999**, 423-424.

95. Wang, Z., Tian, H., Chen, K. *Dyes and Pigments* **2001**, 51, 161-165.

96. Kurosawa, M., Nankawa, T., Matsuda, T., Kubo, K., Kurihara, M., Nishihara, H. *Inorg. Chem.* **1999**, 38, 5113-5123.

97. Yam, V., Yang, Y., Zhang, J., Chu, B., Zhu, N. *Organometallics* **2001**, 20, 4911-4918.

98. Dulta, S., Peng, S., Bhattacharya, S. *J. Chem. Soc. Dalton Trans.* **2000**, 24, 4623-4627.

99. Freeman, H., Hsu, W. *Textile Research Journal* **1987**, 57, 223-234.

100. Bridgeman, I., Peters, A. *Textile Research Journal* **1974**, 44, 645-649.

101. Albini, A., Fasani, E., Pietra, S. *J. Chem. Soc. Perkin Trans.* II **1982**, 1393-1395.

102. Neevel, J., Beek, H., Ouden, H., van de Graaf, B. *JSDC* **1990**, 106, 176-181.

103. Majcen-Le Marechal, A., Slokar, Y., Taufer, T. *Dyes and Pigments* **1997**, 33, 281-298.

104. Hallas, G. *Recent Developments in dyes for textile applications* in *Developments in the Chemistry and Technology of Organic Dyes* Griffiths, J. Ed. Blackwell Scientific Publications: Oxford, **1984**, 31-65.

105. Holme, I. *Ecological aspects of colour chemistry* in *Developments in the Chemistry and Technology of Organic Dyes* Griffiths, J. Ed. Blackwell Scientific Publications: Oxford, **1984**, 111-126.

106. Raffainer, I., Rudolf von Rohr, P. *Ind. Eng. Chem. Res.* **2001**, 40, 1083-1089.

107. Galindo, C., Kalt, A. *Dyes and Pigments* **1999**, 42, 199-207.

108. Donlagic, J., Levec, J. *Environ. Sci. Technol.* **1998**, 32, 1294-1302.

109. Grau, P. *Wat. Sci. Tech.* **1991**, 24, 97-103.

110. Georgiou, D., Melidis, P., Aivasidis, A., Gimouhopoulos, K. *Dyes and Pigments* **2002**, 52, 69-78.

111. Colonna, G., Caronna, T., Marcandalli, B. *Dyes and Pigments* **1999**, 41, 211-220.

112.Chu, W. *Wat. Res.* **2001**, 35, 3147-3152.

113. Fernandez, J., Bandara, J., Lopez, A., Buffat, Ph., Kiwi, J. *Langmuir* **1999**, 15, 185-192.

114. Joseph, J., Destaillats, H., Hung, H., Hoffmann, M. *J. Phys. Chem. A* **2000**, 104, 301-307.

115. Bandara, J., Mielczarski, J., Kiwi, J. *Langmuir* **1999**, 15, 7680-7687.

116. Zhan, H., Tian, H. *Dyes and Pigments* **1998**, 37, 231-239.

117. Viodgopal, K., Wynkoop, D. *Environ. Sci. Technol.* **1996**, 30, 1660-1666.

118. Kadota, K., Dan-oh, Y., Uneyama, K. *J. Org. Chem.* **1996**, 61, 2364-2367.

119. Skoog, D., Holler, J., Nieman, T. *Principles of Instrumental Analysis* 5th ed. Saunders College Publishing: Montreal, **1998**.

120. Harris, D. *Quantitative Chemical Analysis* 4th ed. W.H. Freeman and Company: New York, **1995**.

121. Silverstein, R., Webster, F. *Spectrometric Identification of Organic Compounds* 6th ed. John Wiley & Sons: Toronto, **1998**.

122. Schwedt, G. *The Essential Guide to Analytical Chemistry* John Wiley & Sons: Toronto, **1997**.

123. Calabrese, G., Christian-Maillet, L. *Anal. Chem.* **1992**, 64, 120-123.

124. Szafran, Z., Pike, R., Singh, M. *Microscale Inorganic Chemistry* John Wiley & Sons: Toronto, **1991**.

125. Odian, G. *Principles of Polymerization*, 3rd ed. John Wiley & Sons: Toronto, **1991**.

126. Parker, C. *Proc. Roy. Soc. (London) A* **1953**, 220, 104-116.

127. Murov, S. *Handbook of Photochemistry* Marcel Dekker: New York, **1973**.

128. Hatchard, C., Parker, C. *Proc. Roy. Soc. (London) A* **1956**, 235, 518-536.

129. Porter, G., Doering, J., Karanka, S. *Talanta* **1960**, 44, 4027-4029.

130. Nussbaum, M., Nekimken, H., Nieman, T. *Anal. Chem.* **1987**, 59, 211-212.

131. Zepp, P. *Environ. Sci. Technol.* 12, **1977**, 327-329.

132. Khand, I., Pauson, P., Watts, W. *J. Chem. Soc. C.* **1968**, 2257-2260.

133. Khand, I., Pauson, P., Watts, W. *J. Chem. Soc. C.* **1968**, 2261-2265.

134. Morrison, W., Ho, E., Hendrickson, D. *Inorg. Chem.* **1975**, 14, 500-506.

135. Szantay, C., Csepregi, Z., Aranyosi, P., Rusznak, I., Toke, L., Vig, A. *Magnetic Resonance in Chemistry* **1997**, 35, 306-310.

136. Peng, Q., Li, M., Gao, K., Cheng, L. *Dyes and Pigments* **1990**, 14, 89-99.

137. Lycka, A. *Dyes and Pigments* **1999**, 43, 27-32.